Investigating Planetary Core Formation with Geophysical Modeling and High-Pressure Mineralogy

HARVARD UNIVERSITY
Graduate School of Arts and Sciences

DISSERTATION ACCEPTANCE CERTIFICATE

The undersigned, appointed by the

Department of Earth and Planetary Sciences

have examined a dissertation entitled

"Investigating Planetary Core Formation with Geophysical Modeling and High-Pressure Mineralogy"

presented by Matthew C. Brennan

candidate for the degree of Doctor of Philosophy and hereby certify that it is worthy of acceptance.

Signature Rebecca Fischer Digitally signed by Rebecca Fischer Date: 2022.04.13 17:04:03 -04'00'

Typed name: Prof. Rebecca Fischer

Signature Stein B Jacobsen Digitally signed by Stein B Jacobsen Date: 2022.04.28 11:30:36 -04'00'

Typed name: Prof. Stein Jacobsen

Signature Digitally signed by Lowell Miyagi Date: 2022.04.13 12:16:21 -06'00'

Typed name: Prof. Lowell Miyagi

Signature Jerry Mitrovica Digitally signed by Jerry Mitrovica Date: 2022.04.13 13:36:18 -04'00'

Typed name: Prof. Jerry Mitrovica

Date: April 12, 2022

Investigating Planetary Core Formation with Geophysical Modeling and High-Pressure Mineralogy

a dissertation presented by

Matthew C. Brennan

to the

Department of Earth and Planetary Sciences

in partial fulfillment of the requirements

for the degree of

Doctor of Philosophy

Harvard University

Cambridge, Massachusetts

April 2022

Dissertation Advisor: Rebecca A. Fischer Matthew C. Brennan

Investigating Planetary Core Formation with Geophysical Modeling and High-Pressure Mineralogy

Abstract

Earth's core is impossible to sample or directly observe and yet is fundamentally important to the properties of, and our continued existence on, this planet. Indeed, planetary cores literally underlie every other area of geoscientific inquiry, and core properties controlled the development of Earth, Mars, and likely every other terrestrial planet. As this importance has become evident over the last century, several methods of indirectly investigating planetary cores have been developed. These include the use of mineral physics experiments to measure materials at ultra-high pressures and temperatures, seismic observations to constrain bulk physical properties, and numerical simulations to turn such data into comprehensive models of planetary interiors. In this dissertation, I present results from several studies that combine these methods in various ways to advance our understanding of the formation and evolution of the cores of Earth and Mars.

Chapter 1 (**General Introduction**) gives a brief synopsis of the study of the deep Earth (and Mars). This includes the history of the field, the major research methodologies that appear in subsequent chapters, and the current scientific consensus concerning planetary cores.

Chapter 2 (**Martian Core Formation and the Geophysical Properties of Deep Mars**) presents a simulation of Mars' growth and core-mantle differentiation, parameterized by metal-silicate partitioning experiments and geophysical data

measured by spacecraft. The model was able to reproduce the canonical Martian mantle composition in scenarios where Mars was built from oxidized primordial material that was highly equilibrated in a magma ocean of intermediate depth, resulting in a sulfur-rich core. This model allowed us to evaluate various physical properties of the deep Martian interior and generate predictions of observable seismic properties. We determined that to maintain consistency with measured physical parameters, the core must constitute about half of Mars' radius, a size later confirmed by the groundbreaking seismic measurements of the InSight mission.

Chapter 3 (**Timing of Martian Accretion and Core Formation**) extends the model described in Chapter 2 by incorporating realistic Martian accretion histories from dynamical simulations of solar system formation and constraints from the hafnium–tungsten (Hf–W) radioisotopic system. The evolution of Mars' Hf–W signature is sensitive to a variety of accretionary conditions, especially the oxidation of primordial material. With the right conditions, it is possible to match the Martian signature for a variety of accretion histories, including ones which continue for many times longer than the previously supposed maximum growth period. Additionally, there does not appear to be a relationship between the final orbits of Mars-like bodies and the material that formed them. This implies that Mars might have accreted from a single geochemical reservoir somewhere in the protoplanetary disk before being gravitationally scattered to its modern location.

Chapter 4 (**Deformation Properties of Earth's Inner Core**) presents the results of diamond anvil cell radial X-ray diffraction experiments that investigated the yield strength and deformation texture of alloys similar in composition to Earth's core. These are the first such experiments on alloys containing a light element, which we

found increased alloy strength by up to an order of magnitude. The texture produced upon plastic deformation was consistent with that found by previous studies and believed to exist in Earth's inner core. However, the enhanced mechanical strength of the alloy may imply that this texture developed by a mechanism other than deformation.

Acknowledgements

In addition to the coauthors, collaborators, and funding sources listed at the end of the relevant chapters, I would like to thank Professors Lowell M. Miyagi, Stein B. Jacobsen, and Jerry X. Mitrovica for sitting on my dissertation committee and approving this document. I must also thank my advisor Professor Rebecca A. Fischer for half a decade of support and tutelage, and *her* advisor, Professor Andrew J. Campbell, for getting me started in mineral physics. Like all dissertations, this one was only possible because of contributions from far too many individuals and entities to individually recognize. For some of these, please refer to this incomplete list: Aimee, Alec, Aleyda, Allison, Anne, Annika, Anthony, Bethany, Brian, Camille, Caroline, Christopher, Christopher, Claire, Clint, Darius, David, Deborah, Dennis, Dion, Edward, Esther, Francis, Francisca, Franklin, Gavin, Jesse, John, John, John, Jon, Joseph, Joshua, Junjie, Kaitlyn, Katherine, Kimberly, Linda, Maria, Marisa, Martin, Mary, Maryorie, Michael, Michael, Morgan, Mu, Natasha, Nigel, Paul, Raquel, Robert, Rohan, Samantha, Samuel, Sarah, Sophie, Stephan, Ty, William, William, Yaray, and Zachary.

“Since then the mean denſity of the whole earth is about double that of the general matter near the ſurface, within our reach, it follows that there muſt be ſomewhere within the earth, towards the more central parts, great quantities of metals…”

—first description of the core (Charles Hutton, 1778)

Contents

List of Figures

List of Tables

Chapter 1
General Introduction

Matthew C. Brennan[1]

[1]Harvard University, Department of Earth and Planetary Sciences

1.1 History of the Study of Planetary Cores

The concept of experimentally investigating the deep Earth was first explored by Isaac Newton, who speculated that Earth's density was 5–6 times greater than that of water and proposed experiments to measure this value via the gravitational attraction induced on a pendulum by a nearby mountain (Newton, 1687). A century later, this experiment was attempted on Schiehallion, a Scottish mountain selected by surveyor Charles Mason (of Mason–Dixon fame). Astronomer Royal Nevil Maskelyne successfully measured Schiehallion's gravitational attraction and determined that the bulk Earth was about twice as dense as the mountain's rock (Maskelyne, 1775). More complete surveys of the mountain allowed Charles Hutton to refine Earth's estimated density to 4.5 times that of water and conclude that the other terrestrial planets were similarly dense (Hutton, 1778). Later, John Mitchell devised an apparatus to measure the gravitational attraction of leaden balls; this device was used by Henry Cavendish to calculate an Earth density 5.48 times that of water (Cavendish, 1798), close to the modern accepted value (5.514 times that of water, i.e., 5.514 g/cm^3). These early experiments conclusively demonstrated that Earth's interior contains great quantities of a material much denser than surface rocks (which generally have densities less than 3 g/cm^3). Then, as now, the only reasonable candidates for such a material were varieties of metal.

Separating the properties of this metal from those of the overlying rocks required the advent of seismology in the 1800s. By the end of the century, it had become possible to detect vibrations from earthquakes that had travelled great distances through the Earth's interior, a development enabled in part by the damped-pendulum seismometer of Emil Wiechert (Dewey & Byerly, 1969). Wiechert's other

major contribution (besides the discovery of the electron) was his use of these vibrations to interpret the mass distribution within the Earth, with the conclusion that there was indeed a metallic core accounting for 78% of Earth's radius (Wiechert, 1897). The exact size was contested; Richard Oldham took the contrary position that the core was only 39% of the radius, but Wiechert's student Beno Gutenberg eventually determined the correct size (3485 km, or 55% of Earth's radius) based on reflections of compressional (P) waves (Gutenberg, 1914). Gutenberg also discovered that the core blocked the propagation of shear (S) waves, a phenomenon characteristic of liquids. Combined with calculations of Earth's tidal deformation (Jefferys, 1926), this "shadow zone" revealed that the core was molten. A solid inner core (with a radius of 1220 km) would eventually be proposed by Inge Lehmann based on the shadow zone's excess P wave energy (Lehmann, 1936).

This burgeoning era of seismology coincided with the development of laboratory techniques suitable to investigating geological materials under deep Earth conditions. Unquestionably, the leading figure in this high-pressure revolution was Percy Bridgman. Over his 54 years at Harvard, Bridgman made contributions to mathematics, thermodynamics, and the philosophy of science, but his signature work was on the physics of materials at high pressure, for which he was awarded the Nobel Prize in 1946 (Kemble & Birch, 1970). The "Bridgman press" was the first device to compress a sample to 1 gigapascal (~10,000 atmospheres) and the first used to investigate polymorphism of geological materials. Having previously discovered that numerous high-density crystal structures are produced upon compression of water ice (e.g., Bridgman, 1912), Bridgman surmised that the same process might occur in rock-forming minerals and be responsible for various seismic features of the deep Earth (e.g., Bridgman, 1939). To investigate this concept further, Bridgman, along with

geologist Reginald Daly, astronomer Harlow Shapely, and others, established the Harvard Committee on Experimental Geology and Geophysics in 1932, the world's first such initiative.

The Committee's first hire immediately resigned and was replaced by one of Bridgman's doctoral students, Francis Birch, who would go on to combine his mentor's experimental methods with seismic data and crystallographic theory, establishing the field of mineral physics as we know it today. He spent a few years studying the elastic properties of rocks at high pressures (e.g., Birch & Bancroft, 1938) before the advent of World War II induced Bridgman to dispatch him to the MIT Radiation Lab. From there, Birch became one of the senior figures of the Manhattan Project, and was responsible for the preparation, loading, and arming of the Little Boy weapon on Tinian Island. Birch's most consequential scientific contributions came upon his return to Harvard, first with his extension of Francis Murnaghan's finite-strain equation of state to higher-pressure cases where the derivative of the bulk modulus itself varies with pressure (Birch, 1947). This "Birch–Murnaghan equation of state" allows conversion between the pressure and volume of a crystal across the range of deep Earth conditions and is still the most widely-used formulation in high-pressure science.

Birch's great work, however, was "Elasticity and constitution of the Earth's interior" (Birch, 1952). In the decades since first measuring the size and state of the core, Gutenberg, Jefferies, and other seismologists had discovered several other seismic discontinuities at shallower depths. Birch explicitly identified these transitions with predicted high-pressure polymorphic transformations of ultramafic minerals, establishing the familiar "upper-transition-lower" model of the mantle. All these predicted polymorphs were later experimentally confirmed and/or discovered in

nature, with the most important of all, the perovskite-structured ferromagnesian silicate (now named “bridgmanite”), finally being discovered in nature within the last decade (Tschauner et al., 2014). Birch also demonstrated that the metal that forms the core must be an alloy of iron (Fe) and nickel (Ni). This was already the most popular hypothesis due to the presence of metallic Fe–Ni in meteorites and other factors (e.g., Washington, 1925), but Birch showed conclusively that no other substance was consistent with the core’s density and seismic velocity, or with Earth’s bulk composition. In making these calculations, however, Birch noticed a slight deficit in the density of the core compared to Fe–Ni at the relevant pressures (~10% lower in the outer core, ~4% in the inner core), indicating that the Fe–Ni is alloyed with some lighter substance. Birch famously mused that the core was “an uncertain mixture of all the elements”, and identifying that mixture remains a central aim of mineral physics 70 years later.

1.2 Important Apparatus, Simulations, and Sources of Data

In the decades since establishing the fundamental facts of the deep Earth, mineral physics and allied fields have refined our knowledge by incorporating a very wide variety of experimental, observational, and computational data. While more comprehensive overviews of these are available, this section provides brief descriptions of important techniques used or alluded to in the subsequent chapters.

1.2.1 Diamond Anvil Cell

The diamond anvil cell (DAC) is the most modern evolution of the Bridgman press. Retaining the simplicity of the original concept, the DAC is comprised of two identical flawless diamonds facing each other in a small metal container. The

diamonds are cut similarly to the “round brilliant” shape common in jewelry but retain the flat “culet” facet at their apex (not included in most modern gemstones) instead of tapering to a point. The diamond anvils are aligned such that their culets press against each other when the DAC is closed (Figure 1.1). Since pressure is equal to force divided by area and the diamond culets are very small (usually ~0.2 mm in diameter), manually applying force to the cell with screws can easily generate deep Earth pressures on this tiny contact point. Diamonds are very hard, and therefore resistant to deformation upon compression, allowing DACs to reach pressures up to hundreds of gigapascals (millions of atmospheres) before the anvils shatter. Diamonds are also very transparent, allowing DAC samples to be observed and modified (such as by heating with a laser) while compressed.

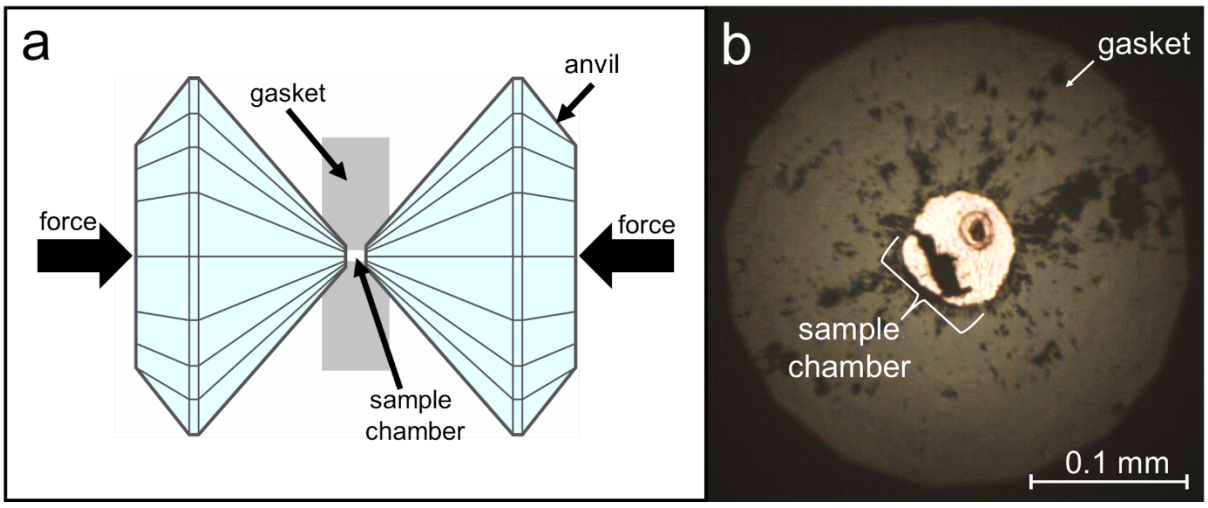

Figure 1.1 a: Schematic of a DAC. Samples are loaded between opposing diamond anvils in a “chamber” formed by a hole drilled into a (usually metal) gasket, shown here in cross section. Samples are pressurized by forcing the diamonds towards each other. **b:** Photomicrograph of an illuminated DAC sample chamber loaded with two sample materials and surrounded by the gasket. This image was taken through one of the anvils in the same direction as the applied force.

1.2.1.1 Synchrotron X-ray Diffraction

The DAC is a static compression apparatus, which means that samples can be compressed and held at high pressure indefinitely while experiments are performed in situ. Focusing an X-ray on the sample allows for measurements with X-ray diffraction (XRD), one of the most powerful tools for investigating crystal structures. XRD relies on the similarity between the wavelength of X-ray light and the interatomic distances of most solids; in crystals, atoms are arranged in orderly repeating patterns, so X-rays reflect and constructively interfere at predictable angles described by Bragg's Law (Bragg & Bragg, 1913). The ability to identify the crystal structure responsible for a certain set of reflections is extremely useful and makes XRD one of the most widely used experimental techniques across disciplines (e.g., Borisov & Podberezskaya, 2012). In mineral physics, XRD enables experimenters to, among other things, observe polymorphic phase transformations of samples and determine their specific volumes (and thus also their pressures via an equation of state).

Most XRD experiments use compact "cabinet diffractometers", in which radiation is generated by excitation of a metal, but DAC samples are very small, and thus require the extremely high fluxes of synchrotron X-ray sources to generate a detectable signal on a practical timescale. Synchrotrons are a type of particle accelerator in which electrons are magnetically induced to travel at >99.99% the speed of light before suddenly being forced to turn a corner. Just like a driver pressed up against the car door during a tight turn, the electron's momentum attempts to continue in its original direction, and this energy is released by the emission of an X-ray.

An inherent feature of the DAC is that force is applied uniaxially at a right angle to the diamond culets (Figure 1.1). This unequal compression geometry is undesirable for most applications, so the experimental sample is generally floated in an extremely soft “pressure medium”, like fluid or salt, to make the pressure approximately hydrostatic (i.e., equal in all directions). However, experiments focused on sample deformation can generate the differential stresses they require by forgoing a pressure medium. In this case, the DAC’s compressive axis must be rotated orthogonally to the path of the X-ray beam to ensure that the Bragg condition is met by the crystal lattice planes experiencing maximum deformation (Singh, 1993). In these radial X-ray diffraction experiments, the X-rays must pass through the containing gasket to reach the sample, necessitating the use of X-ray transparent materials like beryllium or boron.

1.2.1.2 Metal–Silicate Partitioning

Metal–silicate partitioning experiments involve loading a sample with an iron alloy and a silicate mineral assemblage, heating until the two come to chemical equilibrium, and then quenching and extracting the sample. The composition of each phase can then be measured with a device such as an electron microprobe, thus quantifying the chemical affinity of the elements present in the original sample. Though the affinities of most elements have been understood since the formulation of the Goldschmidt classification (Goldschmidt, 1937), these can change at the extreme conditions of planetary interiors. Performing partitioning experiments at a variety of conditions allows us to interpret how elements will behave under arbitrary physical and chemical conditions, and these data are frequently used to parameterize computational models of core formation. Since rock samples grant us some understanding of Earth’s (and to a lesser extent, Mars’) silicate mantle composition

(Section 1.2.3), identifying the partitioning conditions that produced it provides key insight into the composition of the metallic core.

1.2.2 Seismology

It is impossible to directly observe the deep Earth, but we can analyze vibrations that have passed through it. Deep Earth seismology is a field unto itself (e.g., Dziewonski & Romanowicz, 2015), but its focus can generally be divided into body waves and normal modes. Body waves are high-frequency vibrations generated by an earthquake and detected later by a seismometer some distance away. If the distance from the original earthquake is known, travel times of various vibrations can be used to determine their path through the Earth, and the properties of the layers encountered along the way. For example, body wave PKiKP is a compressional wave that travels through the mantle (P) and outer core (K), bounces off the surface of the inner core (i), and traverses the outer core (K) and mantle (P) again on its way back to the surface. All else being equal, a faster PKiKP arrival time means that the bounce happened at a shallower depth, thus indicating a larger inner core (Engdhal et al., 1974).

While body wave arrivals have been interpreted for over a century (Section 1.1), the use of normal modes only became feasible with the advent of large seismic arrays capable of detecting low-frequency vibrations (Gilbert & Dziewonski, 1975). Normal modes are best described as elastic oscillations of the whole Earth simultaneously, like the vibrations of a plucked guitar string. Since they depend on the mechanical properties of the interior, normal modes complement non-seismic geophysical data, such as planetary moment of inertia (i.e., mass distribution in the interior) and dissipation of tidal energy (i.e., rigidity of the interior).

The modern era of massive, coordinated, long-term seismic studies has greatly expanded our understanding of the Earth's deep interior. In particular, the development of the one-dimensional Preliminary Reference Earth Model (PREM) set a canonical average density and velocity structure against which all other observations could be compared (Dziewonski & Anderson, 1981). Anomalous deviations from PREM have contributed to numerous discoveries, among them features such as the regional heterogeneity of the inner core (e.g., Deuss, 2014). Unfortunately, these discoveries are Earth-specific; it is impossible to extrapolate much of our seismology-derived understanding to other terrestrial bodies. However, the limited measurements taken during the Apollo missions allowed for the detection of a lunar core (Weber et al., 2011), and the ongoing InSight mission has successfully returned the first seismic data from Mars (Banerdt et al., 2020). While a single seismometer on a tectonically inactive planet cannot hope to compete with terrestrial datasets, there is historical precedent for the value of even the most limited seismic measurements.

1.2.3 Meteorites

Earth's surface offers an unlimited supply of geochemical samples in the form of rocks, but surface rocks are products of our planet's complex geological history and therefore rarely record evidence of primordial events such as core formation. Meteorites offer an independent and often complementary dataset. There are two main meteorite types: chondrites, which are believed to represent primordial material from the very early Solar System, and achondrites, which are fragments of terrestrial bodies that have experienced core formation. Of the former group, the CI chondrites most closely match the composition of the Sun, and likely the bulk Solar System as well. This correspondence has been widely used in combination with terrestrial rocks to determine Earth's bulk mantle composition (e.g., McDonough & Sun, 1995). As noted in

Section 1.1, the abundance of meteoritic Fe–Ni alloy provided important circumstantial evidence for the composition of Earth's core; indeed, metallic achondrites are now understood to represent destroyed terrestrial cores. There are also stony achondrites derived from the mantles of terrestrial bodies, including the Moon, Mars, and asteroid 4 Vesta. While these present the same challenging geological history as terrestrial rocks, they are nonetheless invaluable to our understanding of their source bodies. For example, essentially our entire understanding of Mars' interior chemistry (i.e., the composition of its core and mantle) relies on analysis of the handful (<70 kg total) of known Martian meteorites in comparison with various chondrite groups (e.g., Dreibus & Wänke, 1985).

1.2.4 Accretionary Simulations

Over the last few decades, our increased understanding of the physical and chemical properties of terrestrial bodies has allowed us to work backwards and interpret the evolution of the Solar System. Astrophysics has shown that the Solar System originated in a gravitationally-collapsed cloud of interstellar gas and dust, the nucleus of which became sufficiently dense to fuse hydrogen and form the protosun (Cameron, 1962). The system's evolution from there to its modern configuration, however, is less clear. At some point, the primordial nebula condensed into solid grains that became gravitationally consolidated into meteoroids, asteroids, and planets, the largest of which (Jupiter and Saturn) were massive enough to trap some of the nebular gas before it dissipated. The basic Solar System architecture, in which small, terrestrial planets orbit close to the Sun and giant, volatile-rich (i.e., rich in hydrogen and oxygen) planets orbit further out is likely a consequence of nebular temperature gradients; it would have been too hot near the protosun for water ice to condense (e.g., Lodders, 2003). The starting materials of the inner Solar System must

therefore have been chondrite-like concretions of heavier elements like iron, magnesium, and silicon with a relatively modest amounts of volatiles.

The process of building the terrestrial planets from such concretions is generally studied by means of computational simulations that attempt to track material as it accumulates together ("accretes") to form larger bodies. While the early stages of this process are best treated statistically, *N*-body simulations have proved most fruitful once the protoplanetary bodies have reached the size of asteroids. In an *N*-body simulation, the location and velocity of many objects are tracked simultaneously, as well as the force (i.e., gravitational attraction) exerted on each object by every other one. By calculating the sum of forces on an object, its motion can be calculated, and its location updated to where it would be, say, an hour hence. By doing this for every object over a long series of short intervals, the dynamics of the whole system can be tracked until the final planetary configuration is produced. The dynamical behavior of an *N*-body system is a famously difficult physics problem (e.g., Newton, 1687) and requires substantial computational power to simulate. Additionally, such systems are deterministically chaotic (i.e., highly sensitive to starting conditions); in one study, it was found that changing the initial location of just one of the thousands of simulated protoplanetary bodies by just one meter completely altered the final configuration of the Solar System (Lissauer, 2007). This means that these computationally expensive simulations must be run many times to determine which narratives of Solar System evolution are truly robust, a task that has benefitted from the enormously improved capabilities of modern hardware. Recent *N*-body simulations have improved our understanding of both the dynamics of planetary formation (e.g., Kokubo & Genda, 2010; Fischer & Ciesla, 2014) and the geochemical evolution of terrestrial bodies (e.g., Rubie et al., 2015; Fischer & Nimmo, 2018).

Chapter 2
Martian Core Formation and the Geophysical Properties of Deep Mars

Matthew C. Brennan[1], Rebecca A. Fischer[1], Jessica C. E. Irving[2]

[1]Harvard University, Department of Earth and Planetary Sciences

[2]Princeton University, Department of Geosciences (now at University of Bristol, School of Earth Sciences)

The contents of this chapter are based on: "Core Formation and Geophysical Properties of Mars" (2020). *Earth and Planetary Science Letters* 530, 115923.

Abstract

The chemical and physical properties of the interiors of terrestrial planets are largely determined during their formation and differentiation. Modeling a planet's formation provides important insights into the properties of its core and mantle, and conversely, knowledge of those properties may constrain formational narratives. Here, we present a multi-stage model of Martian core formation in which we calculate core–mantle equilibration using parameterizations from high pressure–temperature metal–silicate partitioning experiments. We account for changing core–mantle boundary (CMB) conditions, composition-dependent partitioning, and partial equilibration of metal and silicate, and we evolve oxygen fugacity (fO_2) self-consistently. The model successfully reproduces published meteorite-based estimates of most elemental abundances in the bulk silicate Mars, which can be used to estimate core formation conditions and core composition. This composition implies that the primordial material that formed Mars was significantly more oxidized (0.9–1.4 log units below the iron–wüstite buffer) than that of the Earth, and that core–mantle equilibration in Mars occurred at 42–60% of the evolving CMB pressure. On average, at least 84% of accreted metal and at least 40% of the mantle were equilibrated in each impact, a significantly higher degree of metal equilibration than previously reported for the Earth. In agreement with previous studies, the modeled Martian core is rich in sulfur (18–19 wt%), with less than one weight percent O and negligible Si.

We have used these core and mantle compositions to produce physical models of the present-day Martian interior and evaluate the sensitivity of core radius to crustal thickness, mantle temperature, core composition, core temperature, and density of the core alloy. Trade-offs in how these properties affect observable physical parameters

like planetary mass, radius, moment of inertia, and tidal Love number k_2 define a range of likely core radii: 1620–1870 km. Seismic velocity profiles for several combinations of model parameters have been used to predict seismic body-wave travel times and planetary normal mode frequencies. These results may be compared to forthcoming Martian seismic data to further constrain core formation conditions and geophysical properties.

2.1 Introduction

At present, most of our knowledge of the Martian interior relies on inferences from meteorites and measurable geophysical properties, such as planetary mass, inertia, and tidal responses. While the ongoing InSight mission may directly measure the seismic properties of the interior (Panning et al., 2017), interpreting these data will require an understanding of the Martian composition.

Martian mantle composition can be determined by extrapolating the compositions of Martian meteorites, particularly the Shergotty-Nakhla-Chassigny (SNC) group, back to their source. Dreibus and Wänke (1985) developed the canonical model for the silicate Mars (updated by Taylor, 2013) by measuring SNC elemental abundances and proposing that their ratios reflect a mixture of volatile-rich and volatile-poor materials. In later studies, such as Lodders and Fegley (1997) and Sanloup et al. (1999), compositional models were constructed by matching the oxygen isotopic composition of the SNCs to mixtures of chondrites. From these studies, Mars is interpreted to have an FeO-enriched mantle and a smaller core mass fraction relative to Earth, indicating more oxidizing formational conditions (e.g., Rubie et al., 2011). The proximity of Mars to the protoplanetary snow line during its formation may have

resulted in accretion of a larger portion of relatively oxidized, volatile-rich material. Mars is also thought to have a sulfur-rich core based on mass balance arguments (e.g., Anderson, 1972) and chalcophile element depletions (e.g., Wänke, 1991; Wänke and Dreibus, 1988; Yang et al., 2015). Sulfur-rich iron alloys have low melting temperatures, so a high S content may have prevented crystallization of an inner core, consistent with the lack of a modern Martian geodynamo (Helffrich, 2017; Williams and Nimmo, 2004).

One difficulty in evaluating compositional models is determining whether they accurately reflect the behavior of materials during core formation. Single-stage differentiation models use metal–silicate partitioning data to determine one pressure–temperature–oxygen fugacity (P–T–fO_2) condition that can simultaneously reproduce the abundances of several elements (e.g., Rai and van Westrenen, 2013; Righter and Chabot, 2011; Steenstra and van Westrenen, 2018). However, these models do not account for changing conditions during planetary growth, so it is important to check such conclusions with more realistic models. Multi-stage core formation models can constrain the conditions of core formation by comparing the meteorite-based mantle elemental abundances to those calculated at different model conditions for the subset of elements sensitive to the style of core formation (e.g., depth evolution and degree of equilibration). Rubie et al. (2015) calculated Martian core formation in a multi-stage model with self-consistent fO_2 evolution, though their model did not include S and only used the Martian FeO content as a constraint.

Core formation has implications for the modern-day physical state of the Martian interior. Previous studies developed models of the Martian interior that match geophysical parameters such as bulk density and moment of inertia factor (MOI) and

geochemical properties inferred from SNC meteorites (e.g., Bertka and Fei, 1998; Khan et al., 2018; Nimmo and Faul, 2013; Plesa et al., 2018; Rivoldini et al., 2011; Sohl and Spohn, 1997). Sohl and Spohn (1997) developed one model that matched the MOI and another that matched the Fe/Si ratio of Mars. These models improved on earlier assessments by using equations of state to calculate the behavior of Martian minerals at high P–T and constrained the core size to 1400–1700 km. Bertka and Fei (1998) found a core size compatible with this range for Fe–14wt%S (~1400 km). Later measurements of the MOI of Mars, its tidal Love number (k_2), and its tidal dissipation factor (Q) seemed to only be matched by models with larger cores. For example, Rivoldini et al. (2011) found that MOI and k_2 were best matched by cores 1730–1860 km in radius. Varying parameters such as core density and mantle thermal structure can produce models that match these same constraints at a range of core sizes (Nimmo and Faul, 2013), so it is important to evaluate the influence of these parameters. Khan et al. (2018) inverted for the most likely ranges of several properties, including core composition, CMB temperature, and lithospheric thickness, and they constructed seismic velocity profiles based on these ranges. These results suggest a large core (1730–1840 km), though their Bayesian method does not explicitly consider the influence of each parameter on the determined core size. Plesa et al. (2018) also found that the core must be large (>1800 km) based on thermal evolution modeling. Larger cores have lower CMB pressures, probably precluding a bridgmanite layer, though Bertka and Fei (1997) determined that the existence of Martian bridgmanite is also highly temperature dependent.

Here we present a new model of Martian core formation that improves upon previous studies by implementing multi-stage differentiation with comparisons to a large suite of major, minor, and trace elements. The core and mantle compositions

predicted by this core formation model were used to construct forward models of modal mineralogy, density, and seismic velocity profiles for the Martian interior. We explicitly considered how planetary structure is influenced by core composition as well as geophysical parameters such as crustal thickness and thermal structure. Additionally, we introduced more realistic estimations of liquid Fe–S alloy densities at high *P*–*T*, improving our understanding of the core's physical properties. Assessing seismic properties across the model suite allowed for predictions of both body wave travel times and normal mode oscillation frequencies. These new self-consistent models of core formation, internal structure, and seismic properties help tie together the formation of Mars with its modern state and produce geophysical predictions that can be compared to seismic results obtained by the InSight mission.

2.2 Methods

We have constructed a model of multi-stage core formation to investigate Martian formational properties and a model of planetary physical structure to investigate geophysical properties of modern Mars. Further details on these, as well as our seismological calculations, can be found in Appendix A.

2.2.1 Modelling Core Formation

Chondritic primordial material was equilibrated at a single fO_2 to form planetesimals, which were sequentially added to the proto-Mars, and experimentally-determined metal–silicate partitioning data (Table A.1) were used to model the chemistry of core formation (Fischer et al., 2017; Rubie et al., 2011, 2015). In order to constrain the core formation conditions required to match the previously published SNC-based Martian mantle composition, we used the same bulk planetary composition

that Taylor (2013) proposed to explain the Martian mantle. This bulk composition was based on CI chondrites enriched in refectory elements (Mg, Al, Si, Ca, V, Cr, Fe, Co, Ni, W, Ti) by a factor of 1.9 to create relative depletions in more volatile elements (Na, P, S, K, Mn). Dynamical studies suggest that Mars likely did not experience giant impacts (e.g., O'Brien et al., 2014), so we constructed Mars from 1000 small impactors. The final composition of Mars is insensitive to the specific impactor quantity for large numbers of impactors.

In each accretionary step, one planetesimal (the impactor) was equilibrated with proto-Mars (the target). Following the example of previous partial-equilibration models (e.g., Rudge et al., 2010), equilibration took place between the entire impactor mantle, a portion of the impactor core, and a portion of the target mantle; the core of proto-Mars was assumed to be undisturbed by impacts (Figure 1). In each step, metal–silicate equilibration took place at a constant fraction of the growing CMB pressure and at the liquidus temperature. Pressure at the CMB increased linearly with mass, using 21 GPa as the final CMB pressure (Rivoldini et al., 2011). Mg, Al, Ca, Na, and K were assumed to be perfectly lithophile. In each step, major elements Si, Fe, O, and Ni were partitioned first, allowing fO_2 to evolve self-consistently following the methodology of Rubie et al. (2011) as updated in Fischer et al. (2017), then S and the trace elements were partitioned. Finally, the unequilibrated portion of the impactor core and the metallic portion of the equilibrated material were added to the proto-Martian core, and the unequilibrated portion of the target mantle and the silicate portion of the equilibrated material were combined to form the proto-Martian mantle. This procedure assumes a homogenous accretion scenario and constrains only the average conditions of Martian core formation. Nonetheless, homogenous accretion may be a good approximation if

Mars is a stranded planetary embryo that accreted most of its mass oligarchically (e.g., Dauphas and Pourmand, 2011).

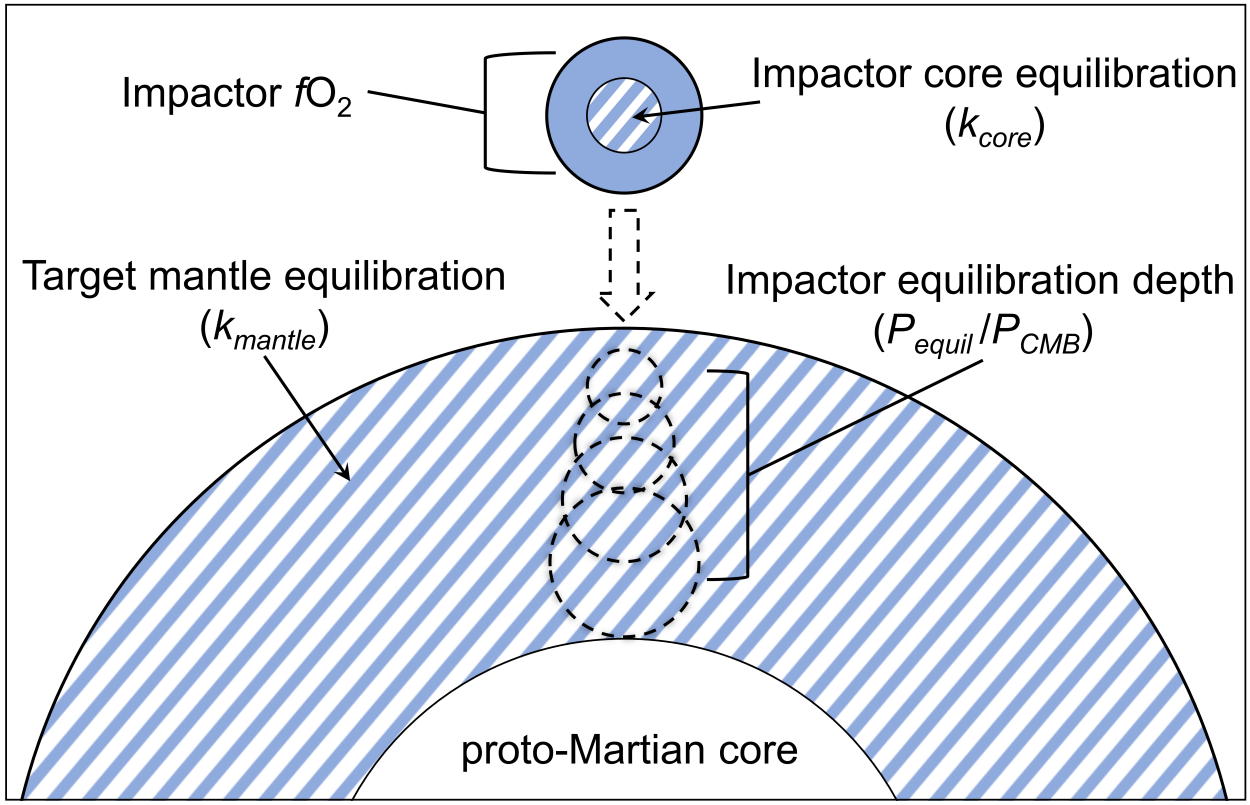

Figure 2.1: Schematic of a small body (the impactor) accreting to proto-Mars (the target) in the core formation model. Solid shaded regions equilibrate fully, unshaded ones do not equilibrate, and stripes denote partial equilibration. In this homogenous accretion scenario, the values of the parameters represent effective averages over the conditions of Martian core formation.

Adjustable parameters in the model include: the equilibration fraction (the portion that participates in the metal–silicate reaction) of the impactor core (denoted by k_{core}) and target mantle (k_{mantle}); depth of equilibration, expressed as a fraction of the evolving CMB pressure (P_{equil}/P_{CMB}); and the initial oxidation state of the impactor bodies (Figure 1). To evaluate the sensitivity of the resulting compositions to these formational parameters and to constrain them, the equilibration fractions of the impactor core and target mantle were each varied in the range 0.1–1.0, the depth of

equilibration was varied in the range 0.01–1.0, and the constant initial fO_2 of the accreted material was varied from IW–3 to IW. Temporal changes in the fO_2 of accreting material were not considered. Compositional uncertainties due to the reported experimental uncertainties of the partition coefficients were evaluated using a Monte Carlo analysis.

2.2.2 Modelling Planetary Physical Structure

Using the core and mantle compositions calculated in the core formation model, present-day radial profiles of density and seismic wave speeds were constructed for a range of geophysical parameters. The Martian temperature profile (the "areotherm") was calculated based on an adiabat from the median CMB conditions of Rivoldini et al. (2011) (~21 GPa and ~2000 K). These correspond to a mantle potential temperature of ~1600 K, consistent with previous estimates (e.g., Nimmo and Faul, 2013; Zheng et al., 2015). The lithospheric thermal boundary layer was approximated as a layer of linearly increasing temperature that intersects the adiabat at ~200 km, the estimated base of the thermal boundary (e.g., Khan et al., 2018). Using these temperatures, mantle profiles of modal mineralogy, rigidity, density, and seismic wave speeds were calculated using Perple_X (Connolly, 2009) with the thermophysical dataset of Stixrude and Lithgow-Bertelloni (2011).

The Martian core was assumed to be a homogenous liquid Fe–S alloy, with the S fraction specified by the core formation model. Density–pressure relationships for the core were calculated by reference to published Fe–S alloy equations of state. The core S content is a function of the formational parameters discussed above, so it was necessary to interpolate between equations of state for several alloys to calculate densities over a range of compositions. We used four equations of state: γ-Fe

(Komabayashi and Fei, 2010), Fe_3S (Seagle et al., 2006), FeS (Urakawa et al., 2004), and FeS_2 (Thompson et al., 2016). These equations of state all describe solids, so we applied a correction for the difference in molar volume between these and liquid alloys using the Clapeyron equation, the Fe–S eutectic melting curve (Campbell et al., 2007), and Fe–S ambient latent heat (Mare et al., 2014). We also performed calculations holding the volume change of melting ($\Delta V_{melting}$) fixed to various values spanning the range of $\Delta V_{melting}$ between those of Fe and FeS (e.g., Anderson and Ahrens, 1994; Komabayashi and Fei, 2010; Nishida et al., 2011). While it would have been more straightforward to use liquid equations of state, there are not enough data to adequately constrain liquid Fe–S alloy densities over a range of compositions (Section 2.4.4).

Pressure versus density and pressure versus velocity profiles were converted to functions of depth with a thin-shell model of self-gravitation (see Appendix A.3). Each constructed profile corresponds to a specific set of physical (crustal thickness, mantle temperature, core temperature, $\Delta V_{melting}$ of Fe–S alloys) and formational (core S content) parameters. To test the sensitivity of core radius and density/velocity structure to these parameters, crustal thickness was varied as 25–85 km, mantle potential temperature was varied as 1500–1800 K, the temperature contrast across the CMB was taken to be 0–600 K, $\Delta V_{melting}$ was taken to be 2–5%, and core S was varied as 12–21 wt%. Each combination of parameters implies a value for MOI and k_2, which can be compared to measurements of Mars-orbiting satellites (Konopliv et al., 2011, 2016) (Section 2.4.4).

2.3 Martian Core Formation

The composition of the Martian mantle can be used to constrain the conditions of core formation. These conditions can then be used to constrain the composition of the core.

2.3.1 Bulk Mantle Composition and Implications for the Formation of Mars

An example of a Martian mantle composition produced by this model is shown in Figure 2.2. At time of writing, Taylor (2013) is the only study that reports uncertainties on the Martian mantle composition (unlike, e.g., Dreibus and Wänke, 1985; Lodders and Fegley, 1997; Sanloup et al., 1999). Therefore, we use the Taylor (2013) bulk composition (refractory-enriched CI) and compare to that study's mantle assemblage. We obtain good agreement with Lodders and Fegley (1996) and Sanloup et al. (1999) when we instead use their bulk compositions. Calculated mantle abundances of major, minor, and trace elements are consistent with those of Taylor (2013), except for K (Figure 2.2). Taylor (2013) treated K uniquely, obtaining its abundance from gamma ray spectroscopy measurements of the surface K/Th ratio, this methodological difference likely accounts for the discrepancy. To constrain conditions of formation and differentiation, first the fO_2 at which primordial material equilibrated was adjusted to match the reported FeO content of the Martian mantle. Its mantle FeO content implies that Mars was built of material with an initial oxidation state of IW–1.4 to IW–0.9, which results in a final core mass fraction of 0.19–0.25 (Figure 2.3a). The higher initial fO_2 and smaller core relative to Earth (e.g., Fischer et al., 2017; Rubie et al., 2011, 2015) reflects the accretion of relatively oxidized primordial material, which likely originated further from the Sun.

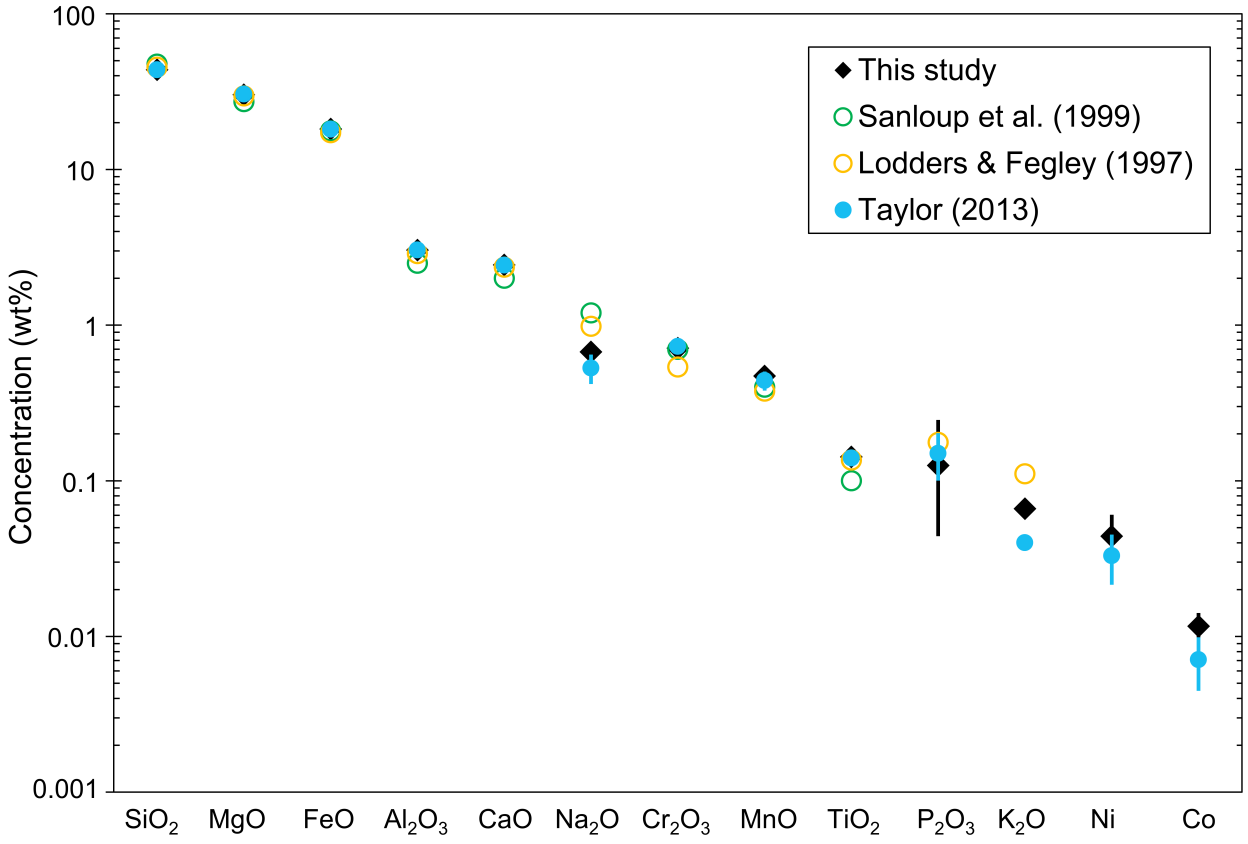

Figure 2.2: Comparison of bulk mantle compositions between this study and models based on SNC elemental abundances (Taylor, 2013) or O isotopes (Lodders and Fegley, 1996; Sanloup et al., 1999). Error bars correspond to 95% confidence intervals of our Monte Carlo error analysis for this study and reported 2σ uncertainties for Taylor (2013). Calculation was performed for k_{core} = 0.9, whole mantle equilibration (k_{mantle} = 1), P_{equil}/P_{CMB} = 0.55, and initial fO_2 of IW–1.12.

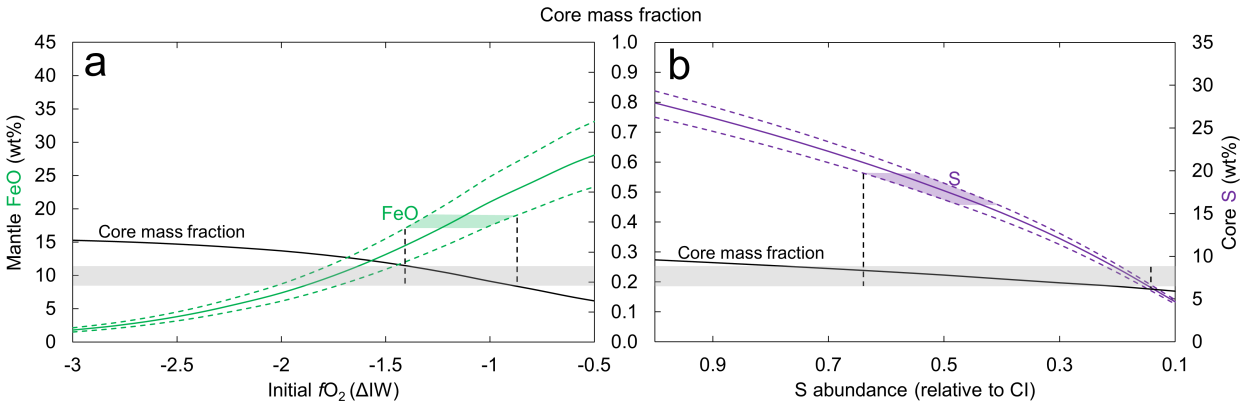

Figure 2.3 a: The tradeoff between initial fO_2 of primordial material and partitioning of Fe between mantle and core. The green shaded region indicates the range of calculated FeO contents that are consistent with Taylor (2013), which constrain the initial fO_2 to be IW–0.9 to IW–1.4. The corresponding core mass fraction is 0.19–0.25 (horizontal shaded bar) for a bulk S content of 4.2 wt%. **b:** The tradeoff between bulk S content and S content of the core (purple). The same range in core mass fraction as in **a** (black curve and horizontal shaded bar) can be produced by varying the total S content of bulk Mars in the range 0.15–0.65 × CI for an initial oxygen fugacity of IW–1.12. The purple shaded region represents the range of core S contents from the core formation model. Dashed lines represent 95% confidence intervals. Calculation was performed for $P_{equil}/P_{CMB} = 0.55$, $k_{mantle} = 1$, and $k_{core} = 0.9$.

Constraints on the degree of equilibration were obtained by comparing the calculated mantle compositions with literature values (Figure 2.4a). Possible values of k_{core} are 0.84–1.0 for whole-mantle equilibration (k_{mantle} =1), based on matching the mantle abundances of TiO_2, S, and Co (within their 95% confidence intervals); other elements are consistent with this range but do not provide such tight constraints. This degree of metal equilibration is significantly higher than the k_{core} of 0.2–0.55 found for Earth (Fischer and Nimmo, 2018). Earth's lower k_{core} is consistent with the accretion of giant differentiated impactors, whose large cores may not have efficiently emulsified in the terrestrial magma ocean. A high k_{core} for Mars is consistent with the accretion of smaller bodies, possibly including undifferentiated impactors that would effectively exhibit $k_{core} \approx 1$. Varying k_{mantle} does not significantly change the mantle composition for

values above ~0.4, consistent with its limited compositional effect above a certain threshold for the Earth (Fischer et al., 2017). Reducing the degree of silicate equilibration requires a corresponding increase in k_{core}.

An analogous procedure was used to constrain the depth of metal–silicate equilibration (Figure 2.4b). Simultaneously matching the Martian mantle abundances of Ni, Co, and S requires that P_{equil}/P_{CMB} falls in the range 0.42–0.60 (for k_{core} = 0.9 and k_{mantle} = 1); again, other elements are consistent with this range, but do not further constrain it. This pressure range implies that, on average, equilibration took place in a deep magma ocean but shallower than the core–mantle boundary, consistent with previous arguments for a deep Martian magma ocean (e.g., Dauphas and Pourmand, 2011). A similar relative depth of equilibration was found for the Earth using comparable models (Fischer et al., 2017; Rubie et al., 2011, 2015); this may suggest a similar relative depth of melting on the two planets. This range implies an average equilibration pressure similar to the results of single-stage partitioning studies (e.g., Rai and van Westrenen, 2013; Righter and Chabot, 2011). Mars likely formed from small bodies (e.g., Kobayashi and Dauphas, 2013), but single-stage models necessarily partition elements at a fixed fO_2 and do not incorporate P–T changes as a planet grows. The more realistic model presented here includes these effects, and its agreement with the single-stage models reinforces the robustness of our results.

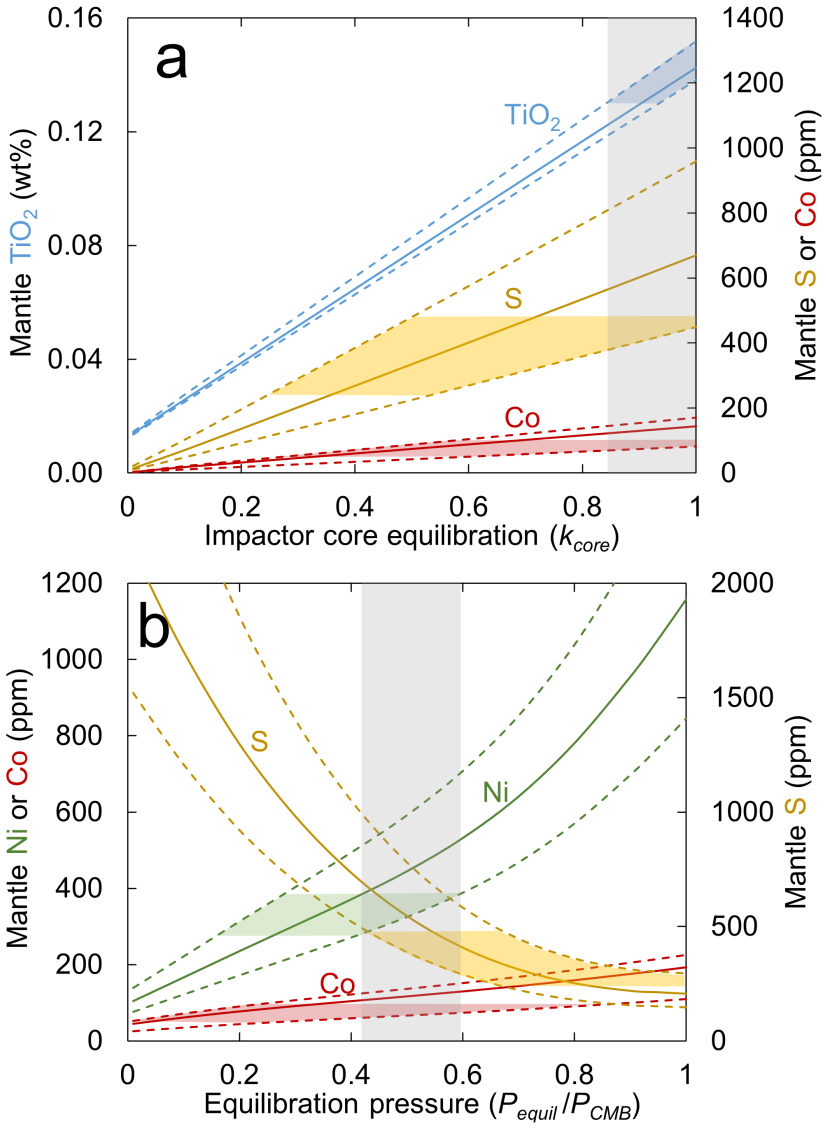

Figure 2.4 a: Mantle TiO_2 (blue), Co (red), and S (yellow) as a function of the degree of impactor core equilibration, k_{core}. Dashed lines are 95% confidence intervals. Colored regions illustrate where the calculated compositions match the values of Taylor (2013) for TiO_2 and Co and Wang and Becker (2017) for S. The grey shaded bar indicates the k_{core} range where all three elements can be matched. These values of k_{core} suggest that most metal was equilibrated before merging with the Martian core. Calculation was performed for whole mantle equilibration (k_{mantle} = 1), P_{equil}/P_{CMB} = 0.55, and initial fO_2 of IW–1.12. **b:** Mantle Ni (green), Co (red), and S (yellow) as a function of core–mantle equilibration pressure (expressed as a fraction of the evolving CMB pressure). Colored regions illustrate where the calculated compositions match the values of Taylor (2013) for Ni and Co and Wang and Becker (2017) for S. These pressures suggest that equilibration occurred in a deep magma ocean, but not at the core–mantle boundary. Calculation was performed for k_{core} = 0.9, k_{mantle} = 1, and initial fO_2 of IW–1.12.

2.3.2 Light Elements in the Martian Core

The core formation conditions implied by the Martian mantle composition indicate that S is the dominant light element in the core, consistent with previous studies (e.g., Lodders and Fegley, 1996; Sanloup et al., 1999; Steenstra and van Westrenen, 2018; Taylor, 2013; Wänke and Driebus, 1985). Sulfur is siderophile at the P–T–fO_2 conditions of Martian core formation, so the majority of Martian S must be in the core. However, the mantle abundance also appears to be greater than that of the Earth (e.g., Wang and Becker, 2017), implying that bulk Mars is relatively sulfur rich. The range of core mass fractions implied by the mantle FeO content, 0.19–0.25 (Section 2.3.1), can be produced by a range of volatile element depletion factors of 0.15–0.65× CI for an initial oxygen fugacity of IW–1.12 (Figure 2.3b). Taylor (2013) argued for a refractory element enrichment of 1.9× CI (equivalent to a volatile element depletion of 0.6× CI) based on a survey of volatile lithophile element abundances. Enriching Mars in refractory elements by this factor leads to a core S content of 18–19 wt% (95% confidence interval, see Table A.2). This corresponds to a mantle with 500 ppm S and a bulk Mars with 4.2 wt% S, within the bulk abundance estimates of Steenstra and van Westrenen (2018). Tuff et al. (2013) suggested a mantle with an order of magnitude more S (2500 ppm), but such a composition would require a far higher S abundance than any meteorite group (i.e., >20 wt% in bulk Mars) if the mantle S content is due to core formation. If Mars is assumed to have bulk S equivalent to an H chondrite, it would have a core S content of 12 wt%. Bulk S content equivalent to a pristine EH chondrite results in a core S content of 21 wt%; this may be taken as the upper limit for core S in a chondritic Mars since EH is the most S-rich of all chondrite groups (Lodders and Fegley, 1998).

The Martian core contains little O (<1 wt%; Table A.2) despite its oxidizing core formation conditions. This is due to the relatively modest *P*–*T* conditions of metal–silicate equilibration on Mars, since O partitions more strongly into iron alloys at higher *T* (e.g., Fischer et al., 2015; Ricolleau et al., 2011; Rubie et al., 2004). Steenstra and van Westrenen (2018) calculated core O content as a function of equilibration pressure in a single-stage model; at 13 GPa they found similar or slightly higher oxygen abundances compared to those found here (~0.4–1.3 wt%). Low oxygen abundances in the Martian core agree with some previous studies (e.g., Rubie et al., 2004), though some predicted O at the few-percent level (e.g., Tsuno et al., 2011) due to an assumption of core–mantle equilibration at the modern CMB (inconsistent with our findings; Figure 2.4b). The other light element considered here, Si, only enters the Martian core at trace levels (Table A.2). Like O, Si is less siderophile at lower temperatures, but it is also less siderophile at higher fO_2 (Geßmann et al., 2001; Fischer et al., 2015; Ricolleau et al., 2011), further reducing its core abundance.

C and H partitioning were not modeled despite suggestions that these may be present in the core with greater-than-trace abundances (e.g., Chi et al., 2014; Zharkov and Gudkova, 2005). There are few constraints on the planetary or mantle abundances of these highly volatile elements, and thus it is difficult to determine their total budgets. Qualitatively, Mars is too small and S-rich to dissolve substantial H in its core, with Clesi et al. (2018) estimating 60 ppm. The solubility of C is also much reduced in S-rich core alloys (Tsuno et al., 2018). For a nominal bulk C content of 1000 ppm, Tsuno et al. (2018) found that a Martian core at IW–1.0 with 16 wt% S would have ~0.5 wt% C; this may be taken as an upper bound for the more S-rich core presented here. This estimation may be too low if Mars is C-rich; Steenstra and van Westrenen (2018) found that bulk Martian compositions with 2500–4000 ppm C can have up to 1.4 wt% C

in the core. Better constraining the abundances and partitioning of these highly volatile elements is a target for future studies.

2.4 Geophysical Properties of the Martian Interior

The compositions predicted by the core formation model were used to construct phase assemblages and produce density and velocity profiles (Figures 2.5 and 2.6) of the Martian interior (Section 2.2.2). In addition to composition, these profiles depend on various geophysical properties of the Martian interior, which can be constrained by calculating each profile's mass, radius, MOI, and k_2. The resulting solution space allows for predictions of core radius and seismic properties.

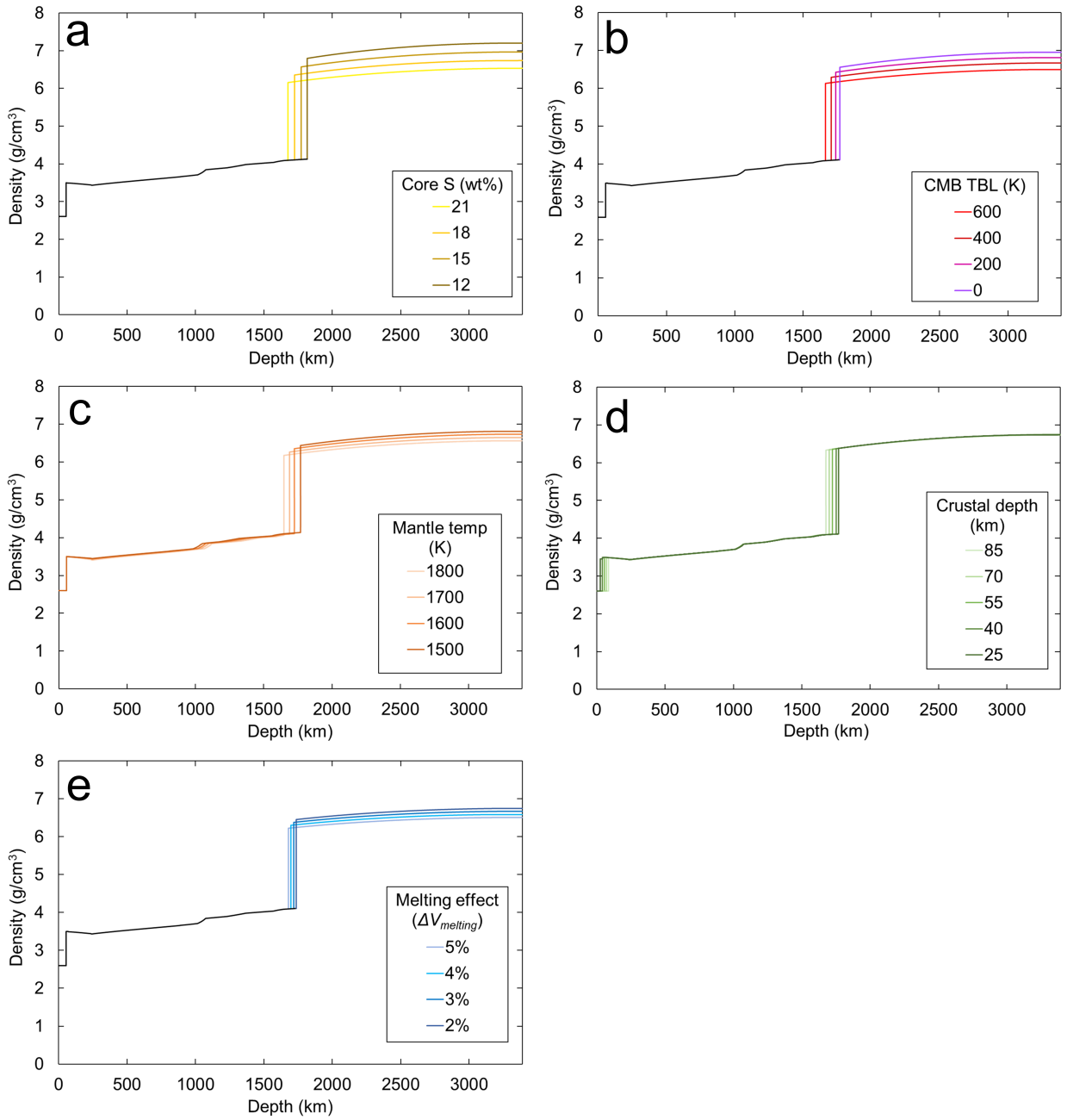

Figure 2.5: Martian density profiles calculated by varying a single parameter at a time: core S content (**a**), temperature contrast between the lowermost mantle and uppermost core (assuming a thin thermal boundary layer at the CMB) (**b**), mantle potential temperature (**c**), crustal thickness (**d**), and $\Delta V_{melting}$ of Fe–S alloys (**e**). Calculations were performed for a core S content of 18 wt%, CMB TBL of 300 K, mantle potential temperature of 1600 K, crustal thickness of 55 km, and $\Delta V_{melting}$ = ~3% except as noted.

2.4.1 The Crust

The outer layers of a planet have an outsized influence on the planet's MOI due to their large radial distance from the center of gravity. Konopliv et al. (2011) determined the Martian MOI to be 0.3644 ± 0.0005 but found that altering crustal thickness by 25 km changes the MOI by 0.0017. Some recent studies use an even tighter bound on MOI (Khan et al., 2018), but regardless of precision, uncertainties in crustal structure dominate inertia-based constraints on models of the Martian interior. Determining the average crustal properties pertinent to a spherically symmetric model is complicated by the fact that the Martian crust contains a significant hemispheric dichotomy, various volcanic provinces, impact basins, and heterogeneous regolith. Constraints from orbital gravity measurements and surface topography imply that mean crustal thickness must lie within 57 ± 24 km (Wieczorek and Zuber, 2004). We find that within a narrow range of crustal thicknesses (55 ± 10 km), the Martian MOI can be matched with a wide range of core sizes (1500–1850 km). Fortunately, InSight measurements are likely to better constrain crustal thickness beneath the landing site (Panning et al., 2017), which will allow for tighter constraints on core size.

2.4.2 The lithospheric boundary layer

Mars is a stagnant lid planet and is inferred to have a laterally variable lithosphere up to 300 km thick (e.g., Grott et al., 2013). This is a thick thermal boundary layer on a small planet, so the accompanying low-velocity zone (LVZ) may be of first-order importance for Martian seismology (Section 2.4.6; Figure 2.6). Since the magnitude of the velocity decrease is dependent on the thermal structure of the lithosphere, mantle potential temperatures may be inferred by measuring the LVZ's seismological effects (Zheng et al., 2015).

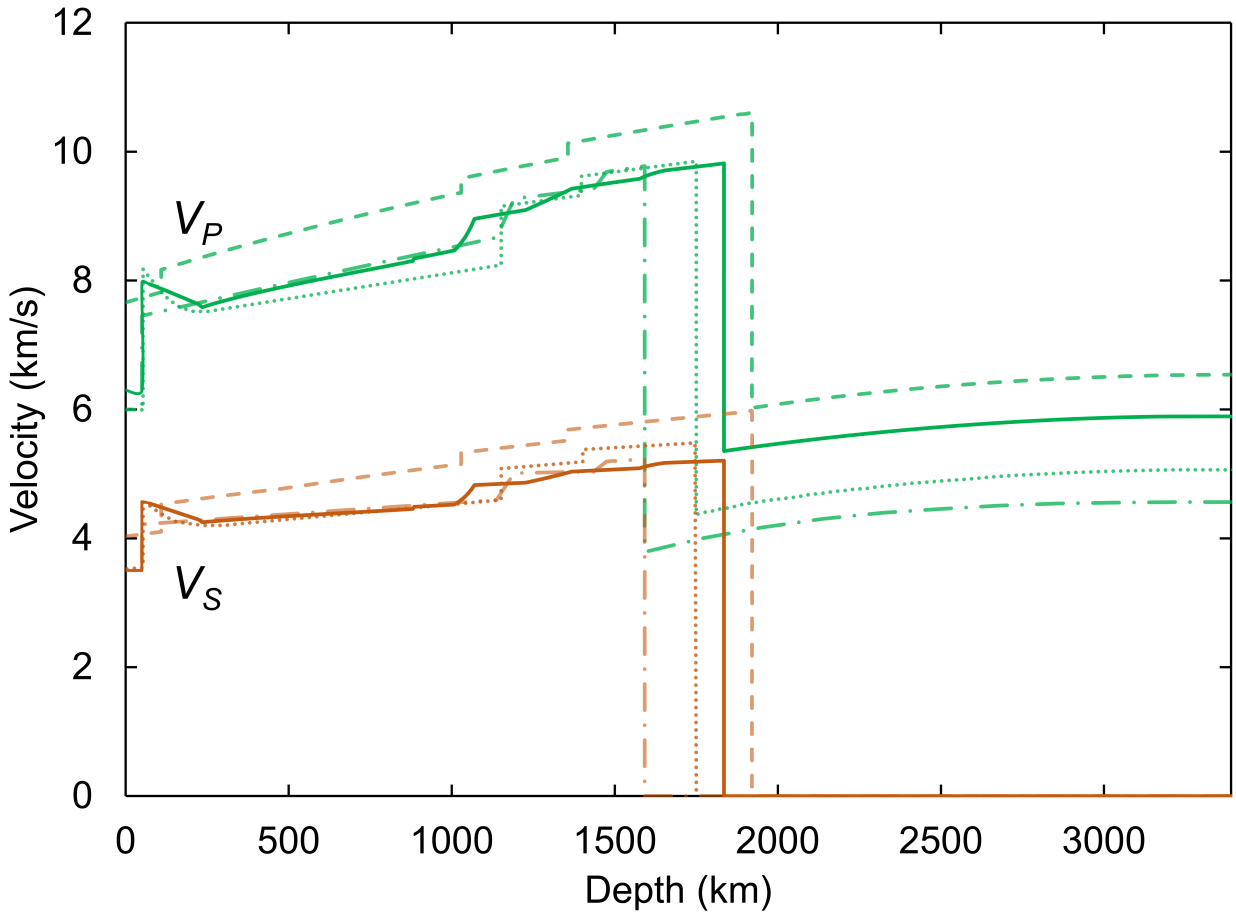

Figure 2.6: Comparison of Martian compressional wave velocity (V_P, green) and shear wave velocity (V_S, brown) profiles between this study (solid lines) and several previous studies. Dashed lines: Sohl and Spohn (1997) "Model A". Dotted lines: Zheng et al. (2015) "LVZ Model". Dot-dashed lines: Zharkov and Gudkova (2005) "M14_3 Model". The profile for this study corresponds to a core sulfur content of 18 wt%, crustal thickness of 50 km, thermal boundary layer temperature contrast of 300 K, mantle potential temperature of 1600 K, and $\Delta V_{melting}$ = 3%. The low-velocity zone in the upper mantle is a consequence of the steep lithospheric temperature profile within the stagnant lid on Mars (Section 2.4.1).

The magnitude of this effect, however, cannot be well-constrained with our current knowledge of Martian temperature and structure. The calculations shown here use an upper mantle thermal boundary layer thickness of 200 km (Khan et al., 2018) and a range of mantle potential temperatures around 1600 K (Nimmo and Faul, 2013). Changing the mantle potential temperature at a constant lithospheric thickness

requires changing the slope of the lithospheric temperature profile (Figure A.3). Increasing potential temperature by 100 K with a 200 km lithospheric boundary decreases velocities in the LVZ by 0.2 km/s for compressional waves and 0.1 km/s for shear waves. These effects may be complicated by variations in lithospheric thickness due to the hemispherical dichotomy and the Tharsis volcanic province.

2.4.3 Lowermost Mantle Conditions

There is some disagreement as to whether the Martian mantle contains bridgmanite, the most abundant mineral of Earth's lower mantle. Some studies find that the *P*–*T* conditions of the lowermost Martian mantle lie within the bridgmanite stability field (e.g., Bertka and Fei, 1998), some do not (e.g., Khan and Connolly, 2008; Khan et al., 2018; Sohl and Spohn, 1997), and some are inconclusive (e.g., Bertka and Fei, 1997; Rivoldini et al., 2011). The experimental work of Bertka and Fei (1997) and Duncan et al. (2018) suggests that bridgmanite stability begins at ~23 GPa in the Martian mantle. This CMB pressure corresponds to a core radius of ~1500 km; such a core is smaller than any in Figure 2.5 and is difficult to reconcile with geophysical constraints (see Section 2.4.4) (e.g., Khan et al., 2018). A bridgmanite layer would affect mantle convection and reduce heat flow from the core, impacting both the areotherm and the temperature contrast across a CMB thermal boundary layer (Bruer et al., 1998; Michel and Forni, 2011). Thus, if a bridgmanite layer does exist, its thickness will strongly constrain mantle temperature (Bertka and Fei, 1997); the possibility of such a layer in the past may have influenced the Martian mantle's convective regime towards single-plume upwelling (Sohl and Spohn, 1997).

2.4.4 Core Radius

We have evaluated the effects of five parameters on the core radius of Mars: the thickness of the crust, temperatures of the mantle and core, sulfur content of the core, and densities of liquid Fe–S alloys. All core radii calculated here are consistent with the core mass fractions determined in the core formation model (Section 2.3.1; Figure 2.3).

(1) Thickness of the crust. A thick layer of relatively light crustal material requires a larger core to maintain consistency with the Martian radius and bulk density. Varying crustal thickness in the range 25–85 km (Wieczorek and Zuber, 2004) corresponds to a change in core radius of 94 km, with thicker crusts corresponding to larger cores. The planet's MOI is very sensitive to crustal parameters, so only a small portion of this range of crustal thicknesses is consistent with measurements (Section 2.4.3).

(2) Temperature of the mantle. Martian internal temperature profiles depend on the thermal history of the planet, its radiogenic heat production, and its convective regime. These features are not well constrained, making temperatures difficult to evaluate. Lowermost mantle temperatures of 1800–2100 K bracket the "hot" and "cold" endmembers of Rivoldini et al. (2011). This range corresponds to mantle potential temperatures of 1500–1800 K, consistent with published estimates (e.g., Nimmo and Faul, 2013). This temperature range corresponds to a change in core radius of 122 km, with larger cores corresponding to hotter mantles.

(3) CMB thermal boundary layer. Previous studies (e.g., Khan et al., 2018) have generally not considered any significant CMB temperature contrast due to the absence of a Martian geodynamo (Williams and Nimmo, 2004). It is possible that the core is hotter than the overlying mantle, leading to a thin

region of rapidly increasing temperatures, as in Earth's lowermost mantle. We have investigated models with uppermost core temperatures 0–600 K above the lowermost mantle temperature, within the allowable range of CMB heat flow (Appendix A.6). This range corresponds to a change in core radius of 103 km, with hotter cores being less dense and thus larger.

(4) Sulfur content of the core. Since S is lighter than Fe, an S-rich core will have a reduced alloy density, and thus must be larger. A core S content of 12–21 wt% encompasses a range of 2.0–5.4 wt% bulk Martian S, corresponding to the difference between the most S-poor (H) and S-rich (EH) chondrites (Lodders and Fegley, 1998). This range changes core radius by 141 km.

(5) Effect of melting on Fe–S alloy densities. Since the Martian core is thought to be entirely molten (Konopliv et al., 2011), its geophysical parameters must be calculated with reference to liquid Fe–S alloys. Unfortunately, there are few equation of state studies in this liquid system, and the available studies generally do not extend to the relevant *P*–*T* conditions. Using the anomalously low extrapolated densities of these extant liquid data, as some previous studies have done (e.g., Khan et al., 2018; Rivoldini et al., 2011), may lead to inaccurate interpretations of the Martian core density (Figure 2.7). Several studies have pointed out that the volume change between solid and liquid Fe–S alloys should be quite small at high pressures, on the order of 1.5% for Earth's CMB (Seagle et al., 2006) and only slightly greater for Martian CMB conditions. The ambient $\Delta V_{melting}$ is ~16% for FeS (Kaiura and Toguri, 1979), dropping to only ~4–5% at a few GPa (Nishida et al., 2011). Since $\Delta V_{melting}$ of Fe is ~2% at 20 GPa (Anderson and Ahrens, 1994; Komabayashi and Fei, 2010), we have chosen to use the interpolation of the

solid densities and correct for a melting effect based on $\Delta V_{melting}$ values of 2–5%, corresponding to a change in core radius of 56 km. For profiles where $\Delta V_{melting}$ was not varied, we estimated $\Delta V_{melting}$ from the eutectic melting curve of Fe–S alloys (Campbell et al., 2007), leading to a mean $\Delta V_{melting}$ of ~3% for Martian core pressures, consistent with this range.

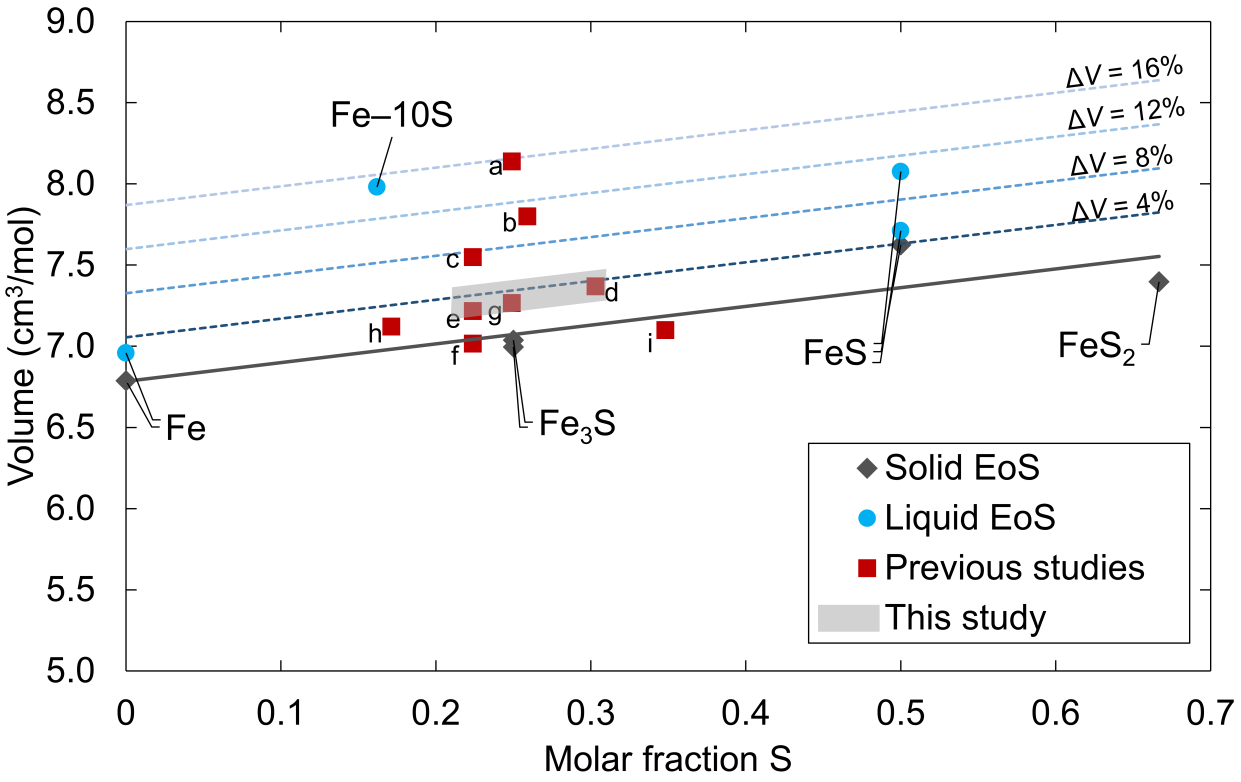

Figure 2.7: Densities of solid (Chen et al., 2007; Kombayashi and Fei, 2010; Seagle et al., 2006; Thompson et al., 2016; Urakawa et al., 2004) and liquid (Anderson and Ahrens, 1994; Balog et al., 2003; Morard et al., 2018; Nishida et al., 2011) alloys in the Fe–S system calculated from equations of state at 20 GPa and 2000 K. The solid line is a linear fit to the solid data, and the dashed lines are offset from this line according to fixed $\Delta V_{melting}$ up to 16%, the 1 bar value for FeS (Kaiura and Toguri, 1979). The grey box indicates the range of S consistent with a chondritic Mars and the range of $\Delta V_{melting}$ between that of Fe and FeS at these conditions. All liquid equations of state have been extrapolated beyond the pressure conditions of the original measurements, save for the Fe–10S study (Balog et al., 2003), which was based on sink/float experiments with large (~20%) error bars. Using this data point to derive the properties of the Fe–S alloy (Khan et al., 2018; Rivoldini et al., 2011) results in an implied $\Delta V_{melting}$ greater than that of FeS, which is physically unlikely. Red squares represent some previous models of the Martian core alloy (**a**: Rivoldini et al., 2011; **b**: Khan et al., 2018; **c**: Sohl and Spohn, 1997; **d**: Zharkov and Gudkova, 2005; **e**: Kavner et al., 2001; **f**: Bertka and Fei, 1998; **g**: Sanloup et al., 1999; **h**: Lodders and Fegley, 1997; **i**: Khan and Connolly, 2008). Studies **a**–**f** are plotted at the same *P*–*T* as the equation of state points, while studies **g**–**i** have fixed (*P*–*T* independent) core densities.

One of the geophysical constraints on the Martian interior comes from its deformation in response to tidal forcings from the Sun, Phobos, and Deimos. The tidal Love number k_2 has been determined from spacecraft and lander tracking data, most recently in Konopliv et al. (2016), which reported a value of 0.169 ± 0.006. To evaluate the consistency between this value and our profiles, we used a simplified two-layer parameterization to calculate k_2 (Appendix A.5). The dissipation of tidal energy within Mars is dependent on the rigidity and relative sizes of the core and mantle, with more rigid mantles requiring larger fluid core sizes to match k_2. Given this tradeoff, a 10% change in mean mantle rigidity would require a ~6% change in fluid core radius to match the observed k_2 value for plausible Martian core sizes. If the Martian mantle accurately reflects the volumetrically-averaged shear modulus of 73 GPa calculated here, then the core should be 1690–1870 km in radius (Figure A.4). It is possible to produce a core within this size range through various combinations of the parameters considered above, even accounting for the constraint on crustal thickness from the MOI. The relationship between core radius and the geophysical and geochemical parameters considered here is illustrated in Figures 2.8 and A.5, and can be parameterized by the following equation:

$$R_{core} = 564(22) + 1.49(5)\, d_{crust} + 10.1(1.5)\, C_{core}^{S} + 0.183(43)(C_{core}^{S})^2 + 0.115(10)\, \Delta T_{TBL} + 0.000108(8)\, (\Delta T_{TBL})^2 + 0.423(12)\, T_P + 14.8(1.1)\, \Delta V_{melting} + 0.337(59)\, \left(\Delta V_{melting}\right)^2 \quad (2.1)$$

where R_{core} is the radius of the core (km), d_{crust} is the thickness of the crust (km), C_{core}^{S} is the S content of the core (wt%), ΔT_{TBL} is the temperature contrast across the core–mantle thermal boundary layer (K), T_P is the mantle potential temperature (K), and $\Delta V_{melting}$ is the core alloy's volume change of melting (%; e.g., for a 2% volume change

of melting, $\Delta V_{melting}$ = 2). Numbers in parentheses represent one standard deviation on the last digits. This equation reproduces our geophysical model with a root mean squared misfit of 9 km for core radii of 1450–2000 km and the parameter ranges listed earlier in this section. It should not be applied to core sizes or parameter values outside these ranges. Future seismological constraints on crustal thickness and core radius can be inserted into this equation to help constrain geophysical properties of the Martian interior.

It is possible that the Martian mantle is less rigid than the melt-free, anhydrous, infinite-frequency idealization depicted here and in other studies. Shear moduli are lowered by the presence of water or partial melts in the mantle. Since many thousand ppm of water are needed to reduce the shear moduli of major mantle minerals by a few percent (e.g., Jacobsen et al., 2008; Wang et al., 2003), the 300 ppm water suggested to reside in the Martian mantle (Taylor, 2013) would not significantly reduce the mean shear modulus. Partial melting is another possibility; fluids cannot support shear stress, so partial melts would decrease the shear modulus of the mantle. Selecting a crust size of 55 km, potential temperature of 1600 K, core S content of 18 wt%, no TBL, and $\Delta V_{melting}$ of 3% returns a core 1620 km in radius. To match k_2, this core would require a mean mantle rigidity of 55 GPa, a 15% reduction from our nominal value, which may be obtained if there is volumetrically significant melting beneath the Martian lithosphere (Duncan et al., 2018). Ultimately, some combination of mantle-softening and core-expanding parameters must be responsible for the observed Martian k_2.

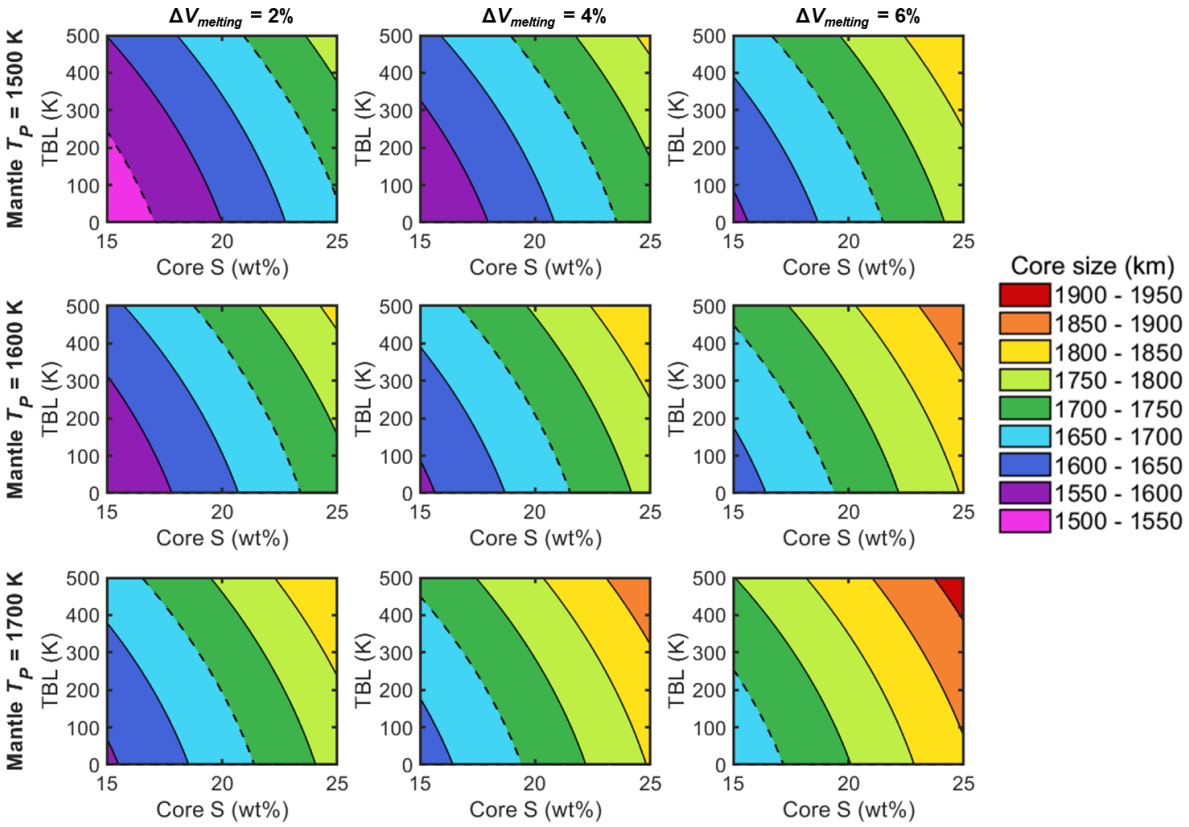

Figure 2.8: Tradeoffs between parameters that influence core size as parameterized by Equation 2.1. Each panel represents a fixed combination of $\Delta V_{melting}$ (constant throughout each column) and mantle potential temperature (constant throughout each row) and shows the combinations of core S content and CMB thermal boundary layer temperature contrast that can produce cores of a certain size. Each contour connects cores of the same radius. All panels correspond to a 55 km crust. For this crustal thickness, the approximate MOI constraints on core size (1550–1700 km) are indicated by dashed lines. Figure A.5 shows alternate versions of this figure corresponding to different crustal thicknesses.

2.4.5 Density and velocity profiles of the Martian interior

We consider the effects of the same five geochemical and geophysical parameters (crust thickness, core and mantle T, core S content, $\Delta V_{melting}$ of Fe–S) on the density and velocity structure of the Martian interior (Figures 2.5 and 2.6). Our results share much in common with previous LVZ models (Section 2.4.1), such as the large contrast

between adiabatic and lithospheric temperatures (Nimmo and Faul, 2013) and a gradual olivine–wadsleyite phase transition due to the high FeO content. This study predicts a V_S in the lowermost mantle that is smaller than V_P at the top of the core, whereas the otherwise similar LVZ model of Zheng et al. (2015) does not (Figure 2.6). The lower V_P of Zheng et al. (2015) is likely due to their use of FeS data for the thermophysical properties of the core alloy; FeS has a reduced density and bulk modulus compared to our composition.

2.4.6 Seismic Properties

Using the Mineos software (Masters et al., 2011), mode center frequencies for the suite of models have been calculated (Figure 2.9a and A.6). Overall, as expected, radial, core-sensitive, and Stonely modes are affected by adjusting the five parameters described above. Stonely modes are confined to the CMB and are very challenging to observe even on Earth. Modes with center frequencies below 5 mHz are unlikely to be detectable on Mars (Panning et al., 2017), but radial modes (on the left of Figure 2.9a) above this period may display changes in frequency of several percent. While not affected by the physical properties of the core itself, models with different crustal thicknesses and mantle potential temperatures will result in different frequencies for the fundamental modes, which are a target for observation (Bissig et al., 2018). Thus, any observations of normal modes on Mars will aid in discrimination between these different models of Martian formation.

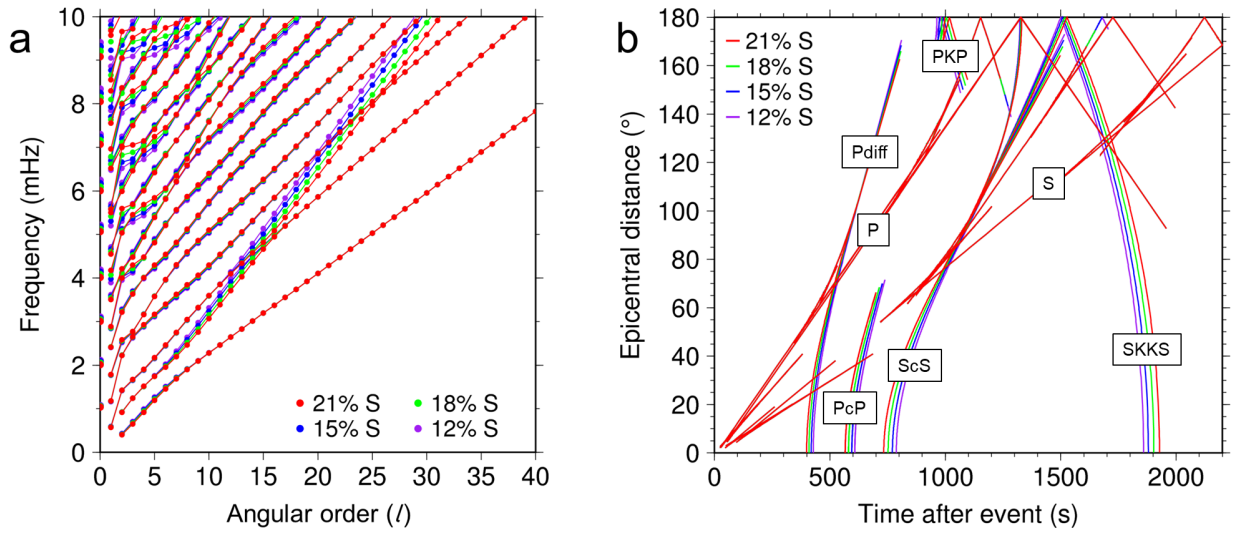

Figure 2.9: Seismological observables corresponding to four models with different core S contents. **a.** Normal mode center frequencies. The radial modes sit on the vertical axis ($l = 0$). InSight's broadband seismometer is expected to be unable to detect those modes under 5 mHz. **b.** Body wave travel time predictions for a 5 km deep marsquake. Major seismic phases are labelled. Calculations are performed for a CMB TBL of 300 K, mantle potential temperature of 1600 K, crustal thickness of 55 km, and $\Delta V_{melting}$ = ~3%.

Body wave travel times (Figure 2.9b) were calculated with the TauP toolkit (Crotwell et al., 1999), and show that a range of phases that reflect at the CMB or travel through the core are sensitive to the parameters explored here. As all the models investigated have an LVZ in the upper mantle (Section 2.4.1), shadow zones are evident in the travel time curves, most prominently in the direct S phase. Models with larger cores show earlier arriving core-reflected phases (e.g., ScS), whilst signals like PKP are delayed, as V_P in the core is lower than that of the mantle. SKS, which travels through the mantle as a shear wave and through the liquid core as a compressional wave, has delay times that vary little through the model suite, as V_S in the mantle is very close to V_P in the core.

The InSight site is roughly 20° from Cerberus Fossae, suggested to be a site of high seismic activity (Taylor et al., 2013). At such a distance, one of the clearest core signals we hope to observe will be ScS. Figure 2.10 shows predicted travel times for this phase at this epicentral distance for the full model suite. Nearly all the parameters behave in the same way: shorter ScS travel times correspond to larger core radii. Thus, even though all properties may not be discernable from such an observation, a travel time should permit us to roughly estimate core radius in this framework. Mantle potential temperature has effects on the radius–ScS time relationship that are not co-linear with the other parameters because a hotter potential temperature both decreases mantle velocities and changes core radius. Both crustal thickness and mantle potential temperature may be obtainable from other seismological observables (e.g., receiver function analysis for the former, and estimates of the sub-lithospheric LVZ for the latter), making this kind of analysis more valuable as the parameter space is narrowed down.

To use ScS travel time data, marsquakes must be relatively accurately located. The InSight mission requires that events be located within 25% of the true epicentral distance and 20% of the true back-azimuth. This level of error at an epicentral distance of 20° would change ScS arrival time by ~10 seconds, impairing the use of this kind of data even with an accurate seismic model. However, the results of the Marsquake Service blind test (Clinton et al., 2017) suggest that many Martian events may be located to a much higher degree of accuracy (van Driel et al., 2019). The utility of ScS observations in determining core radius will be determined by the degree of structural complexity, the level and distribution of seismicity on Mars, and the amount of "noise" or unwanted signal present as ScS is recorded.

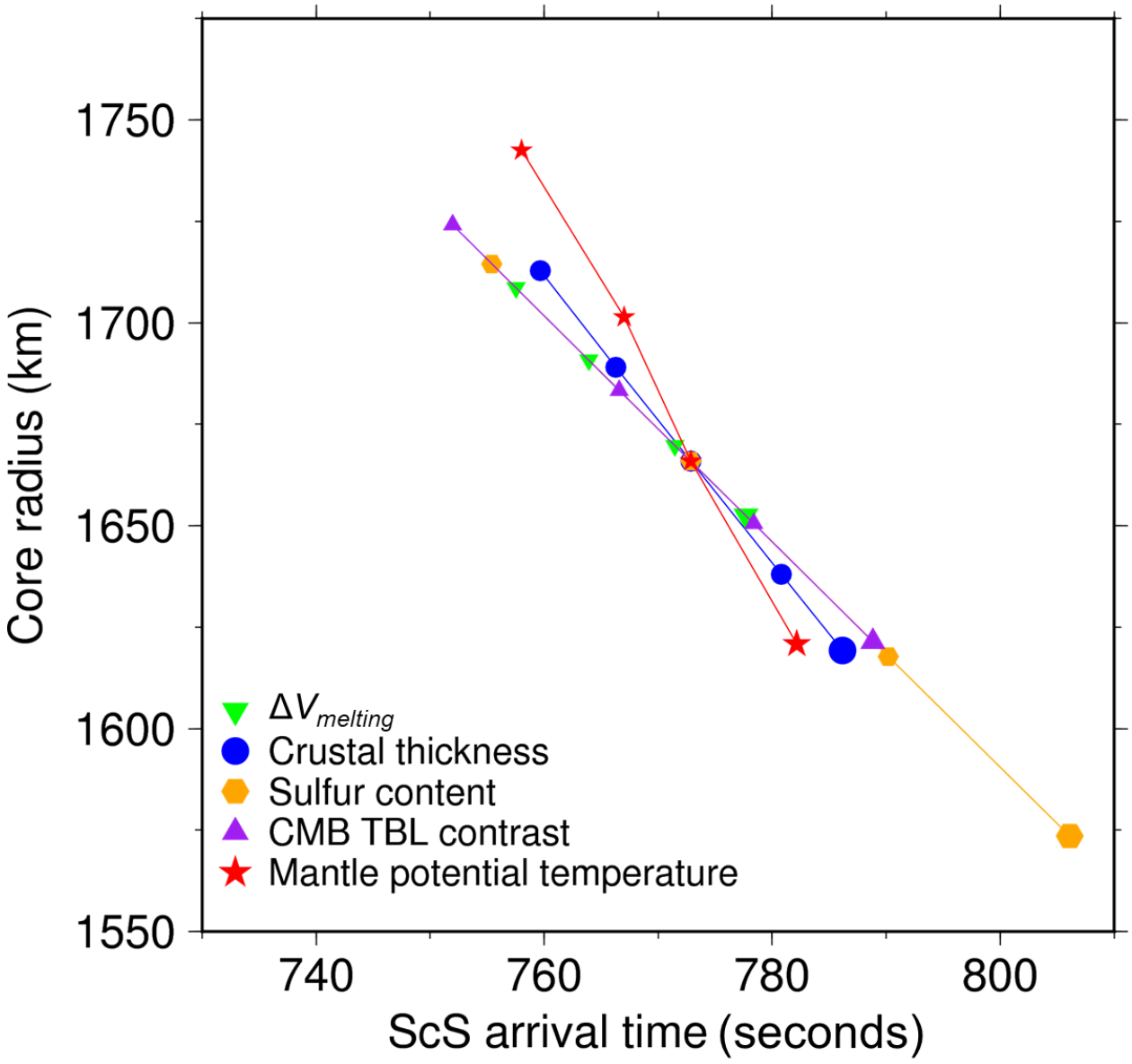

Figure 2.10: Relationship between core radius and predicted ScS arrival time. Travel times are predicted for an epicentral distance of 20˚ and a marsquake depth of 5 km. The impact of each of the five parameters on core radius is discussed in Section 2.4.4. In each case the larger symbol corresponds to the lowest value of the parameter that is being varied. Calculations were performed for a core S content of 18 wt%, CMB TBL of 300 K, mantle potential temperature of 1600 K, crustal thickness of 55 km, and $\Delta V_{melting}$ = ~3% except as noted.

2.4.7 Recent InSight Observations

Since the publication of our original study, InSight has completed its nominal mission period. Though large marsquakes proved to be quite rare, there was sufficient seismic activity to begin to piece together preliminary observational models of the interior (Banerdt et al., 2020). At least two studies have claimed to detect seismic evidence of the core–mantle boundary, one from ambient noise autocorrelations (Deng & Levander, 2020) and the other from ScS body waves (Stähler et al., 2021). Both studies find a core of ~1800 km radius, on the higher end of our predicted range. If this value is borne out, it would essentially confirm a core very rich in light elements, since there is no way for any other combination of parameters to produce a core so large (Figure 2.8). Using the 65 km average crust suggested by Deng & Levander (2020), a CMB TBL of 300 K, mantle potential temperature of 1700 K, and $\Delta V_{melting}$ = 5%, an 1800 km core implies a core S content of 21 wt% (Equation 2.1).

2.5 Conclusions

A multi-stage core formation model successfully reproduces meteorite-based abundances of most elements in the bulk silicate Mars and has been used to determine conditions of core formation and the composition of the Martian core. The high FeO content of the Martian mantle relative to that of Earth is due to formation from primordial material initially equilibrated at an oxygen fugacity between IW–0.9 and IW–1.4. On average, >84% of incoming metal was equilibrated with >40% of the Martian mantle, and equilibration took place at a depth of 42–60% of the evolving CMB pressure. The light element composition of the Martian core is dominated by S (18–19 wt%), with <1 wt% O and negligible Si, consistent with some previous models (e.g., Rubie et al., 2004; Steenstra and van Westrenen, 2018).

We have considered the possible ranges of various geophysical parameters (mantle and core temperatures, crustal thickness, and density of the Fe–S core alloy) and evaluated the effects of varying these parameters on the structure of the Martian interior. The core alloy densities calculated here are somewhat higher than those of previous studies due to different interpretations of the Fe–S equation of state data. Conservative parameter combinations imply that the core could be as small as 1620 km, though this size is not consistent with geophysical constraints on tidal Love number k_2 unless part of the Martian mantle is significantly softened by the presence of melt or water. Larger values of crustal thickness, mantle temperature, core temperature, or S content imply larger cores (Equation 2.1). If the Martian mantle is not subject to any softening effects, the core can be as large as 1870 km while maintaining consistency with geophysical observations. We have calculated seismic phase arrival times and planetary normal modes for a variety of parameter combinations to facilitate comparison with InSight's seismological measurements. Whatever the results of these observations, the actual core radius implies a particular combination of geophysical and geochemical parameters, meaning that constraints on core radius will help elucidate the thermal, physical, and compositional state of the Martian interior.

Acknowledgements

This work was supported by NASA grants NNX17AE27G and 80NSSC18K1633, National Science Foundation grants 1644399 and 1736046, and a National Science Foundation Graduate Research Fellowship (DGE1745303). We thank the editor, John Brodholt, for handling the original manuscript; two reviewers for their comments on the manuscript; Yingcai Zheng and Tamara Gudkova for providing their seismic models for comparison; and Francis Nimmo, Roger Fu, and Junjie Dong for their helpful advice. The original paper is InSight Contribution #110.

Chapter 3
Timing of Martian Accretion and Core Formation

Matthew C. Brennan[1], Rebecca A. Fischer[1], Francis Nimmo[2], David P. O'Brien[3]

[1]Harvard University, Department of Earth and Planetary Sciences

[2]University of California Santa Cruz, Department of Earth and Planetary Sciences

[3]Planetary Science Institute

The contents of this chapter are based on: "Timing of Martian Core Formation from Models of Hf–W Evolution Coupled with *N*-body Simulations" (2022). *Geochimica et Cosmochimica Acta* 316, 295–308.

Abstract

Determining how and when Mars formed has been a long-standing challenge for planetary scientists. The size and orbit of Mars are difficult to reproduce in classical simulations of planetary accretion, and this has inspired models of inner solar system evolution that are tuned to produce Mars-like planets. However, such models are not always coupled to geochemical constraints. Analyses of Martian meteorites using the extinct hafnium–tungsten (Hf–W) radioisotopic system, which is sensitive to the timing of core formation, have indicated that the Martian core formed within a few million years of the start of the solar system itself. This has been interpreted to suggest that, unlike Earth's protracted accretion, Mars grew to its modern size very rapidly. These arguments, however, generally rely on simplified growth histories for Mars. Here, we combine likely accretionary histories from a large number of *N*-body simulations with calculations of metal–silicate partitioning and Hf–W isotopic evolution during core formation to constrain the range of conditions that could have produced Mars.

We find that there is no strong correlation between the final masses or orbits of simulated Martian analogs and their ^{182}W anomalies, and that it is readily possible to produce Mars-like Hf–W isotopic compositions for a variety of accretionary conditions. The Hf–W signature of Mars is very sensitive to the oxygen fugacity (fO_2) of accreted material because the metal–silicate partitioning behavior of W is strongly dependent on redox conditions. The average fO_2 of Martian building blocks must fall in the range of 1.3–1.6 log units below the iron–wüstite buffer to produce a Martian mantle with the observed Hf/W ratio. Other geochemical properties (such as sulfur content) also influence Martian ^{182}W signatures, but the timing of accretion is a more important control. We find that while Mars must have accreted most of its mass within ~5 million years of solar system formation to reproduce the Hf–W isotopic constraints, it may

have continued growing afterwards for over 50 million years. There is a high probability of simultaneously matching the orbit, mass, and Hf–W signature of Mars even in cases of prolonged accretion if giant impactor cores were poorly equilibrated and merged directly with the proto-Martian core.

3.1 Introduction

The final stage of terrestrial planet formation began when large protoplanets finished consuming their neighboring small bodies and started perturbing each other's orbits (e.g., Chambers, 2004). This "chaotic growth" period was characterized by dynamical stochasticity: the mutual gravitation of numerous bodies introduces an unavoidable element of randomness into calculations of orbital dynamics, with even miniscule changes in starting conditions significantly altering the simulated solar system evolution (e.g., Lissauer, 2007). This stochasticity has made *N*-body accretionary simulations (which calculate the gravitational interactions between protoplanets) valuable tools in evaluating the range of possible growth histories for the terrestrial planets. For example, *N*-body simulations very frequently produce planets with Earth-like masses and orbits, so statistically meaningful interpretations can be drawn about Earth's likely accretionary history (e.g., Kenyon & Bromley, 2006; Canup, 2008; Rubie et al., 2015).

Producing Mars-like planets in *N*-body simulations, on the other hand, has proven more difficult. Early studies using classical dynamical regimes (i.e., with the Jovian planets near their modern orbits) produced planets near the orbit of Mars that were far too massive, creating the so-called "small Mars problem" (e.g., Wetherill, 1991; Chambers, 2001; Raymond et al., 2009). Later suites of simulations showed that it is

possible, though unlikely, to produce Mars with classical dynamics (Fischer & Ciesla, 2014), but many proposed solutions to the small Mars problem involve altering the dynamics of the protoplanetary disk. Such approaches include planetary growth by collisional fragmentation (Clement et al., 2019) or pileup of centimeter-sized bodies (Drążkowska et al., 2016). One of the most popular alternate dynamical narratives, the Grand Tack model, relies on an inward-then-outward migration of Jupiter to truncate the distribution of disk material at ~1.5 AU (Hansen et al., 2009; Walsh et al., 2011). This migration scatters material that originally condensed outside of 1.5 AU into the inner solar system and reduces the mass available in the Martian feeding zone. Grand Tack *N*-body simulations produce appropriately small Mars analogs (e.g., Walsh et al., 2011; Jacobson & Morbidelli, 2014; O'Brien et al., 2014), but the model has been criticized from a dynamical perspective: the mechanism, extent, and timing of the required giant planet migration are poorly constrained, and therefore must be tuned to reproduce the observed solar system configuration (e.g., Raymond & Morbidelli, 2014). *N*-body simulations run under these various accretion scenarios can provide important insights into the accretion history of Mars, such as plausible mass evolution histories and provenance, but Martian formation cannot be understood with dynamical simulations alone.

The accretion history of Mars can also be constrained using geochemical data. The extinct hafnium–tungsten (Hf–W) radioisotopic system, which is sensitive to the timing and conditions of core formation, is a common proxy for determining the formation timescales of terrestrial bodies (e.g., Lee & Halliday, 1995; Kleine et al., 2002; Jacobsen, 2005). This sensitivity comes from the differing chemical affinities of the parent and daughter nuclides: Hf is highly lithophile, but ^{182}Hf decays (with a ~9 Myr half-life) into ^{182}W, an isotope of moderately siderophile W. Much of a planet's

primordial W is sequestered in its core, but any ^{182}W produced from ^{182}Hf decay after the end of core–mantle equilibration (or produced earlier but not efficiently partitioned into the core) remains in the mantle, creating anomalous "extra" ^{182}W in the planet's rocks. Due to its short decay time, ^{182}Hf went extinct early in solar system history, fossilizing this signature of core formation.

The Martian Hf–W isotopic composition has been determined from the Shergottite-Nakhlite-Chassignite (SNC) meteorites, a small family of achondrites ejected from the Martian crust (Treiman et al., 2000). These meteorites have been widely used to interpret the timing of Martian core formation (e.g., Lee & Halliday, 1995; Righter & Shearer, 2003; Jacobsen, 2005; Dauphas & Pourmand, 2011; Krujier et al., 2017; Marchi et al., 2020), but this effort has several limitations. First, our knowledge of the Bulk Silicate Mars (BSM) composition, derived as it is from less than 70 kg of material, is poor. Studies of BSM (e.g., Morgan & Anders, 1979; Dreibus & Wänke, 1985; Lodders & Fegley, 1997; Bertka & Fei, 1998; Sanloup et al., 1999; Bouvier et al., 2009; Taylor, 2013; Yoshizaki & McDonough, 2020) tend to either not consider trace elements (like Hf and W) or to disagree on their abundances. Furthermore, the SNC meteorites appear to be derived from several distinct mantle sources that formed during the lifetime of ^{182}Hf (e.g., Foley et al., 2005); since Hf and W are not equally compatible upon mantle melting, the SNCs have inherited a range of Hf–W signatures. While it is doubtful that any meteorites are directly derived from BSM, the Shergottites imply an earlier (and thus less likely to have been overprinted) core formation age than the other SNCs, and evidence from the Sm–Nd system suggests that their Hf–W signature may be representative of BSM (Kleine et al., 2004; Dauphas & Pourmand, 2011; Krujier et al., 2017).

Using the modern Hf–W signature of Mars to date its formation is difficult because our understanding of both BSM and planetary accretion are incomplete (Nimmo & Kleine, 2007). Studies that assume the Martian mantle evolved undisturbed following a single core formation event (e.g., Jacobsen, 2005), or that Mars grew from perfectly equilibrated mass added in infinitesimally small steps (Harper & Jacobsen, 1996; Dauphas & Pourmand, 2011), have concluded that Mars accreted very early, within 5 Myr of solar system formation. These are not realistic depictions of planetary accretion and differentiation, however. During the chaotic end stages of accretion, growth may have occurred in random intervals from impactors with a variety of masses and compositions. Some studies have approached this issue with more sophisticated parameterizations of Martian formation (Marchi et al., 2020; Zhang et al., 2021) or have utilized *N*-body simulations that can match proposed formation timescales (Morishima et al., 2013; Woo et al., 2021). Morishima et al. (2013) calculated Hf–W evolution of three Mars-like bodies during *N*-body simulations of oligarchic growth and found that the Martian Hf–W signature can be matched even for very long (>100 Myr) accretion timescales, depending on conditions like the equilibration fraction of impactor material. Here, we examine a much larger number of Mars analogs produced by *N*-body models of chaotic growth under both classical and Grand Tack dynamics and trace their Hf–W isotopic evolution histories under a variety of accretionary conditions. This approach allows us to determine which narratives can match the observed geochemistry of Mars, thus providing more realistic constraints on the conditions of its formation.

3.2 Methods

We examined the outputs of 116 previously published *N*-body simulations: 16 in the Grand Tack (GT) regime (O'Brien et al., 2014) and 50 each in the classical Eccentric Jupiter and Saturn (EJS) and Circular Jupiter and Saturn (CJS) regimes (Fischer & Ciesla, 2014), though not all simulations form Mars analogs. The starting state of these simulations approximates the protoplanetary disk at the transition from oligarchic to chaotic accretion, with mass bimodally distributed between several dozen larger planetary embryos (each with mass of order 10^{-2} M_{Earth}) and a few thousand smaller planetesimals (each with mass of order 10^{-3}–10^{-4} M_{Earth}). We identified Martian analog bodies from the final solar system configuration of each simulation (see Section 3.3.1) and calculated the Hf–W isotopic evolution implied by the accretionary history of each analog. Bodies in each simulation were assigned an initial composition (Table B.1), oxygen fugacity (fO_2), and sulfur (S) content, and each starting body was differentiated into a core and mantle at the time of solar system formation (equated with CAI condensation at 4.567 Ga; MacPherson, 2014). To account for Hf–W evolution between the formation of the solar system and the start of chaotic growth, mantle Hf–W signatures of the differentiated analogs were evolved undisturbed for 2 Myr before the start of the *N*-body simulation (a timescale consistent with the oligarchic–chaotic transition of Kenyon & Bromely, 2006). The final ^{182}W anomalies of most Mars analogs are relatively insensitive to the details of this early accretionary phase (Figure B.1).

We tracked the isotopic evolution of every initial body that would eventually accrete into a Mars analog. Between impacts, mantle ^{182}Hf decayed to ^{182}W, increasing the ^{182}W anomaly, which is defined as:

$$\varepsilon_{182\mathrm{W}} = \left[\frac{\left({}^{182}\mathrm{W}/_{184}\mathrm{W}\right)_{mantle}}{\left({}^{182}\mathrm{W}/_{184}\mathrm{W}\right)_{CHUR}} - 1\right] \times 10{,}000 \quad (3.1)$$

where $\left({}^{182}\mathrm{W}/_{184}\mathrm{W}\right)$ is the molar ratio of radiogenic ^{182}W to the stable reference isotope ^{184}W, and CHUR is the chondritic uniform reservoir, assumed to have experienced no core formation and thus to represent a pristine bulk solar system value (Kleine et al., 2009). In general, a larger $\varepsilon_{182\mathrm{W}}$ implies more ^{182}Hf decay after core formation, and thus an earlier equilibration time (Jacobsen, 2005). A larger $\varepsilon_{182\mathrm{W}}$ may also indicate that more of the ^{182}W produced before and during core formation was left in the mantle due to a low degree of core–mantle equilibration (e.g., Morishima et al., 2013). The rate of $\varepsilon_{182\mathrm{W}}$ growth in a differentiated body depends on the overall Hf/W ratio of the mantle, quantified as:

$$f^{\mathrm{Hf/W}} = \frac{\left({}^{180}\mathrm{Hf}/_{184}\mathrm{W}\right)_{mantle}}{\left({}^{180}\mathrm{Hf}/_{184}\mathrm{W}\right)_{CHUR}} - 1 \quad (3.2)$$

where ^{180}Hf and ^{184}W are stable, non-radiogenic reference isotopes. A mantle with a higher $f^{\mathrm{Hf/W}}$ has relatively more Hf (including ^{182}Hf), and thus produces more ^{182}W per unit time until the system's extinction.

In our model, each impact was accompanied by an episode of metal–silicate equilibration between the entire impactor mantle, a fraction of the impactor core (k_{core}), and a fraction of the target mantle (k_{mantle}). Equilibration occurred at a fixed temperature (ΔT) above or below the chondritic mantle liquidus (Andrault et al., 2011) at a constant fraction (P_{frac}) of the core–mantle boundary (CMB) pressure at the time of the impact, which was scaled proportionally to the combined target+impactor mass

(assuming a final Martian CMB at 20 GPa; Rivoldini et al., 2011). In real planets, these values were likely correlated; for example, equilibration with $\Delta T < 0$ implies a partially crystallized mantle and thus a low equilibration pressure. However, we allow all parameters to vary independently over reasonable ranges (Table 3.1) to isolate the effects of each. The fO_2 was defined relative to the iron–wüstite (IW) buffer as:

$$\Delta\mathrm{IW} = 2 \times \log_{10}\left(\frac{a_{\mathrm{FeO}}^{silicate}}{a_{\mathrm{Fe}}^{metal}}\right) \approx 2 \times \log_{10}\left(\frac{X_{\mathrm{FeO}}^{silicate}}{X_{\mathrm{Fe}}^{metal}}\right) \quad (3.3)$$

where a_i^j is the activity of component i in phase j and X_i^j is the corresponding mole fraction. In most simulation suites, starting bodies were assigned a fixed initial fO_2 (Section 3.3) that was constant for all equilibration steps. In cases with non-homogenous initial fO_2 (Section 4.2), the fO_2 of each equilibration was a mass-weighted average of all bodies that had accreted to the target and impactor. The fO_2 of equilibration was used to calculate the corresponding Fe partition coefficient (D_{Fe}):

$$D_{\mathrm{Fe}} = \frac{X_{\mathrm{Fe}}^{metal}}{X_{\mathrm{FeO}}^{silicate}} = 10^{(-\Delta\mathrm{IW}/2)} \quad (3.4)$$

Note that this approach does not account for the possibility of other elements dissolving into the core and is therefore not self-consistent regarding the number of O and Si atoms present in each protoplanet, but this is a negligible effect due to the lithophile characters of those elements in Mars-sized bodies (e.g., Rubie et al., 2004; Steenstra & van Westrenen, 2018; Brennan et al., 2020). Ni was partitioned identically to Fe ($D_{\mathrm{Ni}} = D_{\mathrm{Fe}}$), S and C were approximated as perfectly siderophile, all other major elements (plus Hf) were assumed to be perfectly lithophile, and W partitioned between the core and mantle with its partition coefficient calculated as:

$$\log_{10} D_{\mathrm{W}} = a + \frac{b}{T} + \frac{c \times P}{T} + d \times \left(\frac{nbo}{t}\right) - \frac{n}{4}\Delta\mathrm{IW} - \log_{10}(\gamma_{\mathrm{W}}) \quad (3.5)$$

where a, b, c, and d are constants derived from metal–silicate partitioning experiments, n is the valence of W, P is the equilibration pressure, T is the equilibration temperature, $\frac{nbo}{t}$ is the number of non-bridging oxygen atoms per silicate tetrahedron (a proxy for the degree of silicate melt polymerization), and γ_W is the activity coefficient of W in the metallic phase, calculated after Ma (2001). The reported partitioning behavior of W varies between experimental studies (e.g., Cottrell et al., 2009; Seibert et al., 2011; Wade et al., 2013; Jennings et al., 2021), influencing the values of the constants in Equation 3.5 (Table B.2). In this study, we use the values of Jennings et al. (2021), as it compiles and reanalyzes the results of the earlier studies. We also use that study's chemical activity parameters and consider W–W, W–C, and W–S interactions.

After calculating the partitioning of Fe and W in a core formation episode, the compositions of the post-impact core and mantle were updated. For $k_{core} > 0$, the equilibrating material contains a portion of ^{182}W-depleted impactor core. This results in a post-impact mantle closer to the CHUR isotopic ratio, and thus a decrease in ε_{182W} proportional to k_{core} and the impactor mass. In contrast to ε_{182W}, the change of $f^{Hf/W}$ in each impact is small since the change in W partitioning is modest over the range of conditions in a Mars-mass planet (e.g., Cottrell et al., 2009; Jennings et al., 2021). After the final impact, all remaining ^{182}Hf in the mantle of the fully-grown Mars analog was converted to ^{182}W, allowing us to compare the implied modern Hf–W signature (i.e., the final ε_{182W} and $f^{Hf/W}$) of the analog to that of Mars itself.

Table 3.1. Model parameters and ranges tested.

parameter	complete range tested	constrained range
k_{core}	0–1	0.84–1
k_{mantle}	0–1	0.4–1
P_{frac}	0–1	0.4–0.6
ΔT	–200 K to 200 K	0 K
fO_2	IW–1.7 to IW–1.2	IW–1.6 to IW–1.3
bulk S	1–5 wt%	1.6–3.5 wt%

"Complete range tested" is the total range investigated for each parameter (the first three parameters must fall between 0 and 1 by definition). "Constrained range" is a more realistic subset of parameter space that we used to match the Hf–W signature of Mars within the restrictions of previous geochemical studies. See Section 3.4.1 for more details.

3.3 Results

3.3.1 Mars Analog Criteria

We define a Mars analog as a body that survives until the end of a simulation with a semi-major axis of 1–3 AU and mass of <0.2 M_{Earth} (Figure 3.1). With this definition, 33 of the 50 EJS simulations produce a Mars analog, along with 23 of 50 CJS and 13 of 16 GT simulations. This is a broader definition than is typical for analyses of *N*-body outputs (e.g., Fischer & Ciesla, 2014; Rubie et al., 2015; Zube et al., 2019), because we are interested in sampling the broadest range of possible accretionary histories. The lowest-mass survivors of each simulation are stranded embryos that accreted only a few planetesimals and therefore remained at approximately their initial masses: ~0.05 M_{Earth} in the EJS/CJS simulations (Fischer & Ciesla, 2014) and ~0.03 M_{Earth} in the GT simulations (O'Brien et al., 2014). These smallest analogs are 2–3× less massive than Mars, but larger than any non-planet in our solar system (for comparison, Ceres has a mass of ~0.0002 M_{Earth}). Planetary mass influences Hf–W isotopic evolution primarily because D_W changes with equilibration depth, but this effect is small over the size range of the analogs, making them viable candidates for investigating possible

timescales of accretion for Mars. We find that the properties of the Mars analogs (mass, orbital eccentricity, mass-weighted provenance, accretion time) are uncorrelated with their final semi-major axes in these simulations (Figure 3.2), implying that dynamical scattering is strong enough that any small planetary body could have ended up in a Mars-like orbit. Furthermore, bodies with Mars-like orbits do not necessarily resemble each other, or Mars, in terms of mass or Hf–W signature (Section 4.1).

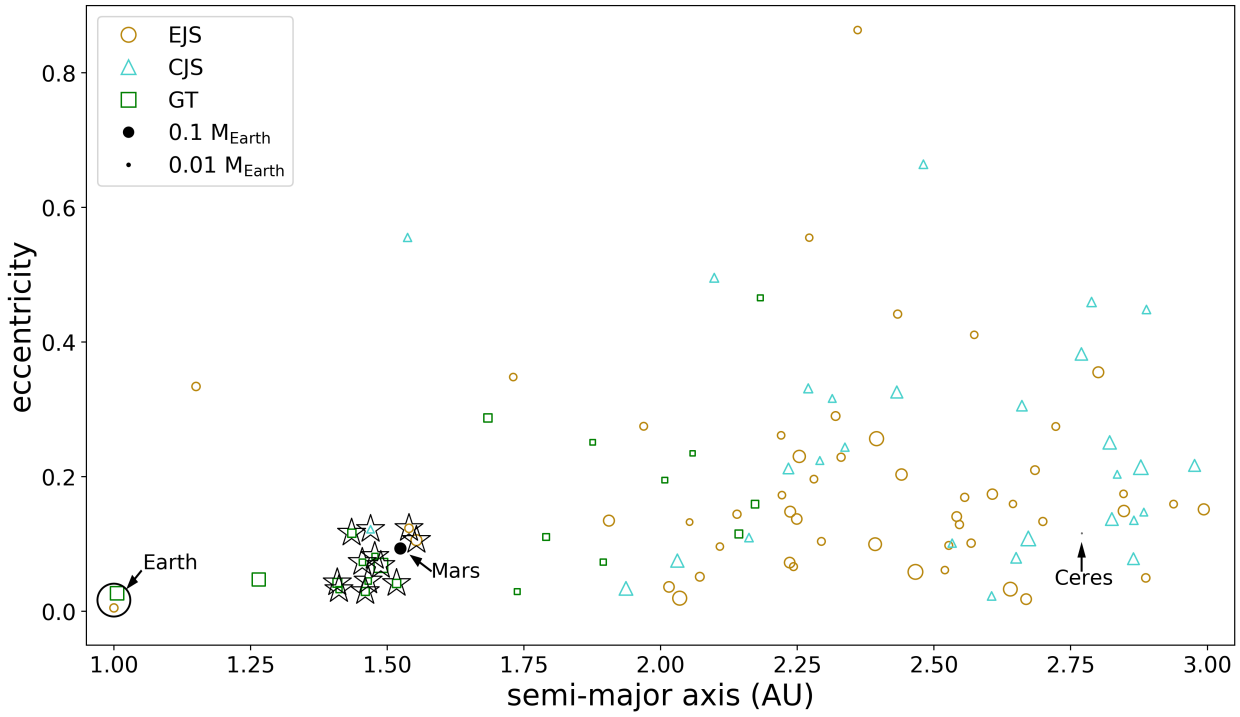

Figure 3.1: Orbital parameters of all Mars analogs (full descriptions in Table B.3). Symbol size is proportional to body mass. Actual solar system bodies shown for context (Ceres' mass is increased 10× for visibility). All analogs are included in the subsequent analysis; the twelve analogs with the most "Mars-like" orbits (indicated with stars) are examined in Section 4.1.

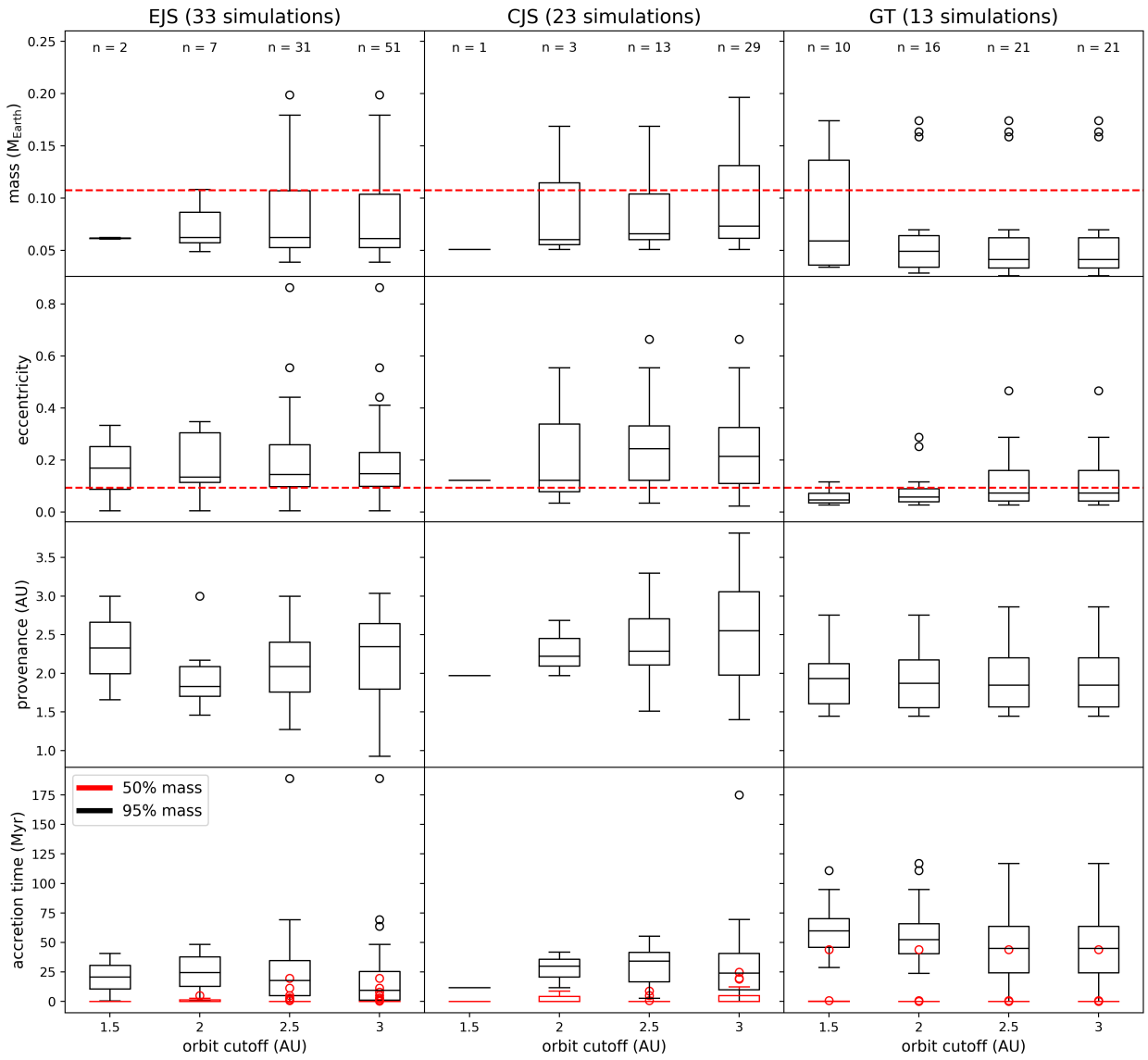

Figure 3.2: Distributions of orbital and accretionary parameters of Mars analogs from *N*-body simulations (Fischer & Ciesla, 2014; O'Brien et al., 2014). For each distribution, the box shows the interquartile range, the line within the box is the median, whiskers extend to ±1.5× the interquartile range, and any outlier analogs beyond that range are shown as open circles. "Orbit cutoff" indicates the maximum semi-major axis allowed for Mars analogs (i.e., an orbit cutoff of 2.5 includes all bodies with masses of <0.2 M_{Earth} and semi-major axes of 1–2.5 AU as Mars analogs). Numbers in the top panels indicate the number of analogs found using each orbit cutoff. Dashed red horizontal lines indicate observed Martian values. "Provenance" is the mass-weighted semi-major axis of an analog's building blocks. Note that most analogs start the simulation at >50% of their final mass and that no parameters appear to vary significantly with the orbit cutoff used for any of these accretion scenarios.

3.3.2 Analysis of Simulation Suites

Evolution of mass and ε_{182W} for all Mars analogs are shown in Figure 3.3. Prolonged accretion is common in all the simulations; few analogs match the Chambers (2006) homogenous, exponential growth function as parameterized by Dauphas & Pourmand (2011). As those studies pointed out, a planet with a Mars-like $f^{Hf/W}$ must accrete rapidly to match the ε_{182W} of Mars since late equilibration of impactor cores will reduce ε_{182W}. Marchi et al. (2020) found that accretion timescales of up to 15 Myr can be consistent with Mars under certain conditions, but many Mars analogs in these *N*-body simulations form even more slowly. Most analogs start the simulation at >50% of their final mass, but accretion within the simulation dominates the final Hf–W signature of most analogs (Figure B.1). This is consistent with the results of Morishima et al. (2013), which found that the contribution of the oligarchic growth period to the final ε_{182W} of Mars was small if accretion continued afterwards. Regardless, Mars analogs in these *N*-body simulations tend to accrete most of their mass within the brief formation timescales deduced by earlier studies (e.g., 3.3 Myr: Jacobsen, 2005; 1.8 Myr: Dauphas & Pourmand, 2011; 2.4 Myr: Kleine & Walker, 2017; 4.1 Myr: Kruijer et al., 2017), even if they do not reach their final masses until much later. Mars analogs with the longest 50% accretion timescales also tend to be those with the lowest final ε_{182W}.

As expected, GT simulations, in which Jupiter's migration scatters protoplanetary mass towards the Sun, tend to produce many Mars analogs (~1.3 per simulation), and those tend to have more Mars-like orbits than analogs formed in EJS or CJS simulations (Figure 3.1). GT analogs also take longer to reach their final mass (median 95% accretion times: 9.6 Myr for EJS, 24 Myr for CJS, 45 Myr for GT). EJS and CJS simulations both produce many analogs that orbit further from the sun and with

greater eccentricities than Mars, though EJS produces analogs almost twice as often (~1 per simulation versus ~0.6 for CJS), implying that mass ends up either lost or concentrated in a few large bodies under CJS dynamics. CJS is also the only suite to show even a slight possible trend between a body's final semi-major axis and the provenance of its material (Figure 3.2), consistent with the lower degree of radial mixing in classical dynamical regimes (e.g., Fischer et al., 2018).

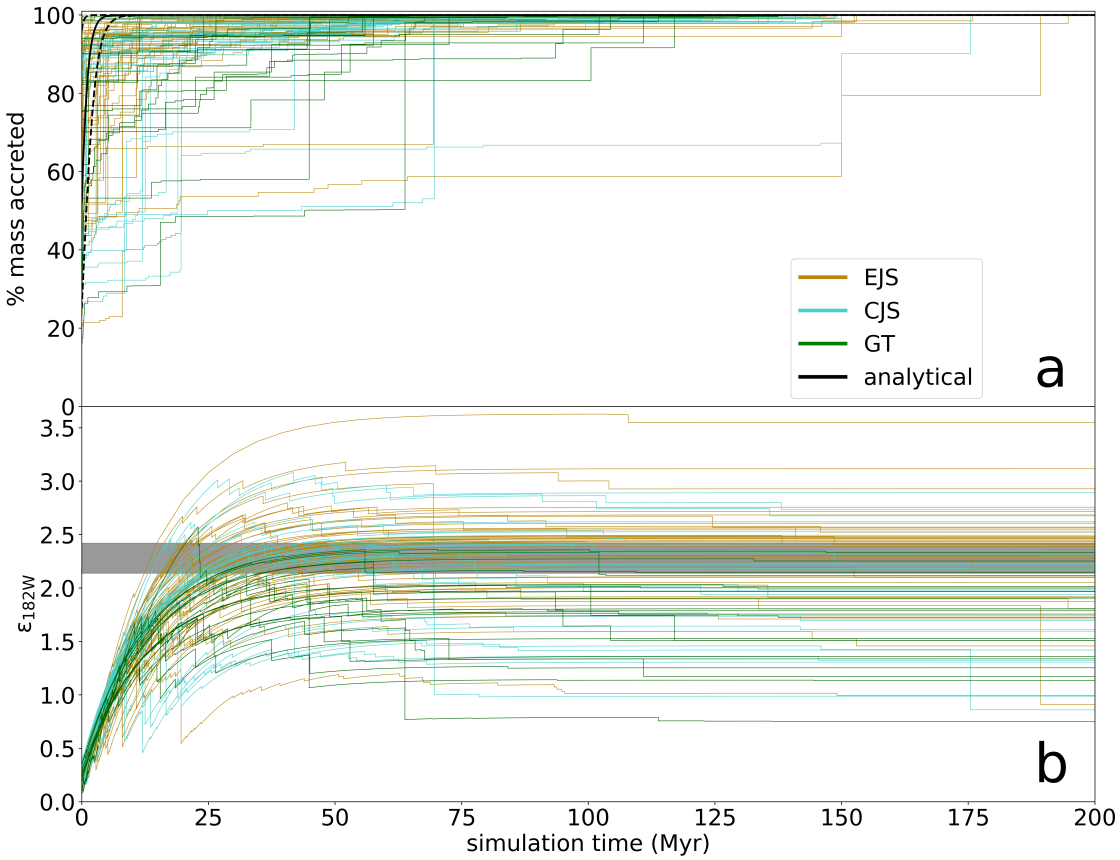

Figure 3.3: Evolution of mass (**a**) and ε_{182W} (**b**, relative to CHUR) of all Mars analogs. Simulations begin 2 Myr after CAI formation. Analytical growth curve (solid black curve) and 95% confidence intervals (dashed black curves) are from Dauphas & Pourmand (2011). ^{182}W anomalies depend on various accretionary parameters; these ε_{182W} evolution curves were calculated at "reference case" conditions (P_{frac} = 0.6, k_{core} = 0.85, k_{mantle} = 0.4, S = 3.5 wt%, ΔT = 0 K, fO_2 = IW–1.47; see Section 3.3). The shaded bar indicates the observed ε_{182W} of Mars (Table B.4). Each impact is associated with a drop in ε_{182W} proportional to k_{core} and the target-to-impactor mass ratio.

3.3.3 Parameters Influencing Hf–W Evolution

One way to visualize the influence of various model parameters on the resulting Hf–W signatures is to define a reference set of parameters, then isolate the effect of each parameter by varying them one at a time (Figure 3.4). An analog's oxidation state is the single most important factor in determining its Hf–W signature. The fO_2 of equilibration determines the fraction of W that is sequestered in the core, thus setting the mantle $f^{Hf/W}$ and the rate of ε_{182W} increase. Since W is high valence (+4 or +6), its partitioning is particularly redox-sensitive (e.g., Cottrell et al., 2009) and the mantle of a reduced planet contains much less of the total W than that of a more oxidized planet, resulting in a larger $f^{Hf/W}$ and ultimately a larger final ε_{182W}. The same effect (though smaller in magnitude) can be seen by increasing ΔT, increasing P_{frac}, or increasing bulk S content. These parameters increase both $f^{Hf/W}$ and ε_{182W} approximately equally, but the degree of impactor core equilibration has a different effect: a lower value for k_{core} results in a lower $f^{Hf/W}$ but a larger ε_{182W}. This is due to the action of two competing effects. A low degree of accreted metal re-equilibration causes the final body to inherit more of the signature of its building blocks, and W is less siderophile at shallower depths in the Jennings et al. (2021) parameterization, decreasing $f^{Hf/W}$. Simultaneously, a small k_{core} reduces the drawdown of radiogenic ^{182}W in each impact, allowing ε_{182W} to reach higher values. The effect is qualitatively similar for k_{mantle} but, as is the case for the Earth (Fischer and Nimmo, 2018), is only significant at very low degrees of mantle equilibration; in Figure 3.4, the "reference case" point ($k_{mantle} = 0.4$) is nearly indistinguishable from the maximum mantle equilibration point ($k_{mantle} = 1$). We also considered the possibility that k_{core} may have been lower in giant (embryo–embryo) impacts since hydrodynamic experiments have indicated that direct core merging is likely in these cases (Deguen et al., 2014). Decreasing k_{core} for giant impacts removes

their otherwise irreversibly-large ε_{182W} reductions (i.e., the large vertical drops in Figure 3.3b), allowing some analogs that experienced embryo–embryo impacts to reach Martian ε_{182W} values. An example of this effect can be seen in Figure 3.5d.

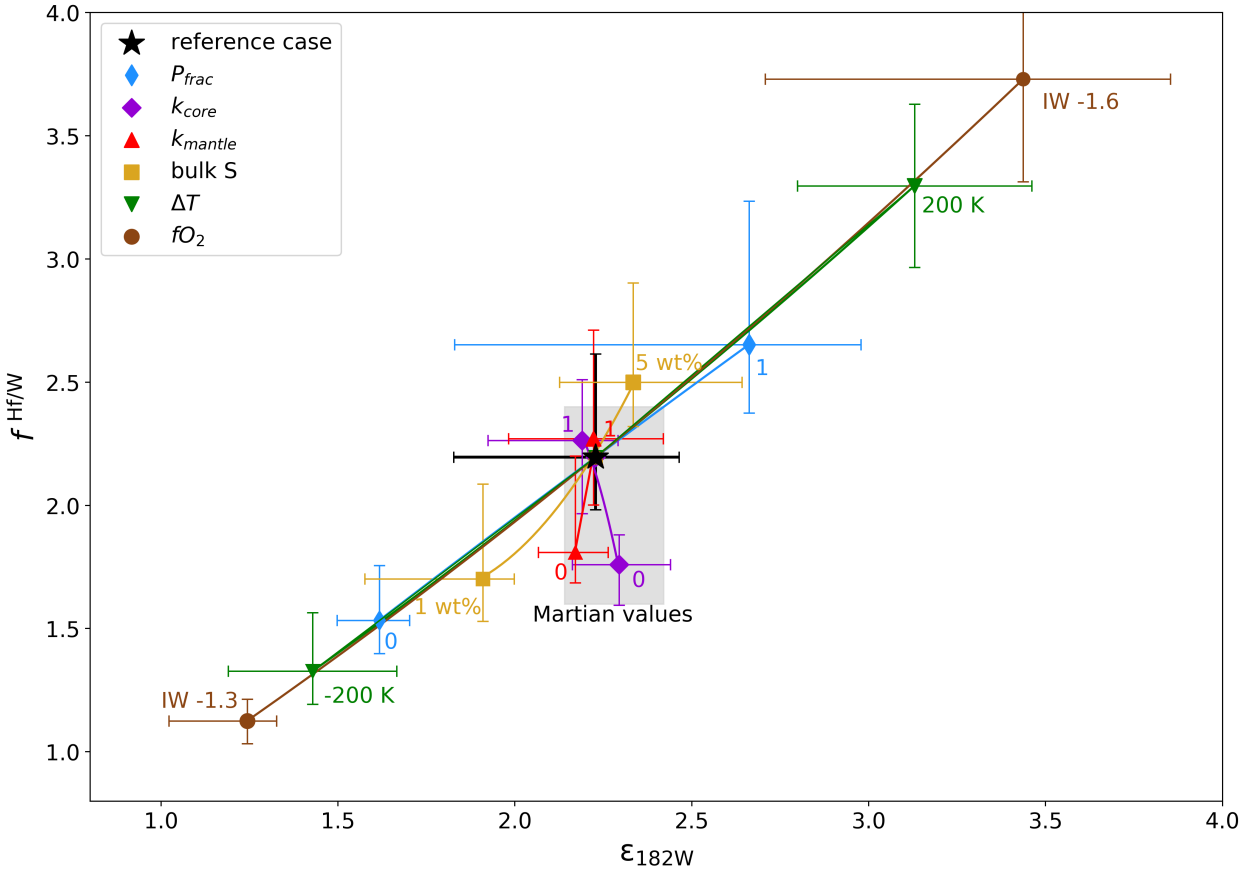

Figure 3.4: Sensitivity of the Hf–W isotopic signature of Mars to variation in model parameters (Table 3.1). The shaded grey region indicates the uncertainty range of measured Martian Shergotty-source values (Table B.4). The "reference case" model parameters are P_{frac} = 0.6, k_{core} = 0.85, k_{mantle} = 0.4, S = 3.5 wt%, ΔT = 0 K, and fO_2 = IW–1.47, representing a close match between the median of the analogs and Mars (Section 3.4.1). Other points were calculated with these same values except for the single parameter being varied that was changed to the value indicated next to each point. Symbols denote the median of all analogs and error bars indicate interquartile ranges. Trends between symbols were calculated by a degree 2 polynomial fit to 4 points evenly spanning each parameter range (not shown). Figure B.2 is an alternate version of this figure using the Siebert et al. (2011) W metal–silicate partitioning parameterization.

The presence of C can significantly alter W partitioning (e.g., Jennings et al., 2021), but the C content of the Martian core is thought to be very low due to the absence of isotopic fractionation signatures (Wood et al., 2013) and the decrease of C solubility in S-rich alloys (Tsuno et al., 2018). Studies with the most C-rich Martian cores (e.g., Steenstra & van Westrenen, 2018) tend to propose abundances of ~1 wt% (i.e., 0.2 wt% bulk planetary C). We performed one set of calculations with C at this level and found that its presence increased $f^{Hf/W}$ by 0.05 and ε_{182W} by 0.02, a very small effect.

3.4 Discussion

3.4.1 Reproducing Mars

Considering the similar effects of several model parameters (Figure 3.4) and the wide distribution of analog properties, it is easily possible to get a few analogs to match the Martian Hf–W signature for many parameter combinations. However, there is a relatively restricted subset of parameter space that is both geophysically and geochemically plausible and results in a significant fraction of analogs matching the observed signature of Mars. As noted above, analog ε_{182W} is most sensitive to initial fO_2. There is a limited range (approximately IW–1.3 to IW–1.6) in which any analogs match Mars, regardless of other parameter values; even modestly more reducing conditions result in a wide distribution of analog properties that extends to high $f^{Hf/W}$ and ε_{182W}, overshooting Mars. Fortunately, the average fO_2 of core formation on Mars is constrained by its mantle FeO content (i.e., Equation 3.3), and previous studies have shown that the FeO-derived fO_2 of Mars agrees with the permissible range found here (e.g., Righter & Drake, 1996; Rai & van Westrenen, 2013; Rubie et al., 2015; Brennan et al., 2020). Brennan et al. (2020) also used mantle trace elements to constrain the values

of P_{frac} (0.4–0.6), k_{core} (0.84–1.0), and k_{mantle} (0.4–1.0). These conditions (high degree of equilibration, intermediate equilibration depth) broadly agree with other investigations of Martian core formation (Kleine et al., 2004; Righter & Chabot, 2011; Yang et al., 2015; Zube et al., 2019), so we restrict our further exploration of parameter space to these ranges. Note that the large k_{core} value interpreted for Mars can equivalently imply efficient mixing of differentiated impactors and/or accretion of undifferentiated impactors (which necessarily have $k_{core} = 1$), and these two cases are indistinguishable in terms of their effect on Hf–W.

The bulk inventory of volatile elements (especially S) in Mars is controversial, with some studies (e.g., Wang & Becker, 2017; Yoshizaki & McDonough, 2020) favoring much lower abundances than others (e.g., Sanloup et al., 1999; Khan & Connolly, 2008; Taylor, 2013; Steenstra & van Westrenen, 2018). Furthermore, S content cannot be constrained by the Hf–W signature because the effect of changing S is indistinguishable from that of other parameters (Figure 3.4). We use a maximum bulk S value of 3.5 wt% (35% less S than CI chondrites; Palme & O'Neill, 2014). This corresponds to ~18 wt% S in the Martian core, within the preferred range of most S-rich models and close to the value interpreted from the first seismic measurements of the Martian core (Stähler et al., 2021). While Martian differentiation could have been unusually hot due to ^{26}Al heating (Sahijpal & Bhatia, 2015), temperatures during planetary formation are not well constrained and would vary depending on the time and size of each analog's impacts, so we do not impose a ΔT.

With these restrictions, we define our "reference case" as a set of parameters that produces a close match between the median analog Hf–W signature and Martian values (Figure 3.5a): $P_{frac} = 0.6$, $k_{core} = 0.85$, $k_{mantle} = 0.4$, S = 3.5 wt%, $\Delta T = 0$ K, and initial

fO_2 = IW–1.47. With these values, 20% of EJS analogs, 31% of CJS analogs, and 14% of GT analogs fall within uncertainty of the Martian Shergottite source. If we instead reduce the S content to produce a core with ~8 wt% S (i.e., 1.6 wt% bulk S, which is 70% less than CI chondrites), the best match to Mars is obtained with slightly more reducing conditions (IW–1.50; Figure 3.5b). A tighter clustering around Martian $f^{Hf/W}$ is achieved at intermediate S abundance (2.7 wt%; Figure 3.5c). If most analogs have approximately Martian $f^{Hf/W}$, matching ε_{182W} depends almost entirely on accretionary history. Keeping the previous parameters but allowing cores to merge directly (k_{core} = 0) during giant embryo–embryo impacts (Figure 3.5d) creates more matching analogs than in our reference case (31% EJS, 28% CJS, 9.5% GT), and some of these matches experience giant impacts tens of Myr into solar system evolution (Figure 3.6d).

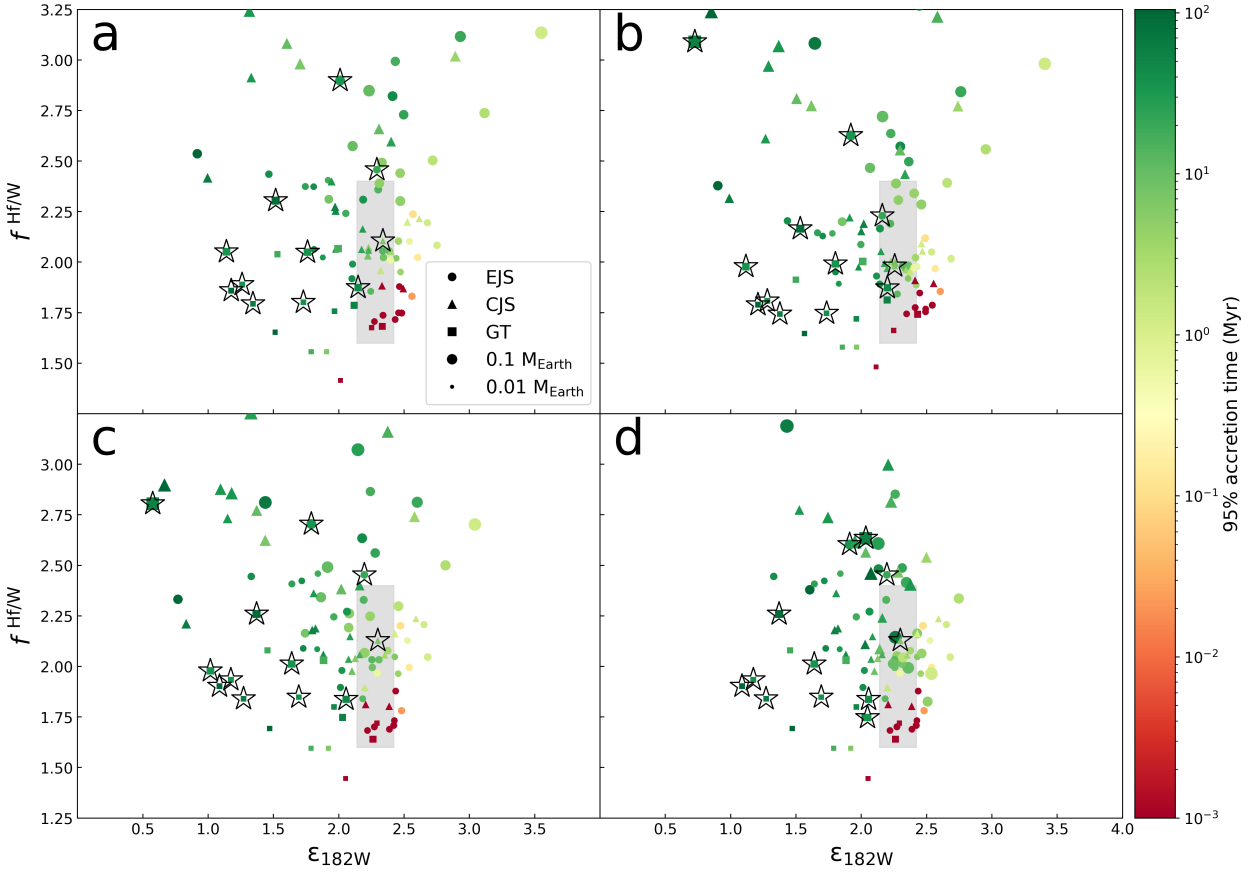

Figure 3.5: Hf–W signatures of Mars analogs for various model parameters and formation timescales. Analogs with the most Mars-like orbits are indicated with stars (Figure 3.1). Symbol color indicates 95% accretion times and symbol size is proportional to mass. The shaded grey region indicates the uncertainty range of measured Martian Shergotty-source values (Table B.4). **a.** Reference case: fO_2 = IW–1.47, 3.5 wt% S, k_{mantle} = 0.4, k_{core} = 0.85, P_{frac} = 0.6. **b.** A low-S case: fO_2 = IW–1.50, 1.6 wt% S, k_{mantle} = 0.4, k_{core} = 0.85, P_{frac} = 0.6. **c.** A good match to $f^{Hf/W}$ only: fO_2 = IW–1.5, 2.7 wt% S, k_{mantle} = 0.4, k_{core} = 1.0, P_{frac} = 0.4. **d.** Same as **c** but with k_{core} = 0 (direct core merging) for embryo–embryo impacts. Examples of other possible parameter combinations are shown in Figure B.3.

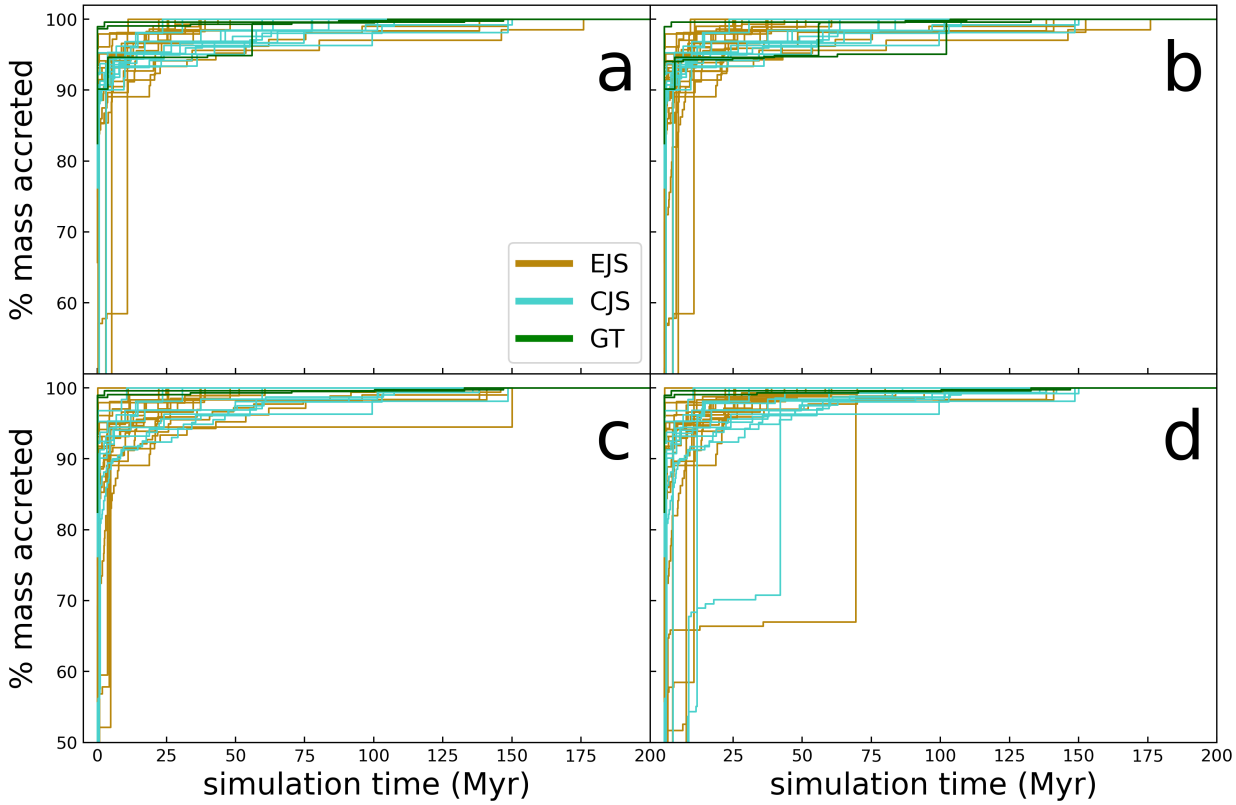

Figure 3.6: Growth curves for the analogs that match Martian Hf–W in each corresponding panel of Figure 3.5. Most matching analogs continue accreting for substantially longer than the 5 Myr timescale often attributed to Mars (Section 3.1), especially if giant impactor cores are poorly equilibrated (**d**).

Regardless of the precise parameter combination, we can draw some general conclusions about the types of analogs that best match Mars. First, the Hf–W signature can be matched by any of the dynamical suites. The $f^{\mathrm{Hf/W}}$ of the Martian mantle is quite low; for comparison, Earth's value has been estimated as 12 (Jacobsen, 2005), 14 (Kleine et al., 2009), or 25 (Dauphas et al., 2014). Given this low $f^{\mathrm{Hf/W}}$, Mars analogs that end up matching $\varepsilon_{182\mathrm{W}}$ tend to be those that avoid having their $\varepsilon_{182\mathrm{W}}$ values reset by significant accretion after ~2 ^{182}W half-lives have elapsed (i.e., >20 Myr post-CAI). This constraint is, however, not as severe as implied by the parametrized accretion curve of Dauphas & Pourmand (2011). Our reference case, for example, includes a GT analog

with a 95% accretion time of 63 Myr that has a Mars-like orbit and matches the $f^{Hf/W}$ and ε_{182W} of Mars within uncertainty. If the cores of giant impactors equilibrate with the same k_{core} as planetesimal impactors, then Mars is unlikely to have experienced an embryo-embryo collision, especially after 20 Myr post-CAI. However, if giant impactor cores are poorly equilibrated, then even large Mars analogs that experienced giant impacts can match the Hf–W signature of Mars for prolonged (e.g., Marchi et al., 2020) accretionary histories (in Figure 3.5d, 30% of the matching analogs are ≥0.75 M_{Mars}). Finally, analogs with the most Mars-like orbits (Figure 3.1) do not necessarily have Mars-like Hf–W signatures, nor do they cluster together in ε_{182W}–$f^{Hf/W}$ space (Figure 3.5). Despite this, a few analogs with Mars-like orbits (which ones in particular depend on model parameters) often match Martian Hf–W values, demonstrating that analogs can simultaneously match the orbit and the core formation signature of Mars in our model. Indeed, any analog can be made to match the Martian Hf–W signature if the accretionary parameters (especially fO_2) are tuned appropriately.

It is important to note that the impacts modelled here are not part of a late veneer. Any impactor that mixes into the mantle without participating in core formation (whether because it is fully oxidized or arrives after core formation is complete) will add isotopes in chondritic ratios and therefore reduce $f^{Hf/W}$ and ε_{182W} proportionally to the impactor-to-mantle ratio (since the chondritic values are 0 for each parameter). The mass of the late veneer on Mars was constrained by Dale et al. (2012), which showed that Martian highly-siderophile element (HSE) abundances are approximately 2.5 orders of magnitude lower than those of CI chondrites. Assuming no HSEs remained in the mantle after core formation, the late veneer cannot account for more than 0.3% the mass of the mantle, or ~1.5×10^{21} kg for a Mars-sized analog. This is four times smaller than the planetesimals in our N-body simulations, which

implies that the ε_{182W} reduction from the late veneer would have been minimal, about 3 $\times 10^{-3}$ ε units. If Mars did, in fact, accrete mass for tens of Myr, all those impactors participated in core formation, implying that the Martian magma ocean was either long-lived (e.g., Debaille et al., 2007) or was regenerated by each impact.

3.4.2 Disk Conditions

In the preceding analysis, we imposed a uniform Mars-like fO_2 and bulk S content on all the initial bodies in each *N*-body simulation. Under these conditions, since the distribution of accretion times does not vary with orbit (Figure 3.2, bottom row), final ε_{182W} values and orbits are similarly uncorrelated (Figure B.3). This does not reflect the reality of the protoplanetary disk. At the start of chaotic accretion, there would have been a relationship between a body's composition and the nebular properties of its indigenous orbit. As evidenced by Earth's relatively low core formation fO_2 (<IW–2.0; Geßmann & Rubie, 2000; Li & Agee, 2001; Chabot et al., 2005) and bulk S content (<1 wt%; McDonough, 2003) compared to Mars, higher nebular temperatures close to the Sun probably inhibited the condensation of more volatile species. Previous analyses of *N*-body simulations have examined this effect by imposing variable fO_2 on their initial bodies, such as a highly reduced "enstatite chondrite like" inner solar system surrounded by a more oxidized "ordinary chondrite like" region (e.g., Rubie et al., 2015). There may be evidence for such discrete reservoirs of material existing in the early solar system (e.g., Warren, 2011; Morbidelli et al., 2016; Lichtenberg et al., 2021), but their spatial and temporal boundaries, as well as their bulk chemistries, are poorly constrained.

Matching the narrow range of permissible Martian bulk fO_2 requires the oxidation state of these reservoirs (and the location of the boundary between them) to

be precisely tuned to a particular accretionary provenance. As Rubie et al. (2015) concluded based on Martian FeO content, it is difficult to produce Mars by mixing reasonable inner solar system and outer solar system reservoirs (Figure 3.7). Since Hf–W is so sensitive to fO_2, the only "successful" fO_2 distribution (i.e., one that allows numerous analogs to match Mars) is one in which a large portion of primordial material closely matches the final fO_2 of Mars. In any other case, very few analogs accrete exactly the right proportions of reduced and oxidized material. This could be taken as an indication that the bulk fO_2 of Mars represents a single, local reservoir (e.g., Mah & Brasser, 2021) rather than a mixture, but such a simple primordial fO_2 distribution is probably unrealistic (e.g., Ciesla & Cuzzi, 2006). The situation becomes even more complicated if the bulk S gradient does not coincide with variations in fO_2 or if disk dynamics displace material far from its region of condensation by the time of chaotic growth (e.g., Williams et al., 2020). Therefore, we have chosen to impose a Mars-like composition and redox state on all Mars analogs, allowing us to focus on how their accretionary history influences their Hf–W evolution. It is worth noting that most analogs (including those with Mars-like orbits) have provenances of ≥2 AU (Figure 3.2), so it is possible to match Martian geochemistry and simultaneously form a reduced Earth from material originating closer to the Sun.

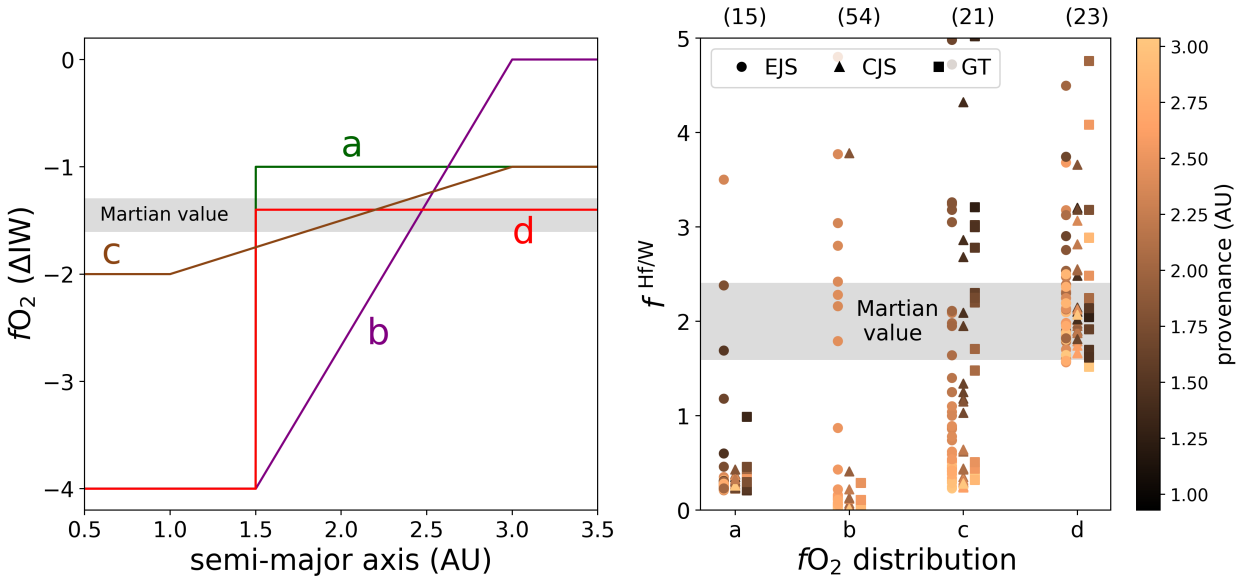

Figure 3.7: Hypothetical disk fO_2 distributions (**left**) and resulting analog $f^{Hf/W}$ values (**right**). The shaded bar in the left panel shows the fO_2 constraints from Hf–W (Section 3.4.1) and the shaded bar in the right panel shows the Martian $f^{Hf/W}$ value (Kleine & Walker, 2017; Table B.4). The counts of analogs whose $f^{Hf/W}$ plot off-scale are shown in parentheses at the top of the figure. Unless fO_2 distributions are contrived such that much of the disk has approximately Martian fO_2 (i.e., distribution d), almost all analogs end up either too oxidized (very low $f^{Hf/W}$) or too reduced (very high $f^{Hf/W}$). Provenance is quantified as the mass-weighted semi-major axis of an analog's building blocks and indicated by the color of each symbol.

3.4.3 Other *N*-body Approaches

While it is impossible to perfectly simulate the complex physics of planetary accretion, there have been significant advances in *N*-body techniques since the creation of our simulation suites. For example, Woo et al. (2021) used improved computational power to run an *N*-body model with more and smaller initial bodies, thus allowing the simulation's start time to closely coincide with that of the solar system. In agreement with our results, that study found that most Mars analogs accrete more slowly than the exponential growth curve of Dauphas & Pourmand (2011) and proposed various dynamical methods to make them grow more quickly. These include the

implementation of non-perfect merging between colliding protoplanets, an effect which slightly prolongs Earth's accretion (e.g., Chambers, 2013; Dwyer et al., 2015) but could potentially form Mars more quickly via fragmentation (Kobayashi & Dauphas, 2013; Dugaro et al., 2019).

Studies disagree on whether "pebble accretion" promotes (Levison et al., 2015; Matsumura et al., 2017) or discourages (Voelkel et al., 2021) the formation of small terrestrial planets, but a pebble contribution speeding up pre-chaotic growth (Lichtenberg et al., 2021) could possibly have helped Mars form within the timeframe of Dauphas & Pourmand (2011). Additionally, since very small bodies will fully equilibrate in the magma ocean (i.e., have $k_{core} = 1$; Section 4.1), significant pebble accretion could help explain Mars' high k_{core} value.

Broadly, our approach could be extended to any number of *N*-body simulation types, including ones with different disk dynamics, pre-simulation periods, or impact outcomes, but it seems likely that the Hf–W signature of Mars can be reproduced in a variety of circumstances despite prolonged accretion. As noted above, however, later impactors have larger negative effects on ε_{182W} because of the ongoing decay of ^{182}W, with anomaly growth dramatically slowing after 20 Myr post-CAI. Simulations in which long-lived nebular gas postpones the start of chaotic accretion (e.g., Walsh & Levison, 2019; Clement et al., 2020) are likely to produce systematically low ε_{182W} if there is late addition of material to Mars (Figure B.3d). A possible workaround could be if late-accreting material avoids resetting the mantle anomaly because it does not sequester radiogenic ^{182}W to the core ($k_{core} = 0$). Simulations with long-lived nebulae have yet to successfully solve the small-Mars problem, but Hf–W evolution under this regime could be a target of future studies.

3.5 Conclusions

The Martian Hf–W signature ($f^{Hf/W}$ and ε_{182W}) can be reproduced by modeling W partitioning for successive stages of core formation in *N*-body accretion simulations. As suggested by some recent studies (e.g., Marchi et al., 2020; Woo et al., 2021; Zhang et al., 2021), we find that many Mars analogs experience substantially protracted accretion, in contrast to the rapid exponential growth of Dauphas & Pourmand (2011). While proto-Mars likely reached 50% of its final size within 5 Myr of solar system formation, it may not have finished growing until >50 Myr later. Exactly which accretionary histories match Mars is dependent on model parameters. Hf–W evolution is particularly sensitive to the oxidation state of metal–silicate equilibration, constraining initial fO_2 to a narrow range (IW–1.6 to IW–1.3) consistent with the FeO content of the Martian mantle. This sensitivity means that reproducing Mars by substantial accretion of material from two reservoirs of dramatically differing fO_2 is a low-probability event. As in previous studies (e.g., Kleine et al., 2004; Righter & Chabot, 2011; Yang et al., 2015; Zube et al., 2019; Brennan et al., 2020), we find that Martian material could have been highly equilibrated, with the caveat that larger, later-accreting analogs best match the Hf–W signature of Mars if giant impactor cores directly merged with that of proto-Mars (e.g., Deguen et al., 2014).

While GT dynamics allow analogs to form with Mars-like orbits much more often than EJS or CJS scenarios, we do not find that a Mars-like orbit correlates with Mars-like chemistry, or that GT analogs have a higher probability of matching the Hf–W signature of Mars. Indeed, analogs formed by GT dynamics tend to accrete material from a narrower range of orbits and finish forming later, slightly reducing their ranges of acceptable model parameters. Nonetheless, there are reasonable parameter

combinations by which any of the dynamical regimes investigated can match both the orbit and Hf–W signature of Mars simultaneously, even with substantially prolonged accretion.

Acknowledgements

The authors thank the *Geochimica et Cosmochimica Acta* editor Audrey Bouvier for handling this manuscript, as well as D. C. Rubie and two anonymous reviewers for their helpful suggestions. This work was supported in part by a National Science Foundation Graduate Research Fellowship awarded to M.C. Brennan (DGE1745303), a NASA Emerging Worlds grant awarded jointly to R.A. Fischer and F. Nimmo (NNX17AE27G), and the Henry Luce Foundation.

Chapter 4
Deformation Properties of Earth's Inner Core

Matthew C. Brennan[1], Rebecca A. Fischer[1], Samantha Couper[2], Lowell Miyagi[2], Daniele Antonangeli[3], Guillaume Morard[3,4]

[1]Department of Earth and Planetary Sciences, Harvard University

[2]Department of Geology and Geophysics, University of Utah

[3]Sorbonne Université

[4]Université Grenoble Alpes

The contents of this chapter are based on: "High-Pressure Deformation of Iron–Nickel–Silicon Alloys and Implications for Earth's Inner Core" (2021). *Journal of Geophysical Research: Solid Earth* 126, e2020JB021077.

Abstract

Earth's inner core exhibits strong seismic anisotropy, often attributed to the alignment of hexagonal close-packed iron (hcp-Fe) alloy crystallites with the Earth's poles. How this alignment developed depends on material properties of the alloy and is important to our understanding of the core's crystallization history and active geodynamical forcing. Previous studies suggested that hcp-Fe is weak under deep Earth conditions but did not investigate the effects of the lighter elements known to be part of the inner core alloy. Here, we present results from radial X-ray diffraction experiments in a diamond anvil cell that constrain the strength and deformation properties of iron–nickel–silicon (Fe–Ni–Si) alloys up to 60 GPa. We also show the results of laser heating to 1650 K to evaluate the effect of temperature. Observed alloy textures suggest different relative activities of the various hcp deformation mechanisms compared to pure Fe, but these textures could still account for the theorized polar alignment of the inner core crystallites. Fe–Ni–Si alloys are mechanically stronger than Fe and Fe–Ni; extrapolated to inner core conditions, Si-bearing alloys may be more than an order of magnitude stronger. This enhanced strength proportionally reduces the effectivity of dislocation creep as a deformation mechanism, which may suggest that core texture developed during crystallization rather than as the result of post-solidification plastic flow.

4.1 Introduction

Since the discovery of the inner core (Lehmann, 1936) and its identification as a solid iron alloy (Birch, 1952), seismic studies have revealed it to be complexly structured and seismically anisotropic. On average, seismic waves move through the

inner core several percent faster on paths parallel to Earth's axis of rotation compared to perpendicular paths (e.g., Deuss, 2014). This anisotropy is well documented by travel time (e.g., Creager, 1992) and normal mode (e.g., Durek & Romanowicz, 1999) observations, and deviations from this large-scale anisotropy have been used to suggest other inner core structural features (e.g., Irving & Deuss, 2011; Ishii & Dziewonski, 2002; Ouzounis & Creager, 2001; Su & Dziewonski, 1995). These secondary structures are frequently invoked as evidence for various proposed mechanisms of the primary anisotropy's development.

As with many instances of seismic anisotropy, the Earth's inner core structure likely arises from preferred orientation of crystallites (i.e., texture). Solid Fe-rich alloys (including those in the Fe–Ni–Si system) are expected to exist in the hexagonal close-packed (hcp) crystal structure (ε-Fe) at inner core pressures (P) and temperatures (T) (e.g., Sakai et al., 2011; Tateno et al., 2010, 2012, 2015). Since hcp crystals are seismically fast parallel to their c-axes (Bergman et al., 2000), a preferential alignment of the inner core's crystals with Earth's axis of rotation is widely accepted as responsible for the inner core anisotropy (e.g., Antonangeli et al., 2006; Sakai et al., 2011; Sayers, 1989; Stixrude & Cohen, 1995; Vočadlo et al., 2009). This explanation is experimentally supported by observations of strong c-axis aligned deformation textures in hcp metals, including ε-Fe (e.g., Antonangeli et al., 2006; Merkel et al., 2012, 2013; Miyagi et al., 2008; Wenk et al., 2000). It is worth noting that cubic Fe polymorphs cannot deform to produce a texture compatible with the observed anisotropy (Lincot et al., 2016).

There is considerable diversity amongst the mechanisms proposed to create this texture. One class of models relies on preferred orientation developing during crystallization (e.g., Karato, 1993; Bergman, 1997). However, if crystals instead solidify

in random orientations, texture must develop by plastic flow in the solid aggregate. This can result from solid-state convection (e.g., Buffett, 2009; Deguen et al., 2013; Jeanloz & Wenk, 1988) or from west-to-east translation due to preferential solidification in one hemisphere (e.g., Alboussiere et al., 2010; Bergman et al., 2010; Monnereau et al., 2010). Flow may also be driven by forces external to the inner core, such as electromagnetism (e.g., Buffet & Wenk, 2001; Takehiro, 2011) or outer core convection (e.g., Aubert et al., 2008; Yoshida et al., 1996). Experimentally, Gleason & Mao (2013) found that Fe is very weak at ultra-high pressures. If this holds true for the inner core, post-solidification texturing could be driven by almost any source of differential stress, making it difficult to discriminate between various models.

An important caveat of previous studies is that they have investigated pure ε-Fe, but the core is known to also contain other elements. Ni is expected to be present at approximately 5 weight percent (wt%) (e.g., McDonough & Sun, 1995), but Fe–Ni is too dense and seismically fast to account for core properties, so a much lighter element must also be present (Birch, 1964). The identity of the light element(s) is one of the most controversial problems in deep Earth geophysics, but Si is a leading contender based on its ability to partition into the metallic phase during core formation (e.g., Fischer et al., 2015; Siebert et al., 2013) and the isotopic (Georg et al., 2007) and major-element (Ringwood, 1961) ratios of terrestrial rocks. Estimates of inner core Si based on density range as high as 7 wt% (Fischer et al., 2014; Tateno et al., 2015), but this should be considered an upper bound since Si is unlikely to be the sole alloying light element (e.g., Edmund et al., 2019; Ozawa et al., 2016).

The presence of alloying elements may alter the deformation mechanisms and resultant texture of the inner core. Metallurgical studies have demonstrated that Ni (e.g., Ledbetter & Reed, 1973) and Si (e.g., Ros-Yanez et al., 2007) can significantly alter

the mechanical properties of Fe. A previous experimental study (Reagan et al., 2018) on Fe–Ni alloys at high pressure did not characterize textures but found that addition of 5.5 wt% Ni could increase the strength (defined as the shear stress needed to induce plastic deformation) of Fe by 25% at inner core conditions. This increase alone is unlikely to change the dominant mechanism of inner core texturing, but a light element, possibly combined with strain hardening (Bergman et al., 2014), could further strengthen the alloy. Geodynamical models have difficulty reproducing seismic observations by imposing plausible flows on ε-Fe (Lasbleis & Deguen, 2015; Lincot et al., 2014), but this issue may disappear if alloy deformation textures are distinct from those of pure Fe. In this study, we measure both the strength and texture of deformed Fe–Ni–Si alloys to determine whether an alloying light element significantly changes the mode of plastic deformation or the interpreted strength of the inner core.

4.2 Methods

We investigated the properties of five Fe–Ni–Si alloys: Fe–9wt% Si (hereafter Fe–9Si) was a powder (Goodfellow FE166014); Fe–6Ni–8Si was synthesized in a piston-cylinder press at Harvard University (composition checked by energy dispersive spectroscopy); and Fe–5Si, Fe–5Ni–5Si, and Fe–5Ni–10Si were synthesized as foils by ultra-rapid quenching at the Institut de Chimie et des Matériaux de Paris-Est (details in Morard et al., 2011). We also prepared a sample of unalloyed Fe powder (Alfa Aesar G19X048) to attempt to reproduce literature results. Non-foil samples were loaded as powders and foil samples were laser-drilled into cylindrical slugs. All samples filled the sample chambers, which were 50 μm diameter cylindrical holes drilled into amorphous boron gaskets contained in Kapton supporting rings. This configuration allows X-rays to pass radially through the gasket and sample (Merkel & Yagi, 2005). A

Pt flake was loaded along with each sample as a pressure standard (Fei et al., 2007). Samples were compressed between diamonds with 200 μm diameter culets in panoramic piston-cylinder type diamond anvil cells (DAC) to initial pressures of 2–3 GPa. Additional compression was accomplished by an inflating gas membrane once the cell was on the beamline. We repeated the Fe–5Si experiment with double-sided laser heating during compression. For that experiment, gaskets were laser drilled from cubic boron nitride, and MgO flakes were used as thermal insulators and pressure standards (Speziale et al., 2001).

Experiments were conducted at Advanced Light Source beamline 12.2.2 (λ = 0.4613 or 0.4592 Å) with the DAC mounted with its compression axis orthogonal to the X-ray beam (Kunz et al., 2005). The detector was a mar345 positioned 385 or 386 mm from the sample with this distance calibrated by CeO_2 at ambient conditions. For each pressure step, a diffraction pattern was collected with a 120 second exposure. We used the program Dioptas (Prescher & Prakapenka, 2015) for live pattern integration, which allowed us to monitor phase changes and sample pressure during the experiment. Diffraction patterns were collected as the samples were gradually compressed to 50–60 GPa, near the maximum stability of the boron gaskets (Merkel & Yagi, 2005). Membrane pressure was then released over several hours while simultaneously collecting decompression patterns. Diffraction data were analyzed via Rietveld refinement (McCusker et al., 1999) in the crystallographic software package MAUD (Lutterotti et al., 1999). We analyzed several diffraction patterns for each experiment, including at least one pattern in the body-centered cubic (bcc) and the bcc–hcp transition regions, and at least four in the hcp region. Patterns were chosen based on their diffraction intensity, possession of sufficient Pt diffraction to refine an accurate pressure, and equally spaced coverage of the experiment's pressure range.

These patterns were refined over a 2θ range of 11.5–25° and unit cell dimensions and elastic strains were compiled for the hcp phase of each sample (Table C.1). Textures were calculated using the Extended Williams-Imhof-Matthies-Vinel (E-WIMV) model (Chateigner et al., 2019) with fiber symmetry imposed about the axis of compression. Orientation density functions were refined at a resolution of 15°, exported to BEARTEX (Wenk et al., 1998), and smoothed with a 10° Gaussian filter prior to plotting as inverse pole figures (Section 4.3). The pressures of phase transitions in 300 K samples may not necessarily be the same as at equilibrium due to sluggish kinetics, starting material effects, and non-hydrostaticity, but the measured texture and strength of the phases present are still accurate.

4.3 Deformation Textures

As in pure Fe, our alloy samples transformed from the bcc (or bcc-like: Fischer et al., 2013) structure to the hcp structure upon compression. The deformation textures of our room-temperature experiments are shown in Figure 4.1. The bcc textures are near-identical to those of pure Fe (e.g., Merkel et al., 2004; Miyagi et al., 2008), varying only in the strength of the 100 maximum. The similarity across compositions suggests that sufficient plastic flow occurred prior to the bcc–hcp transition to homogenize the textures (except for possibly in Fe–9Si, which may have led to its distinctive hcp texture). Once the transition to hcp is complete, the alloy textures show two distinct maxima: one near $11\bar{2}0$ and one near 0001. The non-foil samples (Fe–9Si and Fe–6Ni–8Si) are distinguished by the absence of the latter maximum; these were mechanically strong (Section 4.4) but weakly textured, perhaps indicating that plastic flow was impeded in these experiments. The non-foil textures are likely the result of dominant compressive $\{2\bar{1}\bar{1}2\}\langle 2\bar{1}\bar{1}3\rangle$ twinning. This deformation

mechanism is known to occur at large strains and low temperatures in ε-Fe (Kanitpanyacharoen et al., 2012; Merkel et al., 2004), so its presence at 300 K in our strongest alloys is reasonable. The foil experiments were more strongly textured (showing strong maxima at $11\bar{2}0$ and 0001), so they may be better representative of texture development by dislocations (the type of deformation texturing proposed to occur in the inner core; see Section 4.4). Polycrystal plasticity simulations of hcp metals (e.g., Chapuis & Liu, 2015; Kanitpanyacharoen et al., 2012; Miyagi et al., 2008; Wenk et al., 2000) have shown that basal $(0001)\langle 2\bar{1}\bar{1}0\rangle$ slip produces the 0001 maximum, while pyramidal $\{2\bar{1}\bar{1}2\}\langle 2\bar{1}\bar{1}3\rangle$ slip produces the $11\bar{2}0$ maximum. A large pyramidal contribution can result in a ~30° shift in the 0001 maximum (Miyagi et al., 2008; Merkel et al., 2013), as is seen in the Fe–5Ni–10Si textures. Together, these foil textures show evidence of significant pyramidal slip. Since basal slip is typically observed to dominate ε-Fe deformation at 300 K (e.g., Nishihara et al., 2018), we surmise that addition of Si increases the activity of pyramidal slip. Prismatic $\{10\bar{1}0\}\langle\bar{1}2\bar{1}0\rangle$ slip is also likely to be active without producing a distinct textural signature (Merkel et al., 2004).

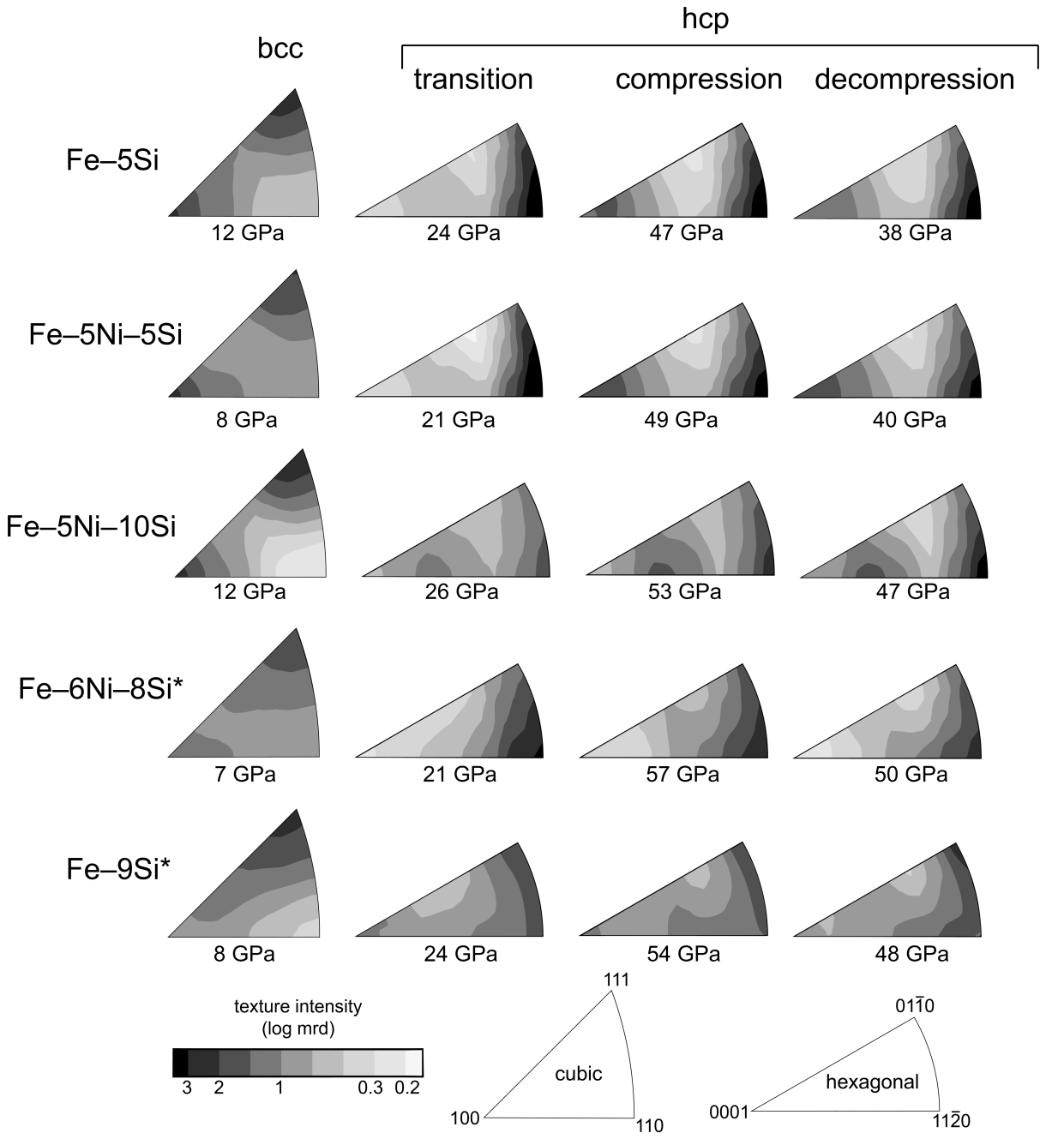

Figure 4.1: Inverse pole figures (IPFs) showing deformation textures at 300K. The bcc textures were collected below hcp stability, "transition" textures were collected during bcc–hcp coexistence, "compression" textures were collected approaching peak sample pressure (in the hcp-only regime), and "decompression" textures were collected after the sample relaxed by 5–10 GPa. Sample textures remained consistent upon decompression, in contrast to Miyagi et al. (2008). Asterisks indicate non-foil starting materials (Section 4.2). All IPFs are plotted on the same intensity scale, quantified as multiples of randomly distributed crystallographic orientations (mrd). Typical pressure uncertainties are ~5%.

Laser-heated deformation textures of a separate Fe–5Si experiment are shown in Figure 4.2. Compared to the 300 K data, the high-temperature textures show a basal slip maximum focused in the 0001 direction and much stronger in intensity than the pyramidal maximum at $11\bar{2}0$. Consistent with the phase relations reported by Komabayashi et al. (2019), a few face-centered cubic (fcc) grains (<2 volume % from the Rietveld refinement) crystalized above 1400 K (Figure C.3), but they are likely too scarce to have influenced the texture; Miyagi et al. (2008) did not observe hcp textural changes even at higher fcc abundances. Focused 0001 textures previously observed in pure Fe have been attributed to basal slip (Nishihara et al., 2018; Wenk et al., 2000) and tensile twinning (Merkel et al., 2012). Since heating disrupts twinning mechanisms, and there is no textural evidence for strong pyramidal slip (unlike at 300 K), it seems that deformation at high temperatures favors basal slip. This effect was previously suggested for ε-Fe by Steinle-Neumann et al. (2001) and could be associated with the high temperature breakdown of $\langle c + a \rangle$ deformation mechanisms observed in other hcp metals (Fan et al., 2017; Poirier & Langenhorst, 2002).

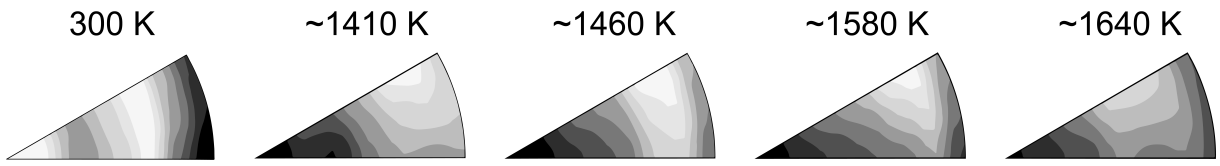

Figure 4.2: IPFs of the hcp phase from diffraction images taken in the laser-heated Fe–5Si experiment. The 300 K pole figure was collected at 24 GPa (prior to any laser heating), and the others were taken consecutively during a cycle of simultaneous heating and compression at 43–46 GPa. The basal slip maximum at high temperatures is stronger and more focused on 0001 compared to 300 K textures, while a weaker local maximum appears to persist at $11\bar{2}0$, suggesting continued pyramidal slip activity. This texture persisted upon temperature quenching. Geometries and intensity scales are the same as in Figure 4.1. Typical temperature uncertainties are ~10%.

The relative dominance of basal and pyramidal slip systems may be significant to our understanding of the inner core. As mentioned above, most studies predict basal slip to dominate ε-Fe deformation at deep-Earth conditions since this mechanism produces strong 0001 textures analogous to the observed polar anisotropy (e.g., Wenk et al., 2000). We see this same texture in our heated experiment, so we cannot rule out this interpretation. However, some studies (e.g., Lincot et al., 2016; Steinle-Neumann et al., 2001) have suggested that pyramidal slip may be required to match seismic observations. In that case, our finding of significant pyramidal activity in Si-bearing alloys may help explain the discrepancy between the observed and expected modes of plastic deformation. Of course, it is also possible that the inner core texture is a solidification product and was not created by plastic deformation at all (Section 4.4.4).

4.4 Alloy Strength

Our experiments allow us to measure elastic stress in the sample and quantify its dependence on pressure and temperature. Calculating mechanical strength also requires knowledge of the alloys' shear moduli, the values of which were taken from previous studies. We extrapolate these parameters to inner core conditions to compare the mechanical strength implied by our experiments to previously-published estimates for Fe and Fe–Ni.

4.4.1 Strength Calculations

The yield strength of a material is defined by the boundary between stresses low enough to be supported elastically and stresses high enough to induce plastic deformation (i.e., flow). In our experiments, the elastic stress resolved on a specific diffraction peak is determined by the dimensionless parameter $Q(h\,k\,l)$, where h, k, and

l are the Miller indices of the peak. This parameter is related to deviatoric (i.e., differential) stress by:

$$Q(h\ k\ l) = \frac{t}{3}\left[\frac{\alpha}{2G_R(h\ k\ l)} + \frac{(1-\alpha)}{2G_V}\right] \quad (4.1)$$

where G_V is the Voight approximation shear modulus, $G_R(h\ k\ l)$ is the Reuss approximation shear modulus of the peak (Anderson, 1965), α is a weighting factor, and t is the deviatoric stress:

$$t = \sigma_1 - \sigma_3 \quad (4.2)$$

where σ_1 and σ_3 are the maximum and minimum stress components, respectively (Singh et al., 1998). Calculating $G_R(h\ k\ l)$ requires single-crystal compliance moduli (S_{ij}) for the sample material under conditions of hydrostatic pressure. Since these are seldom available, it is common to assume $G_R(h\ k\ l) = G_V = G$, where G is the aggregate shear modulus, a measurable quantity. These assumptions reduce Equation 4.1 to:

$$t = 6G\langle Q(h\ k\ l)\rangle \quad (4.3)$$

where $\langle Q(h\ k\ l)\rangle$ (hereafter Q) is an average across all observed peaks in a diffraction pattern. If the sample's yield strength has been exceeded and it is plastically flowing, elastic deformation cannot accommodate any more strain, the peaks are expressing their maximum possible Q, and t is equal to the material's yield strength (Hemley et al., 1997). Determining alloy strengths at conditions relevant to the inner core requires extrapolating both G and Q to high pressures (>330 GPa) and temperatures (>3000 K).

4.4.2 Extrapolation of Q

The pressure dependence of Q in our experiments is shown in Figure 4.3. Each experiment shows a positive linear relationship between P and Q, with four of the five

alloys having similar slopes and Fe–5Ni–5Si exhibiting a shallower pressure dependence. There are no apparent experimental reasons for this deviation; Fe–5Ni–5Si is intermediate among the sample compositions, did not have large uncertainties in Q, had the same dimensions as the other samples, and the other two foil experiments did not exhibit shallow slopes. Extrapolating each trend to inner core pressures (Figure 4.3 inset) results in indistinguishable values for each experiment except Fe–5Ni–5Si. Since there does not appear to be a compositional trend in Q values, and we cannot rule out the shallower ${}^{\partial Q}/_{\partial P}$, the following analysis will present results using both a fit to all the experimental alloys (${}^{\partial Q}/_{\partial P} = (1.1 \pm 0.1) \times 10^{-4}$ GPa^{-1}) and a fit to only Fe–5Ni–5Si (${}^{\partial Q}/_{\partial P} = (4.4 \pm 0.9) \times 10^{-5}$ GPa^{-1}). Both fits are steeper than our Fe measurements and literature values for Si-free alloys. For example, the steepest value found by Regan et al. (2018) was ${}^{\partial Q}/_{\partial P} \approx 3 \times 10^{-5}$ GPa^{-1} for Fe–20Ni, and we found ${}^{\partial Q}/_{\partial P} = (1.0 \pm 0.6) \times 10^{-5}$GPa^{-1} for our own pure Fe sample.

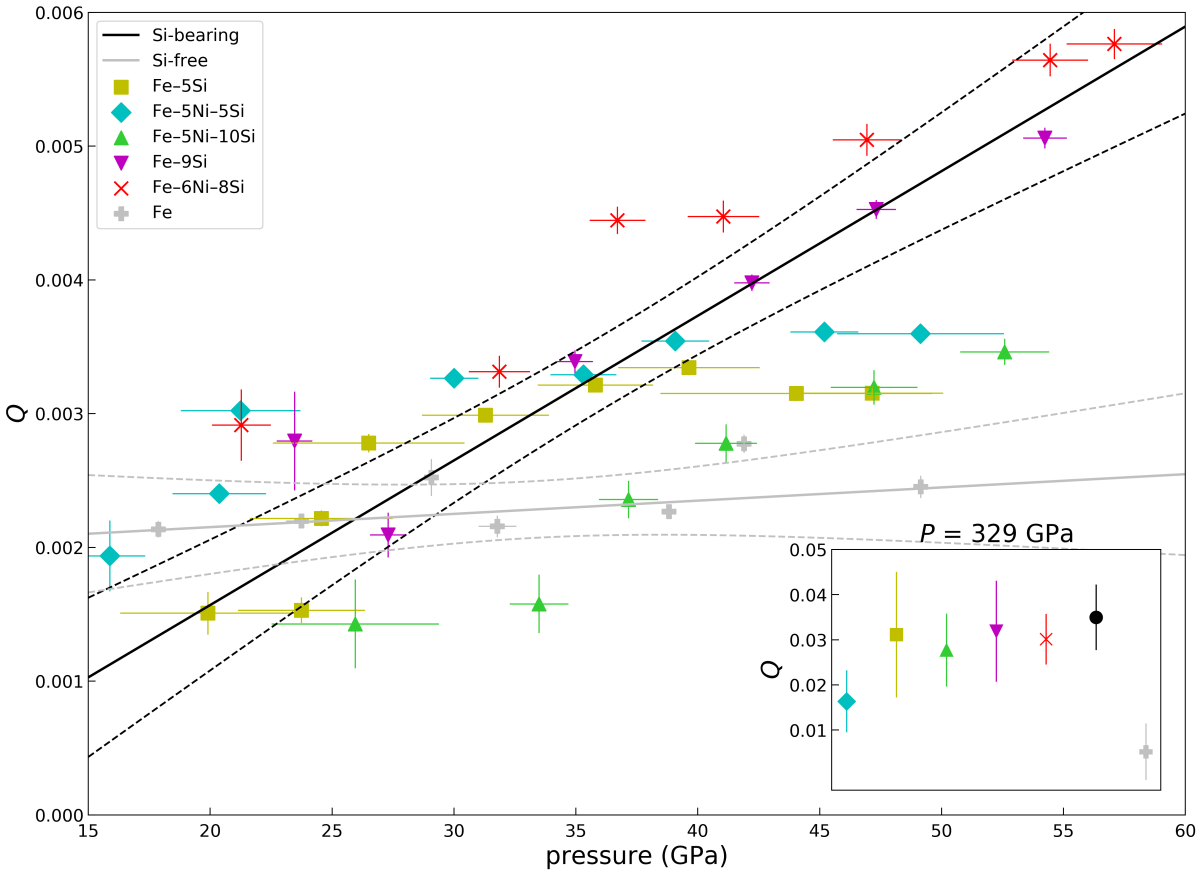

Figure 4.3: Pressure evolution of $\langle Q(h\ k\ l)\rangle$ for the hcp phase of each composition at 300 K. While Fe is noticeably weak, relative strengths between the alloys do not appear to show significant compositional dependence, even within the three experiments (Fe–5Si, Fe–5Ni–5Si, Fe–5Ni–10Si) synthesized as foils. All these data were collected on compression. Fits to $^{\partial Q}/_{\partial P}$ for each composition (not shown), all Si-bearing data (solid black line), and pure Fe (solid grey line) were calculated by orthogonal distance regression considering the error bars of each point (dashed lines are 95% confidence intervals). **Inset:** These fits (and 95% confidence intervals) extrapolated to the inner core boundary pressure. Fe–5Ni–5Si is noticeably weaker than the other alloys, but it is still stronger than pure Fe.

Our laser-heated Fe–5Si experiment allows us to estimate the effect of temperature on Q. As expected, high temperatures enhance plastic deformation, reducing the elastically-supported strain and resulting in Q reduction at a rate of $^{\partial Q}/_{\partial T} = (-1.60 \pm 0.36) \times 10^{-6}\ \mathrm{K}^{-1}$ (Figure C.1). There are significant experimental

limitations to this technique; the minimum power threshold for laser emission prevents measurements at intermediate temperatures, and laser heating generates large temperature gradients in the sample. However, Merkel et al. (2013) constrained the temperature effect on pure Fe by compiling data from several resistive-heated DAC and multi-anvil experiments, and their reported alloy strengths imply $^{\partial Q}/_{\partial T}$ consistent with our value for reasonable (i.e., H. Mao et al., 1999) values of G (Equation 4.3). Previous studies that extrapolated experimental values to inner core conditions (Gleason & Mao, 2013; Regan et al., 2018) assumed $^{\partial Q}/_{\partial T} = 0\ \mathrm{K}^{-1}$, meaning their calculated inner core strengths were upper bounds. In the following analysis, we recalculate their results using our estimated $^{\partial Q}/_{\partial T}$ value.

4.4.3 Extrapolation of G

In addition to Q, it is necessary to extrapolate the shear modulus (G) to core-relevant conditions (Equation 4.3). Although Dubrovinsky et al. (2000) describes a technique to determine G values by Rietveld refinement, this requires high-quality and quasi-hydrostatic diffraction, restrictions incompatible with radial geometry experiments. Relatively few studies report shear modulus values, but with the relationships:

$$V_S = \sqrt{\frac{G}{\rho}} \tag{4.4}$$

$$V_P = \sqrt{\frac{K+\frac{4}{3}G}{\rho}} \tag{4.5}$$

(where V_S is shear velocity, V_P is compressional velocity, ρ is density, and K is bulk modulus), G can be extracted from studies that simultaneously measured density and

velocity. Figure 4.4 shows G versus P for available experimental data from the literature on Si-bearing hcp alloys. There is a clear difference between experimental techniques, with nuclear-resonant inelastic X-ray scattering (NRIXS) studies finding systematically lower G values than inelastic X-ray scattering (IXS) or acoustic methods. The compositional effect is also reversed between techniques, with NRIXS implying that alloying Si reduces G and IXS implying that Si increases G. We will use NRIXS values for the following calculations since experimental uncertainties are sufficient to make extrapolated results of the techniques overlap at inner core conditions (Figure 4.4 inset). Note that while a linear G versus P relationship is experimentally supported at least to 220 GPa (H. Mao et al., 1999), a sublinear relationship could potentially reduce the shear modulus at inner core conditions.

Following the method of previous high-pressure strength studies (Gleason & Mao, 2013; Reagan et al., 2018), we extrapolated G using the formalism of Steinburg et al. (1980):

$$G(P,T) = G_0 + \frac{\partial G}{\partial P}\frac{P}{\left(\rho/\rho_0\right)^{1/3}} + \frac{\partial G}{\partial T}(T-300) \tag{4.6}$$

where subscript 0 indicates ambient conditions (T = 300 K, P = 1 bar) and ρ is molar density. Values of G_0 and $\partial G/\partial P$ are taken from the NRIXS fit shown in Figure 4.4, ρ_0 is from equation of state literature (Fe–5Si from Edmund et al., 2019; Fe–5Ni–5Si from Edmund et al., 2020; other alloys calculated from these and the pure Fe values of Dewaele et al., 2006), ρ is the PREM inner core density, and $G(P,T)$ is calculated from ρ and the PREM inner core shear velocity (Dziewonski & Anderson, 1981). Selecting locations in the inner core, namely the inner core boundary (ICB) and inner core center (ICC), allows $\partial G/\partial T$ to be solved at the corresponding pressure and temperature

conditions. This calculation implicitly assumes that the inner core has the same composition as the material used to derive the other parameters, which is most reasonable for compositions with Ni and Si. The calculation is also subject to the large (but difficult to quantify) uncertainty on the temperature of the inner core (e.g., Karato, 2008). Considering this, we elected to use the same inner core temperatures as Gleason & Mao (2013) and Reagan et al. (2018) (5500 K at the ICB, 6200 K at the ICC) to ensure that our results are directly comparable to their Si-free results; the differences between studies are not dependent on the specific pressure and temperature. Calculated $^{\partial G}/_{\partial T}$ values vary little between compositions; average values are –0.050 ± 0.008 GPa K^{-1} at the ICB and –0.043 ± 0.006 GPa K^{-1} at the ICC. These values are smaller than the corresponding values of Fe–12Ni (Reagan et al., 2018) and Fe (Gleason & Mao, 2013) by a factor of 1.25 and a factor of 2 respectively because of our smaller $^{\partial G}/_{\partial P}$ term.

4.4.4 Mechanical strength of the inner core

Calculated alloy strength as a function of temperature is shown in Figure 4.5. Merkel et al. (2013) calculated trends directly as a function of t (rather than treating G and Q individually) based on several data spanning different studies and techniques. Extrapolating, their results imply a stronger Fe than Gleason & Mao (2013) but still consistently weaker than our Si-bearing values. Even the Fe–5Ni–5Si experiment (with shallow $^{\partial Q}/_{\partial P}$) is stronger than all Si-free compositions. If solid state deformation occurs in the inner core, this enhanced strength may influence our interpretation of whether deformation is dominated by the flow of atoms towards concentrations of vacancy defects (diffusion creep) or the movement of lattice dislocations (power-law creep). Van Orman (2004) suggested the additional possibility of dislocation flow via "Harper-Dorn creep", but this mechanism is controversial (e.g., Kassner et al., 2015).

Adjudicating between mechanisms is important because diffusion creep typically does not produce lattice-preferred orientation and thus would not generate anisotropy. Therefore, if the inner core is in a diffusion-dominated regime, this would tend to support anisotropy developing during crystallization rather than afterwards.

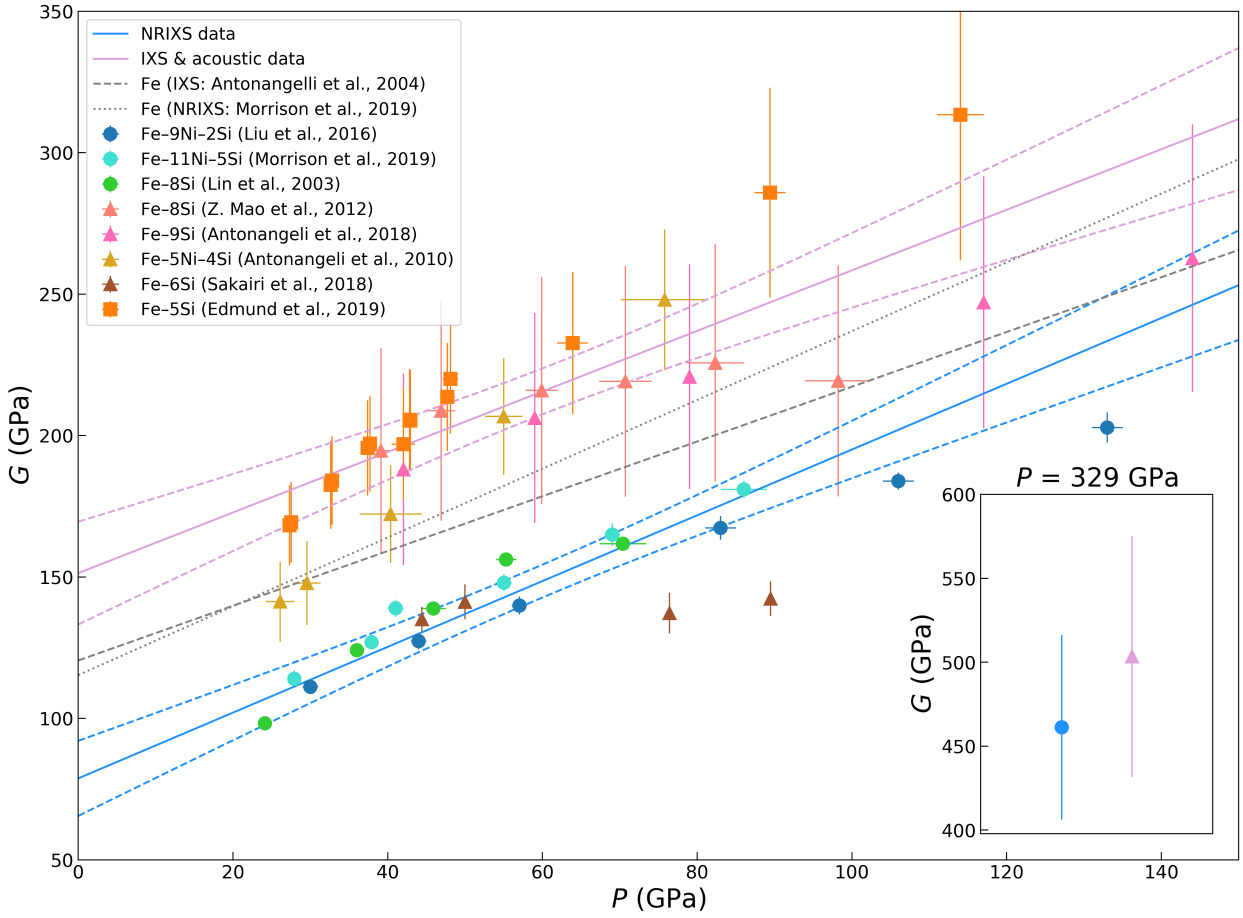

Figure 4.4: Published experimental values of the shear moduli of hcp Fe–Si and Fe–Ni–Si alloys at 300 K, either explicitly reported or implied (i.e., Equations 4.4 and 4.5). The pink line is a fit to data collected by IXS and picosecond acoustic techniques (triangles and squares, respectively), excluding Sakairi et al. (2018). The blue line is a fit to NRIXS data (circles) and is corrected for ^{57}Fe enrichment. Both fits are calculated irrespective of composition by orthogonal distance regression and are shown with 95% confidence intervals (dashed lines). Fits to measurements of pure ε-Fe (grey lines) are shown for context. **Inset:** Alloy fits extrapolated to 329 GPa. At this pressure, the techniques are indistinguishable within error.

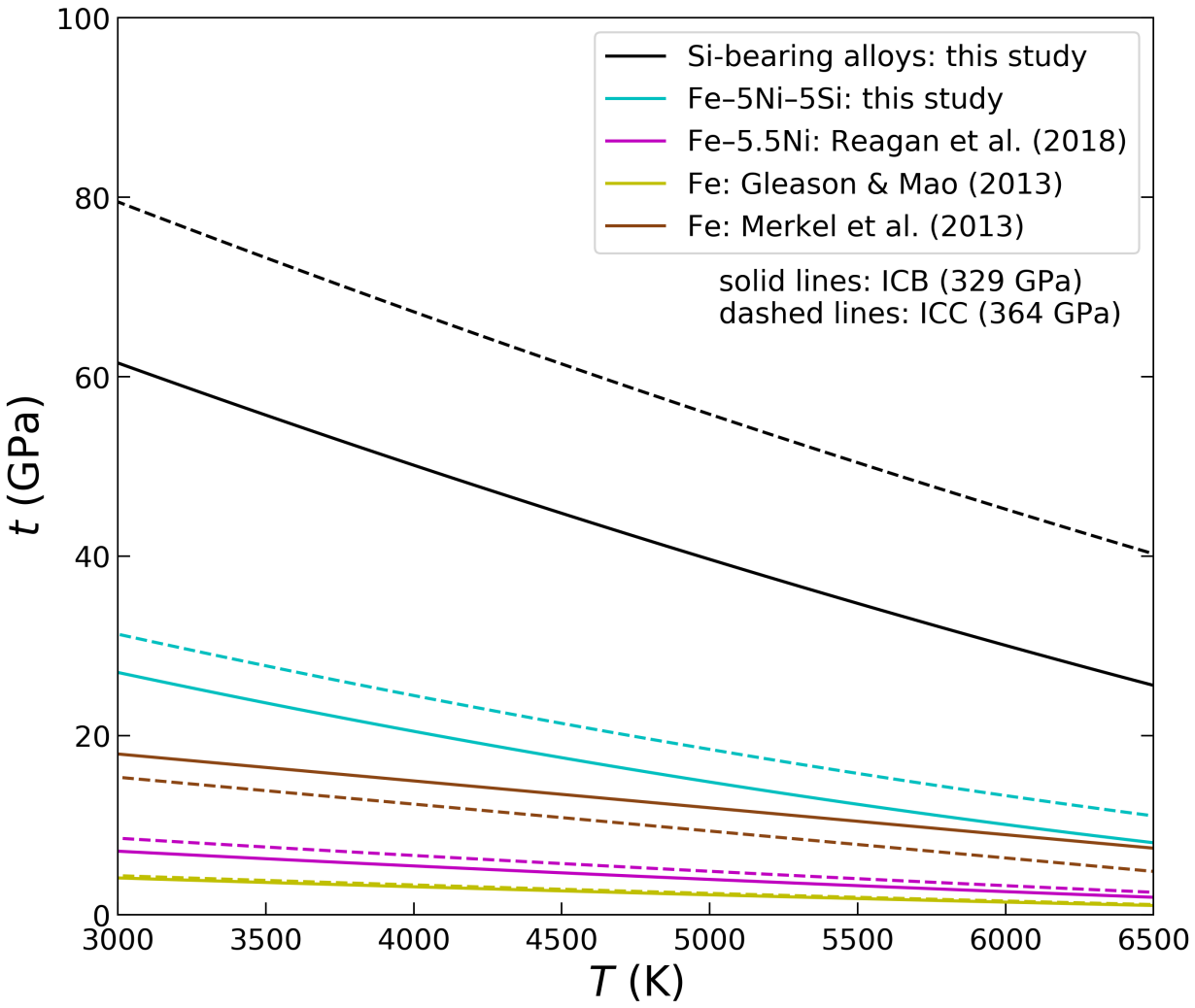

Figure 4.5: Alloy strength in the inner core as a function of temperature. Curves from Merkel et al. (2013) use that study's parametrization while those for other studies have been recalculated using Equation 4.6 and including $^{\partial Q}/_{\partial T}$. Curves from Reagan et al. (2018) assume that study's experimentally-determined strength ratio between Fe–5.5Ni and Fe–20Ni is constant with pressure and temperature. At inner core conditions, alloys which contain Si are significantly stronger than alloys without a light element. The calculated magnitude of this strengthening effect is reduced for the Fe–5Ni–5Si fit due to its smaller $^{\partial Q}/_{\partial P}$.

Gleason & Mao (2013) concluded that their pure Fe data were consistent with dislocation-dominated (power-law) creep since mechanical weakness enhances dislocation mobility, allowing geophysically-plausible stresses to produce the required strain rates. Figure 4.6 (panels a and b) compares their results to those of Reagan et al. (2018) and this study. For a given differential stress, dislocation velocities and strain rates are about one order of magnitude reduced for Si-bearing alloys compared to pure Fe. An approximately equal depression is obtained (for both velocity and strain rate) by moving from the ICB to the ICC for a given alloy. Figure 4.6c shows a calculation of the boundary between diffusion- and dislocation-dominated regimes based on the parametrization of Reaman et al. (2011), which depends on $G(P,T)$ and ρ, but not explicitly on t. Here, the depressed G values of Si-bearing alloys slightly enlarge the dislocation-dominated field. It is important to note that our knowledge of inner core properties is incomplete. Estimates of the inner core stress field (τ) span at least five orders of magnitude (Buffet & Wenk, 2001; Koot & Dumberry, 2011; Yoshida et al., 1996). Likewise, estimates of the inner core's grain size vary widely, with constraints from earlier studies (e.g., Bergman, 1998) permitting crystallites as small as several centimeters while more recent studies (e.g., Yamazaki et al., 2017) prefer much larger grain sizes. These uncertainties make it impossible to say definitively in which field the inner core lies. Additionally, inner core viscosity, itself a poorly constrained parameter, determines the relationship between applied stress and strain rate. Gleason & Mao (2013) suggested a viscosity range of 10^{15}–10^{19} Pa s assuming a pure Fe inner core and simple isotropic shear; our "all alloys" fit would be one order of magnitude more viscous under the same conditions.

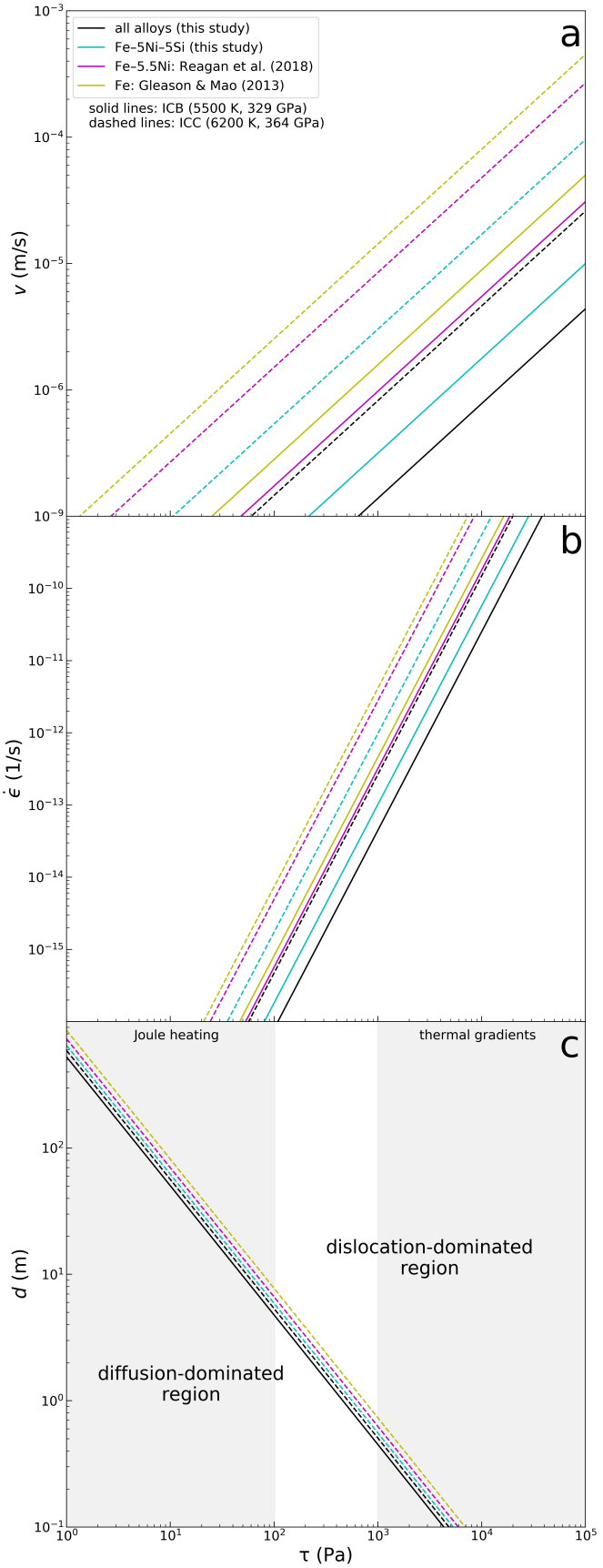

Figure 4.6: Dislocation velocity (**a**), strain rate (**b**), and critical grain size (**c**) as functions of differential stress τ. Equations and constants used are from Gleason & Mao (2013) and Reaman et al. (2011) and are listed in the Table C.2. For clarity, only the "all alloys" ICB line is plotted in (**c**); the other ICB lines would be similarly offset from their corresponding ICC lines. The shaded "thermal gradients" (Jeanloz & Wenk, 1988) and "Joule heating" (Takehiro, 2011) regions are representative examples of proposed inner core stress ranges (see Section 4.4).

4.5 Conclusions

We investigated hcp Fe–Ni–Si alloy deformation textures and strengths with high-pressure radial X-ray diffraction experiments. These alloys plastically deform by the same principal mechanisms documented in other hcp metals, though possibly with greater pyramidal slip activity compared to pure ε-Fe at 300 K. Upon laser heating, we observed a change in the distribution of crystallographic preferred orientations, which may suggest that basal slip is preferred at high temperatures. Experimental Fe–Ni–Si compositions are strong compared to previous Fe and Fe–Ni data and show significantly larger $^{\partial Q}/_{\partial P}$ values. Extrapolating to inner core conditions, Si-bearing alloys may be up to an order of magnitude stronger than pure Fe. This would reduce the mobility of anisotropy-favoring lattice dislocations by an equal factor. A mechanically strong inner core generally favors deformation by non-texturing diffusion creep and thus anisotropy as a crystallization (rather than a post-solidification) phenomenon. However, the large uncertainties on experimental and observational inner core parameters make it premature to conclude whether the strengthening effect of Si is significant in this regard.

Acknowledgements

We thank Timothy Cavanaugh for performing the alloy EDS measurements, Martin Kunz and Andrew Doran for their assistance on beamline 12.2.2, Feng Lin for his experimental assistance, two anonymous reviewers for their valuable comments, and the editor for handling this manuscript. This work was funded in part by a National Science Foundation Graduate Research Fellowship awarded to M.C. Brennan (DGE1745303) and by a Henry Luce Foundation award to R.A. Fischer. L. Miyagi acknowledges support from the National Science Foundation through EAR-1654687. This work has been partially supported by the US Department of Energy National Nuclear Security Administration through the Capital-DOE Alliance Center which provided financial support for S. Couper (DE-NA0003858). D. Antonangeli has received funding from the European Research Council under the European Union's Horizon 2020 research and innovation program (grant agreement No. 724690). The Advanced Light Source is a Department of Energy Office of Science User Facility (contract no. DE-AC02-05CH11231). Beamline 12.2.2. is funded in part by the Consortium for Materials Properties Research in Earth Sciences (COMPRES) under NSF Cooperative Agreement EAR 10-43050. Part of this work was performed at the Harvard University Center for Nanoscale Systems, a member of the National Nanotechnology Coordinated Infrastructure Network, which is supported by the National Science Foundation (award no. 1541959).

Appendix A
Supplemental Material for Chapter 2

A.1 Composition and Oxygen Fugacity of Martian Building Blocks

The bulk Martian composition used in this study was based on a CI chondrite enriched in refectory elements. CI material alone cannot account for the oxygen isotopic composition (Javoy, 1995) or Fe/Si ratio (Bertka and Fei, 1998) of Mars, but the differences in predicted mantle compositions between CI-based models and those with more complicated mixtures of meteorite groups are modest (Lodders and Fegley, 1997; Sanloup et al., 1999). We used the CI abundances of Palme and O'Neil (2014) and considered each element present at >1 wt% (H, C, N, O, Mg, Al, Si, S, Ca, Fe, Ni), as well as some minor and trace elements of interest (Na, P, K, Ti, V, Cr, Mn, Co, W). Elements were classified as highly volatile, moderately volatile, or refractory based on the criteria of Palme and O'Neil (2014). The highly volatile elements (H, C, N, O) were removed. These elements have condensation temperatures <200 K (Lodders, 2003) and are highly depleted in terrestrial planets (Albarède, 2009). Oxygen was added back in the initial equilibration step based on the imposed primordial oxygen fugacity (fO_2). The refractory element enrichment factor comes from Taylor (2013), who determined that the moderately volatile lithophile elements are depleted in the bulk silicate Mars to roughly the same extent as one another, and that the elemental budgets implied by this depletion are consistent with a 1.9× refractory enrichment of the bulk planet.

The Martian building blocks were produced by differentiating this starting material at 1 GPa, 1810 K, and a fixed fO_2, which was a free parameter. Oxygen fugacity was calculated as:

$$\Delta IW = 2 \times \log_{10}\left(\frac{a_{FeO}^{silicate}}{a_{Fe}^{metal}}\right) = 2 \times \log_{10}\left(\frac{\gamma_{FeO}^{silicate} X_{FeO}^{silicate}}{\gamma_{Fe}^{metal} X_{Fe}^{metal}}\right) \quad \text{(A.1)}$$

in log units relative to the iron–wüstite (IW) buffer, where a_i^j, γ_i^j, and X_i^j are the activity, activity coefficient, and mole fraction, respectively, of component *i* in phase *j*. The value of γ_{Fe}^{metal} was calculated after Ma (2001), accounting for the alloying effects of S and Ni based on the Steelmaking Data Sourcebook (Japan Society for the Promotion of Sciences, 1988), and $\gamma_{FeO}^{silicate}$ was taken as 1.7 (Holzheid et al., 1996; O'Neill et al., 2002). Fixing an initial fO_2 also fixes the partition coefficient of iron, defined as:

$$D_{Fe} = \frac{X_{Fe}^{metal}}{X_{FeO}^{silicate}} \tag{A.2}$$

and thus determines the iron contents of the core and mantle.

The partitioning behavior of each element *M* with valence *n* was defined by a partition coefficient:

$$D_M = \frac{X_M^{metal}}{X_{MO_{n/2}}^{silicate}} \tag{A.3}$$

or an exchange coefficient:

$$K_D^M = \frac{D_M}{D_{Fe}{}^{n/2}} \tag{A.4}$$

which was defined as $K_D^O = \frac{X_{Fe}^{metal} X_O^{metal}}{X_{FeO}^{silicate}}$ in the case of oxygen (e.g., Frost et al., 2010).

A.2 High Pressure–Temperature Metal–Silicate Partitioning

A few elements (Mg, Al, Ca, Na, K) were assumed to be perfectly lithophile (White, 2013). Partition coefficients for Ni, Co, Cr, Ti, Mn, V, P, and W were calculated using:

$$\log_{10}(D_M) = a + \frac{b}{T} + \frac{c \times P}{T} + d \times \left(\frac{nbo}{t}\right) - \frac{n}{2} \times \log_{10}\left(\frac{1}{D_{Fe}}\right) - \log_{10}\left(\frac{\gamma_M^{metal}}{\gamma_{Fe}^{metal\,n/2}}\right) \quad \text{(A.5)}$$

(Corgne et al., 2008; Siebert et al., 2011), where T is temperature, P is pressure, a, b, c, and d are constants based on experimental data (Table A.1), and $\frac{nbo}{t}$ (non-bridging oxygen atoms per tetrahedron) was fixed at 2.5. The composition-dependent activity coefficients γ_M^{metal} and γ_{Fe}^{metal} were calculated based on Ma (2001), with the activity parameters taken from the Steelmaking Data Sourcebook (Japan Society for the Promotion of Sciences, 1988). Exchange coefficients for Si and O were calculated using:

$$\log_{10}(K_D^M) = a + \frac{b}{T} + \frac{c \times P}{T} \quad \text{(A.6)}$$

(Fischer et al., 2015). For O, we additionally calculated the effect of S composition dependence after Equation 3 of Fischer et al. (2015). Partitioning of S was calculated using:

$$\begin{aligned}\log_{10}(D_S) = {} & \log_{10}\left(M_{FeO}^{silicate}\right) - \log_{10}\left(C_{Sulfide}\right) + \frac{b}{T} + \frac{c \times P}{T} + d\log_{10}\left(1 - M_{Si}^{metal}\right) \\ & + e\log_{10}\left(1 - M_{Si}^{metal}\right)^2 + f\log_{10}\left(1 - M_{Si}^{metal}\right)^3 + g\log_{10}\left(1 - M_C^{metal}\right) \\ & + h\log_{10}\left(1 - M_{Fe}^{metal}\right) + i\log_{10}\left(1 - M_{Ni}^{metal}\right) + j\log_{10}\left(1 - M_O^{metal}\right) + k \quad \text{(A.7)}\end{aligned}$$

(Boujibar et al., 2014), where a through k are experimental constants (Table A..1), M_A^{metal} is the mass fraction of element A in the metal, $M_{FeO}^{silicate}$ is the mass fraction of FeO in the silicate, and $C_{Sulfide}$ is the sulfide capacity of the silicate. This composition-

dependent parameterization can be used only if the elemental abundances of the metal and silicate reservoirs are already known, but this is inappropriate for partitioning an initially homogeneous body. Therefore, for the initial equilibration step only, the partition coefficient of S was calculated using:

$$\log_{10}(D_S) = -4.37 + \frac{13686}{T} + \frac{217.49 \times P}{T} \quad \text{(A.8)}$$

with T in Kelvin and P in GPa (Rose-Weston et al., 2009).

Temperatures were calculated using the expression:

$$T = 0.3116 \times P^3 - 9.264 \times P^2 + 96.03 \times P + 1819 \quad \text{(A.9)}$$

with T in Kelvin and P in GPa, a fit to an experimentally determined liquidus curve for Martian silicates (Borg and Draper, 2003). The core mass fraction was determined by iteratively solving for core compositions until the core mass fraction converged on a single value. All accreted planetesimals had the same mass, core mass fraction, and composition.

It would be computationally difficult to simultaneously solve for the partitioning behavior of every element, so major and minor elements were partitioned first to enable calculation of composition-dependent partitioning of trace elements. We used the method of Rubie et al. (2011) to partition non-lithophile major and minor elements (Fe, Ni, Si, O) between the metallic and silicate components. Rubie et al. (2011) used the O activity model of Frost et al. (2010), but we instead used the oxygen partitioning parameterization of Fischer et al. (2015) (after Fischer et al., 2017). Following the methodology of Rubie et al. (2011), oxygen fugacity was evolved self-consistently. Rubie et al. (2011) only accounted for Fe, Ni, Si, and O as components of the metal, so we partitioned S along with the rest of the elements and iterated to

ensure that each step was self-consistent in terms of molar abundances. We did not include the effect of S on the partitioning of Si.

Trace elements and S were partitioned following the same procedure as in the primordial differentiation, with compositions calculated iteratively until convergence was obtained. After partitioning all elements, the composition of the proto-Martian core was updated by adding the unequilibrated portion of the impactor core and the metallic portion of the equilibrated material. Similarly, the proto-Martian mantle was updated to consist of the unequilibrated portion of the target mantle plus the silicate portion of the equilibrated material. This procedure of adding material, simultaneously solving for the major/minor elements, partitioning S and the trace elements, and updating the composition of the target was repeated for every accretionary step until the mass of Mars was reached. Uncertainties for the calculated compositions were evaluated using a Monte Carlo analysis; the model was run 3000 times with partition coefficients varied in a standard distribution according to the experimental studies' reported uncertainties (Table A.1).

A.3 Density and Sound Velocity Profiles for the Mantle

The mantle composition was used to construct mantle profiles of temperature, modal mineralogy, rigidity, density, and seismic wave speeds using Perple_X (Connolly, 2009). Given a *P*–*T* profile, Perple_X uses Gibbs free energy minimization to calculate a modal mineral phase assemblage, as well as density and seismic velocities (using the Voight-Royce-Hill approximation) for a given bulk composition. This calculation used the thermophysical dataset of Stixrude and Lithgow-Bertelloni (2011).

To convert the profile from density vs. pressure to density vs. depth, we used a spherically symmetric concentric-shell model, where the known gravity, radius, and pressure at the surface of Mars was used to infer the properties slightly deeper in the planet, iterating until the center was reached. At the center of Mars, the total radius for all shells equaled the planetary radius, and the gravitational acceleration at the base of the innermost shell was approximately zero (<0.02 m/s^2). The outermost shell extended from the surface to the base of the crust. For simplicity, we fixed crustal density as ρ_{crust} = 2.6 g/cm^3 (Goossens et al., 2017) and assumed a uniform crustal thickness. The volume of the crust can therefore be calculated as:

$$v_{crust} = \frac{4}{3}\pi[R^3 - (R - d_{crust})^3] \quad \text{(A.10)}$$

where R is the radius of Mars (~3390 km) and d_{crust} is the thickness of the crust. The mass of the crustal shell is:

$$m_{crust} = \rho_{crust} \times v_{crust} \quad \text{(A.11)}$$

and gravity at the base of the crust is:

$$g = \frac{G \times (M - m_{crust})}{(R - d_{crust})} \quad \text{(A.12)}$$

where G is the gravitational constant and M is 6.1417 x 10^{23} kg, the mass of Mars (Konopliv et al., 2011).

Calculating the concentric shells in the mantle was accomplished in much the same way, with the top and bottom of each shell defined by consecutive points along the P–T–ρ profile. We approximated shell density as the average of the densities at the top and bottom of the shell, then calculated the shell thickness required to account for the change in pressure between the top and bottom of the shell using the formula:

$$d_{shell} = \left(P_{bottom} - P_{top}\right)/\left(\rho_{shell} \times g_{top}\right) \quad \text{(A.13)}$$

This equation assumes that gravity does not change over the thickness of each thin shell. Shell volume, shell mass, and gravity at the base of the shell were calculated in the same way as for the crust, replacing R with the radius at the top of the shell and M with the mass of Mars minus the mass of all overlying shells.

A.4 Density and Sound Velocity Profiles for the Core

The Martian core was assumed to be a homogenous liquid alloy in the Fe–S system. The core S content is a function of the formational parameters discussed in Section 2.4 (bulk composition, volatile loss, partial equilibration, oxidation state, equilibration depth), so it was necessary to interpolate between equations of state for several alloys to calculate densities over a range of compositions. We interpolated between solid equations of state, fitting a line to their molar volumes as a function of mole fraction S (i.e., an assumption of ideal mixing). We then estimated the effect of melting with the Clapeyron equation:

$$\frac{dP}{dT} = \frac{L}{T\,\Delta V_{melting}} \quad \text{(A.14)}$$

where L is the specific latent heat, $\frac{dP}{dT}$ is the slope of the melting curve at a given pressure, and $\Delta V_{melting}$ is the volume change upon melting. The Fe–S eutectic melting curve of Campbell et al. (2007), which is approximately isochemical over the relevant pressure range, was used to estimate $\frac{dP}{dT}$. Measurements of a meteoritic metal–sulfide mixture (Mare et al., 2014) provided L at ambient conditions, which was approximated to be constant throughout Mars. The estimated $\Delta V_{melting}$ for the core alloy using this method are consistent with the actual $\Delta V_{melting}$ of Fe and FeS at high pressures (e.g.,

Anderson and Ahrens, 1994; Komabayashi and Fei, 2010; Nishida et al., 2011) (Section 4.4). The thermal expansivity (α) of a liquid alloy is greater than that of an isochemical solid, so we used an interpolated value between the α of liquid Fe (Anderson and Ahrens, 1994) and liquid FeS (Kaiura and Toguri, 1979) for temperatures above the Fe–S melting curve.

Interpolating between equations of state (Kombayashi et al., 2010; Seagle et al., 2006; Thompson et al., 2016; Urakawa et al., 2004) allowed us to calculate densities for a given *P*–*T* condition. At the core–mantle boundary (CMB), the *P*–*T* conditions were given by the lowermost mantle shell (plus the temperature increase associated with the CMB thermal boundary layer). For the rest of the core, we constructed an adiabat by slightly increasing the density of each alloy. An adiabatic change in density implies that the new temperature at this density is:

$$T = T_{CMB}\left(\frac{\rho}{\rho_{CMB}}\right)^{\gamma} \tag{A.15}$$

where γ is the Grüneisen parameter, calculated at the new density by:

$$\gamma = \frac{\alpha K_T}{\rho C_V} \tag{A.16}$$

where K_T is the isothermal bulk modulus, α is the thermal expansion coefficient, and C_V is specific heat, approximated by the Dulong-Petit law. At each compression step, we calculated a temperature along the adiabat for each of the alloys and interpolated between them to get ρ and T for our core composition. Repeating this procedure for incrementally larger compressions produced density and temperature profiles as a function of pressure along the adiabatic compression curve of the core alloy. The adiabatic bulk modulus (K_S) for each alloy was calculated as:

$$K_S = K_T(1 + \alpha\gamma T) \tag{A.17}$$

Since the core is molten, the seismic parameter reduces to:

$$\varphi = V_p{}^2 = \frac{K_S}{\rho} \tag{A.18}$$

allowing us to construct the compressional velocity profile of the core.

The adiabatic profile provided the pressure–density relationship needed to employ the concentric shell approach to the core. This procedure was done just as in the mantle: the shells were defined by pressure steps and we calculated the depth, mass, and gravity of each. When the gravity at the base of a shell goes to zero, the center of the planet has been reached. Each set of parameters was consistent with a single core radius, so it was necessary to adjust the CMB pressure until the zero-gravity point corresponds to the center of the planet.

A.5 Geophysical Properties of Bulk Mars

The mean moment of inertia can be calculated directly from the concentric shell model, assuming each shell is thin:

$$I = \frac{2}{3}mr^2 \tag{A.19}$$

where I is the shell inertia, m is the shell mass, and r is the shell's mean radius. The mean moment of inertia factor (MOI) for a spherically symmetric Mars is calculated by:

$$MOI = \frac{\sum I}{MR^2} \tag{A.20}$$

where M is the mass of Mars and R is the radius of Mars.

The elastic tidal Love number k_2 was calculated by the analytic formulation of Harrison (1963), which assumes a two-layer planet (core and mantle) parameterized by core radius, mean mantle density, mean core density, mean mantle rigidity (μ), and mean core rigidity. The rigidity of a liquid is 0, but the formula precludes this as a value, so we have set the core rigidity to an arbitrarily small number (0.0001×μ); the calculation is not sensitive to this value within two orders of magnitude. This simplified formula reproduces the results of more complete calculations following the method of Nimmo and Faul (2013) within 11% (personal communication with Nimmo). Additionally, the measured value of k_2 is frequency-dependent, so it was necessary to adjust the elastic value of our calculation to the diurnal frequencies of the spacecraft measurements used in the calculation of Konopliv et al. (2016). This was done by multiplying k_2 by $1+Q^{-1}$, where Q is the measured diurnal-period tidal dissipation factor of 88 (Nimmo and Faul, 2013). Together, these adjustments allow us to investigate the tradeoff between k_2, core size, and mantle rigidity (Figure A.4). Rigidity was calculated for each shell by rearranging the equation for shear velocity:

$$\mu = V_S^2 \rho \tag{A.21}$$

then volumetrically averaging the shells to obtain an approximate value for the bulk mantle. Note that the high FeO content of Mars increases the uncertainties of these values, as there are few available experimental data on the shear moduli of the Fe-rich endmembers of mantle minerals, especially high-pressure phases (Stixrude and Lithgow-Bertelloni, 2011). These data are uncertain by up to 17% in the case of Fe-wadsleyite (compared to 1.7% for Mg-wadsleyite and 3.9% in fayalite). Neglecting these experimental uncertainties, our calculated average mantle μ was 73 GPa. Using the k_2 calculation described above and accounting for the 11% uncertainty of this simplified

method compared to the full calculation, this μ corresponds to cores 1690–1870 km in radius (Figure A.4).

A.6 CMB Thermal Boundary Layer

A hypothetical thermal boundary layer (TBL) in the lowermost mantle must not cause the Martian core to exceed its maximum conductive heat flux or else it would induce core convection, which is inconsistent with the absence of a Martian dynamo. If the core's temperature profile is adiabatic, then the conductive heat flux out of the top of the core is related to alloy properties by:

$$F_c = \frac{\alpha \kappa_c \, g \, T}{C_p} \tag{A.22}$$

where κ_c is the core thermal conductivity, α is thermal expansivity, g is gravitational acceleration, T is the uppermost core temperature, and C_p is specific heat capacity. Nimmo and Stevenson (2000) found that the maximum value of F in a conductive Martian core was 19 mW/m^2. Updating the values of κ_c to 54 W K^{-1} m^{-1} (Suehiro et al., 2017) and α to 7×10^{-5} K^{-1} (Seagle et al., 2006) and recalculating for the case of a hot core (T = 2500 K) increases this limit to ~33 mW/m^2. This corresponds to a TBL temperature gradient (ΔT) of 500 K, which implies a mantle heat flux of:

$$F_m = \Delta T \frac{\kappa_m}{h} \tag{A.23}$$

where κ_m is mantle thermal conductivity and h is the height of the TBL. For a κ_m of 4 W K^{-1} m^{-1} (Kiefer and Li, 2016), $F_m < F_c^{max}$ for all h > 60 km. Thus, even large supra-adiabatic temperatures near the Martian CMB can be consistent with the absence of core convection.

A.7 Seismological Modeling

Seismological forward modeling was carried out to predict observable properties of both body waves traveling through Mars and normal mode oscillations of the planet. For each model, normal mode frequencies were estimated using Mineos (Masters et al., 2011). Anelastic predictions were made for each model, and the effect of gravity was included. To calculate body wave travel times, the TauP toolkit (Crotwell et al., 1999) was employed. A marsquake at a depth of 5 km was used in the calculations, though we note that the depth range over which marsquakes may occur is uncertain.

For the normal mode calculations, anelasticity was added to the seismic models of Mars, and the velocities were assumed to correspond to seismic waves propagating through Mars at 1 Hz. Bulk attenuation (Q_κ) was set to 57823 throughout as in the Preliminary Reference Earth Model, PREM (Dziewonski and Anderson, 1981). In the fluid core, shear attenuation (Q_μ) was set to zero. Mantle Q_μ was set to 130, as in Nimmo and Faul (2013), from the CMB to the Martian Moho. Crustal Q_μ was set to the PREM value of 600. Mode frequencies were computed using the self-coupling approximation throughout, and no mode splitting was considered.

A.8 Supplementary Figures

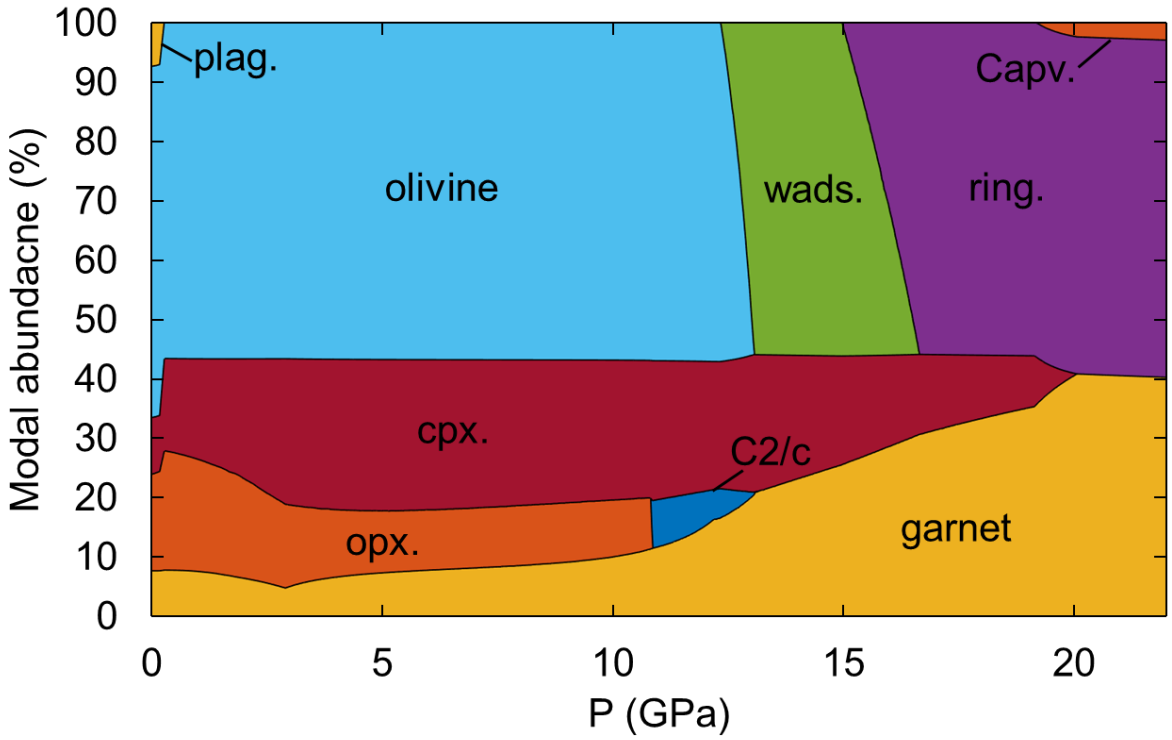

Figure A.1: Example of a calculated phase assemblage for the Martian mantle following an areotherm with a mantle potential temperature of 1600 K (Figure A.3). "Garnet" includes both the low-pressure and majorite polymorphs. Abbreviated phases are plagioclase (plag.), wadsleyite (wads.), ringwoodite (ring.), calcium perovskite (Capv.), clinopyroxene (cpx.), orthopyroxene (opx.), and high-pressure pyroxene (C2/c) (e.g., Hugh-Jones et al., 1994).

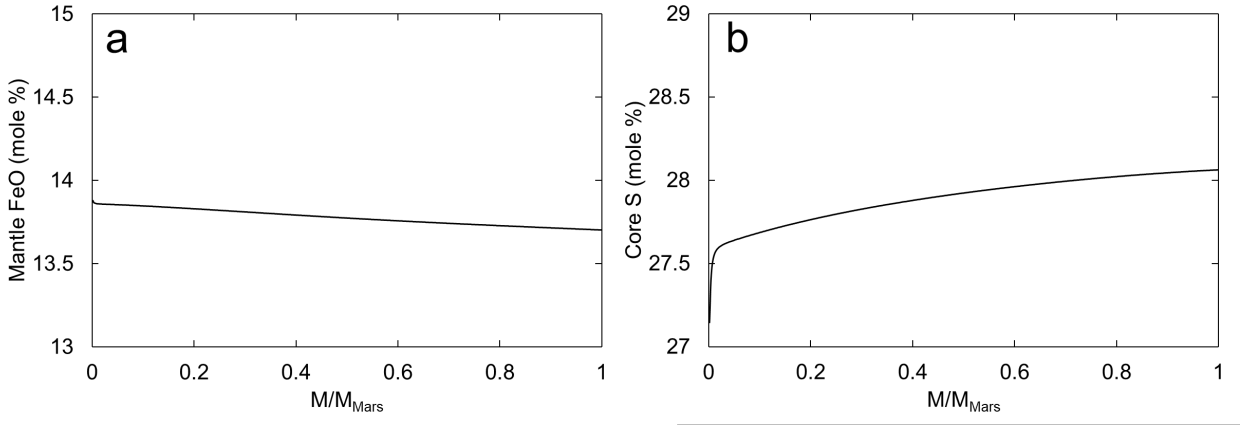

Figure A.2: Change in **(a)** the FeO content of the mantle and **(b)** the S content of the core over a simulated homogenous Martian growth history with initial fO_2 = IW–1.12, k_{core} = 0.9, k_{mantle} = 1.0, and P_{equil}/P_{CMB} = 0.55.

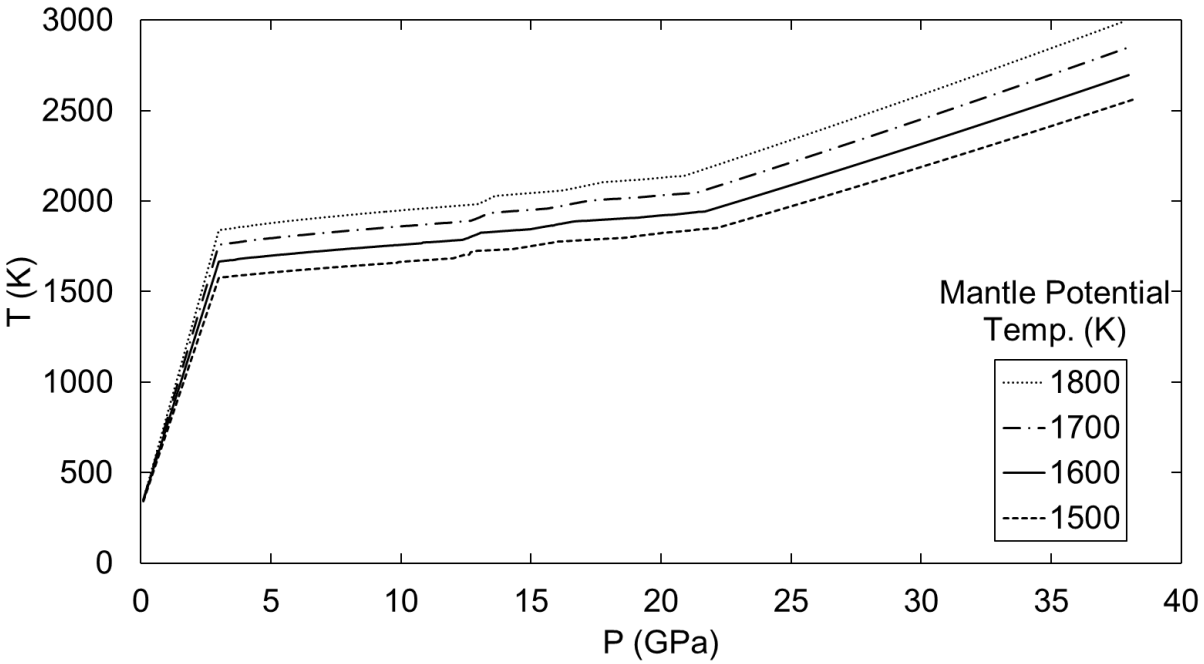

Figure A.3: Sample areotherms as a function of pressure. This range of mantle potential temperatures was chosen to bracket the modeled temperature profiles of Verhoeven et al. (2005) and Rivoldini et al. (2011). The steep temperature gradient near the surface is due to the presence of a conductive crust and lithosphere; no CMB thermal boundary layer is imposed. Note that each profile has a different core size due to the tradeoff between temperature and density (Section 4.4).

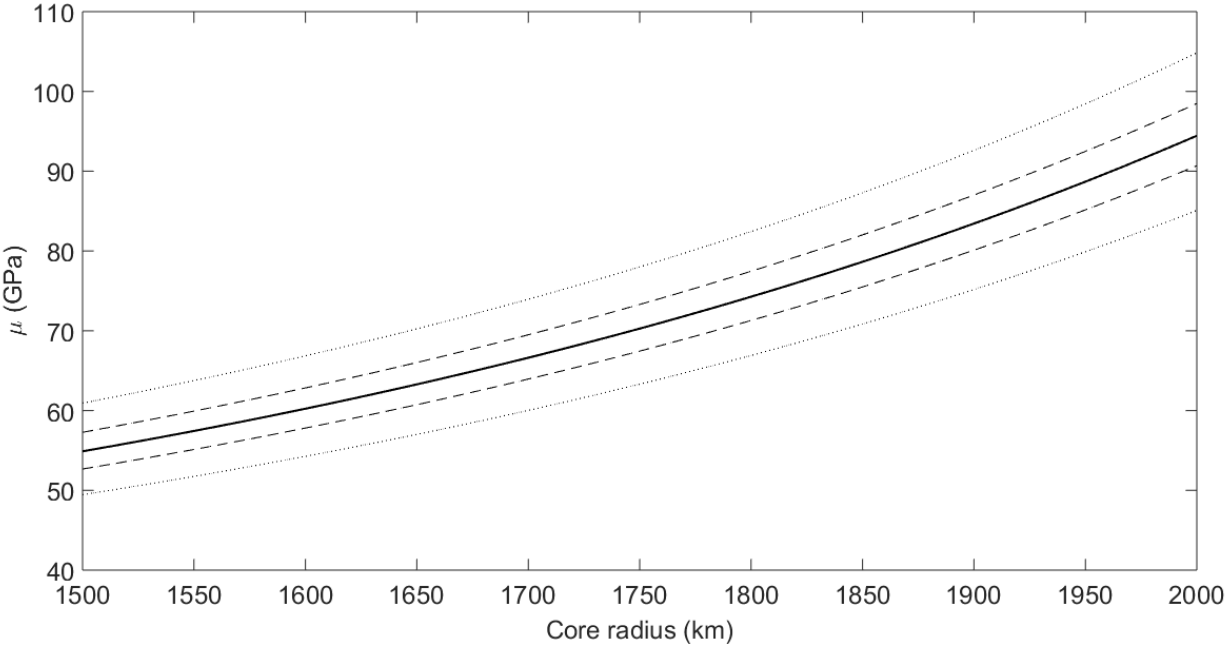

Figure A.4: The tradeoff between mean mantle rigidity (μ) and the radius of the core implied by the measured elastic tidal Love number (k_2) of Mars, based on the parametrization of Harrison (1963). The solid line indicates combinations of parameters that correspond to $k_2 = 0.169$, the dashed lines correspond to the associated uncertainty of ±0.006 (Konopliv et al., 2016), and the dotted lines correspond to a possible 11% error bound on the calculation. The calculated values of k_2 were adjusted to account for the frequency-dependence of spacecraft observations (Appendix A.5).

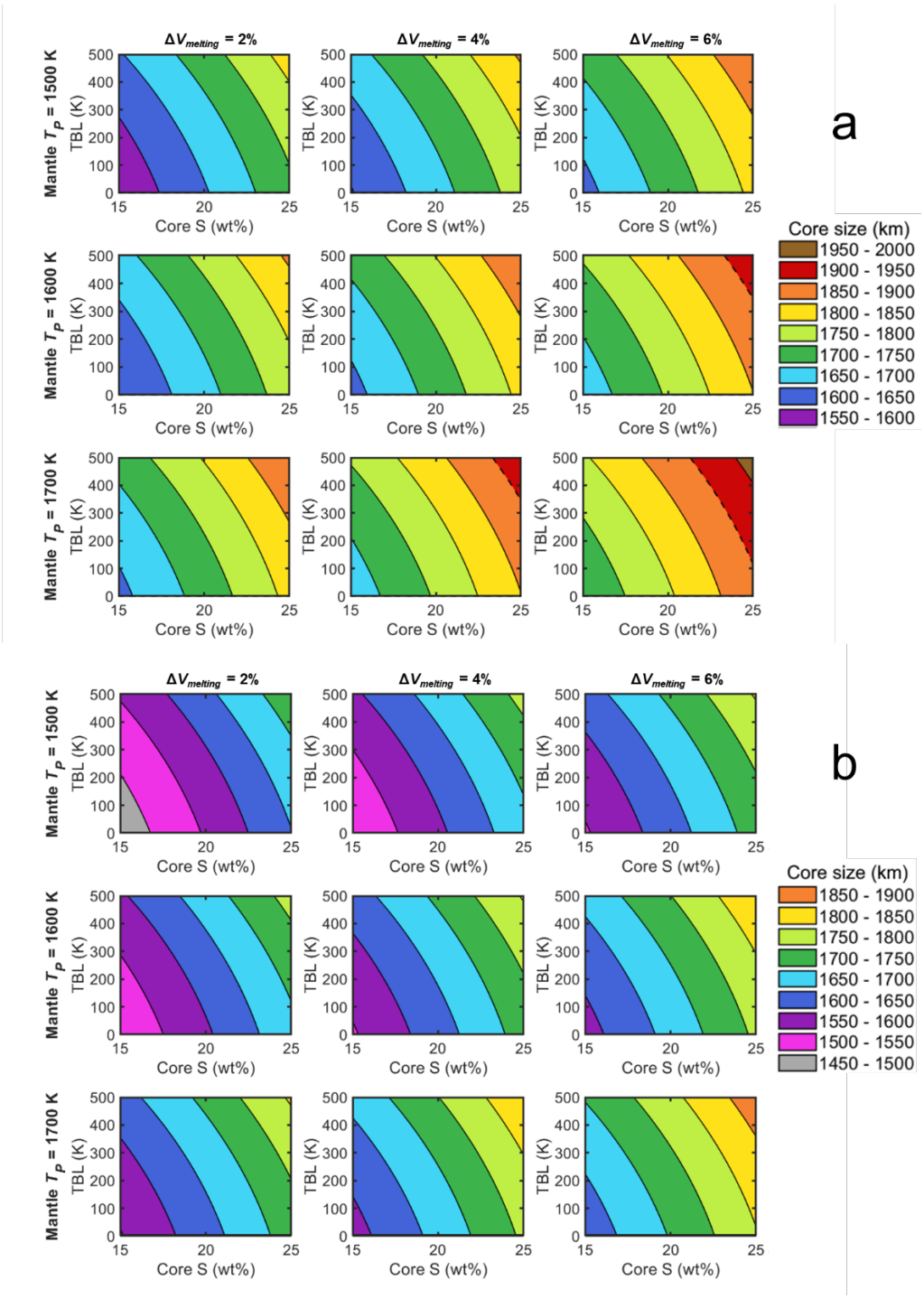

Figure A.5: Tradeoffs between parameters that influence core size for fixed crustal thicknesses of 85 km (**a**) and 25 km (**b**). Thicker crusts necessitate larger core radii to match the bulk properties of the planet. For a crustal thickness of 85 km, the measured MOI constrains core size to be >1900 km, indicated by the dotted line. For a crustal thickness of 25 km, the measured MOI constrains core size to be <1400 km, below the range of this plot. Also see Figure 2.8.

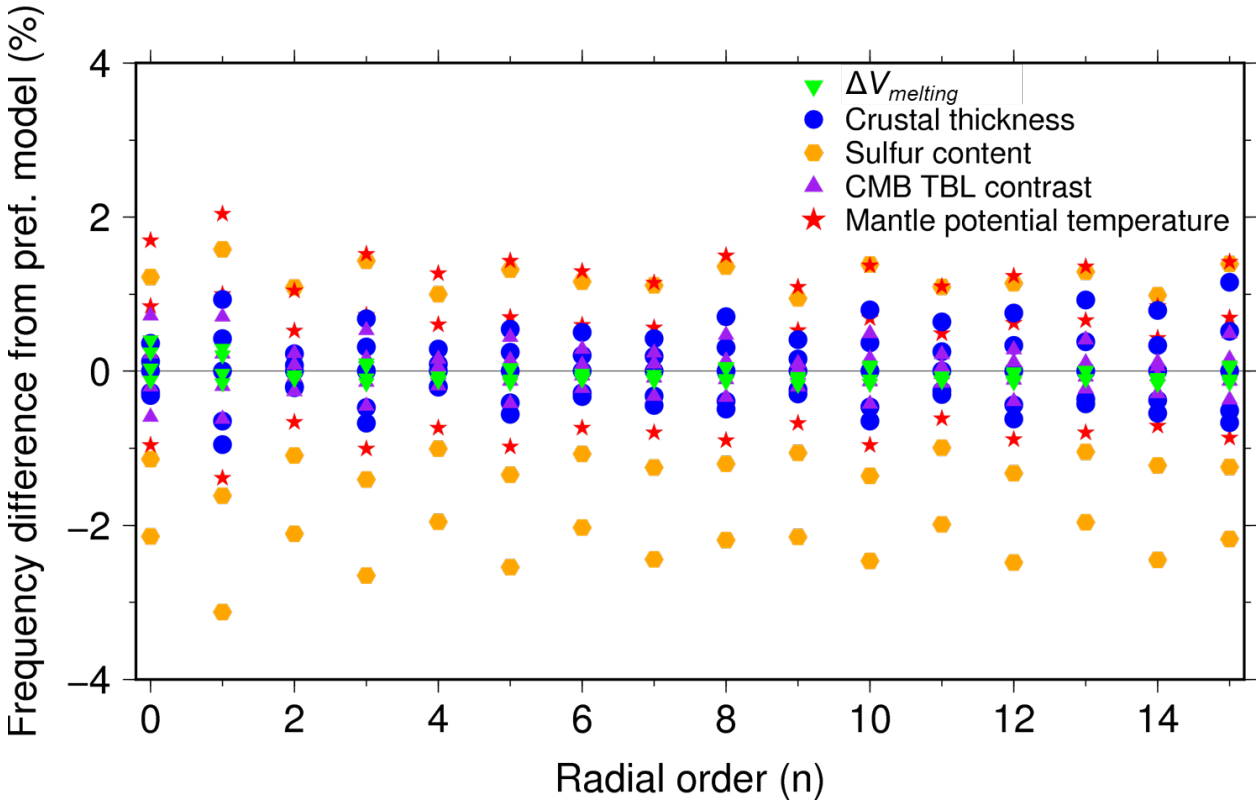

Figure A.6: Detailed variation of the change in radial mode frequency as each of the five parameters described in Section 4.4 is varied. All frequencies are shown relative to the prediction for core S of 18 wt%, crustal thickness of 50 km, TBL temperature contrast of 300 K, mantle potential temperature of 1600 K, and $\Delta V_{melting}$ = ~3%, as in Figure 2.5.

A.9 Supplementary Tables

Table A.1: Metal–silicate partitioning parameterizations

		valence	a	b	c	d
Siebert et al. (2011)						
	Ni	+2	0.35 (±0.07)	2934 (±279)	–83 (±17)	0
	Co	+2	0.2 (±0.03)	1892 (±238)	–66 (±8)	0
	Mn	+2	0.53 (±0.04)	–6356 (±418)	46 (±10)	0
	V	+3	–0.46 (±0.06)	–5964 (±513)	–19 (±14)	–0.063 (±0.026)
	Cr	+2	0.26 (±0.06)	–3318 (±495)	13 (±14)	–0.056 (±0.025)
	P	+5	2.03 (±0.17)	–2698 (± 1062)	99 (±42)	–0.71 (±0.05)
	W	+4	1.96 (±0.14)	–937 (±741)	–55 (±35)	–0.57 (±0.04)
Corgne et al. (2008)						
	Ti	+4	3.46	–19000	–42 (±52)	–0.11 (±0.16)
Fischer et al. (2015)						
	Si	+4	1.3 (±0.3)	–13500 (±900)	0	–
	O	–2	0.6 (±0.4)	–3800 (±900)	22 (±14)	–
Rose-Weston et al. (2009)						
	S	–2	4.37	13686	217.49	–
Boujibar et al. (2014)						
	S	–2	–	405 (±150)	136 (±25)	32 (±5.5)
			e	**f**	**g**	**h**
			181 (±45)	305 (±380)	30.2 (±6)	1.13 (±0.14)
			i	**j**	**k**	
			10.7 (±2.5)	31.4 (±18)	–3.72 (0.07)	

Partitioning coefficients used in this study (Equation A.5) and their associated 2σ uncertainties. Each listed study parameterized partitioning using a different functional form, described in Appendix A.2. The S parameterization of Rose-Weston et al. (2009) was used for the primordial differentiation step, while the parameterization of Boujibar et al. (2014) was used for all subsequent steps.

Table A.2: Martian mantle and core compositions

		This study	Taylor (2013)	Sanloup (1999)	Lodders & Fegley (1996)	Wänke & Dreibus (1988)
Mantle						
SiO_2	wt%	43.8 (44.1, 43.6)	43.7 (±1.0)	51.0	45.39	44.4
MgO	wt%	30.2 (30.5, 30.1)	30.5 (±0.05)	27.3	29.71	30.2
FeO	wt%	18.2 (18.4, 17.6)	18.1 (±1.0)	17.7	17.22	17.9
Al_2O_3	wt%	3.03 (3.06, 3.03)	3.04 (±0.1)	2.5	2.89	3.02
CaO	wt%	2.44 (2.46, 2.43)	2.43 (±0.01)	2.0	2.35	2.45
Na_2O	wt%	0.673 (0.678, 0.671)	0.53 (±0.1)	1.2	0.98	0.50
MnO	wt%	0.471 (0.475, 0.469)	0.44 (±0.06)	0.4	0.37	0.46
P_2O_3	wt%	0.125 (0.236, 0.045)	0.15 (±0.47)	–	0.17	0.13
TiO_2	wt%	0.143 (0.147, 0.141)	0.14 (±0.01)	–	0.14	0.14
Cr_2O_3	wt%	0.712 (0.721, 0.699)	0.73 (±0.04)	0.7	0.68	0.76
K_2O	ppm	662 (670, 660)	400 (±20)	–	1100	656
Ni	ppm	440 (585, 320)	330 (±109)	–	–	400
S	ppm	523 (755, 373)	–	–	–	–
Co	ppm	116 (138, 76.5)	71 (±25)	–	–	68
V	ppb	114 (119, 111)	–	–	–	–
W	ppb	46.7 (75.5, 24.6)	74 (±31)	–	–	105
Core						
Fe	wt%	73.9 (74.3, 73.6)	71.6*	76.6	79.5	77.8
S	wt%	18.4 (18.6, 17.9)	21.4	16.2	10.6	14.24
Ni	wt%	7.00 (7.10, 6.85)	7*	7.2	7.67	7.6
O	wt%	0.12 (0.35, 0.04)	–	–	–	–
Co	wt%	0.300 (0.305, 0.288)	–	–	0.38	0.36
Si	ppm	1.82 (5.06, 0.672)	–	–	–	–
W	ppm	4.68 (5.44, 3.71)	–	–	–	–

Table A.2 (Continued)

Comparison of the bulk silicate Mars and core compositions between this and previous studies. The compositional uncertainties for this study are reported as 95% confidence intervals, while the uncertainties of Taylor (2013) are ±2σ. The core composition of Taylor (2013) is reported in terms of Fe+Ni, which we have separated here assuming a nominal Ni value.

Table A.3: Martian bulk planetary compositions

		Taylor (2013)	Sanloup (1999)	Lodders and Fegley (1996)	Wänke and Dreibus (1988)
O	wt%	34.9	32.5	33.75	33.1
Fe	wt%	26.7	28.5	27.24	27.7
Si	wt%	15.3	17.0	16.83	16.2
Mg	wt%	13.6	12.6	14.16	14.3
S	wt%	4.02	3.8	2.2	4.64
Ni	wt%	1.56	1.7	1.58	1.68
Ca	wt%	1.30	1.1	1.33	1.37
Al	wt%	1.20	1.0	1.21	1.25
Cr	wt%	0.375	0.35	0.368	0.407
Na	wt%	0.374	0.67	0.577	0.290
Mn	wt%	0.274	0.23	0.225	0.279
P	wt%	0.141	–	0.11	0.0979
Co	ppm	734	–	795	532
Ti	ppm	643	600	650	657
K	ppm	411	–	730	265
V	ppm	78.1	–	77	–
W	ppm	0.137	–	0. 16	0. 0822

Comparison of Martian bulk (crust + mantle + core) compositions implied by previous studies. The composition of Taylor (2013) was calculated based on the stated relative abundances of volatile and refractory elements. The composition of Wänke and Dreibus (1988) was calculated based on the reported bulk silicate Mars composition, core composition, and core mass fraction.

Appendix B
Supplemental Material for Chapter 3

B.1 Note on Mars' Hf/W Ratio

The Martian mantle (i.e., Shergottite source) $f^{Hf/W}$ used in this study (2.0 ± 0.4, Table B.4) is different than the value (~3.4) reported by Foley et al. (2005) and Dauphas & Pourmand (2011) and used in some models of Martian Hf–W evolution (e.g., Morishima et al., 2013). We use the $f^{Hf/W}$ of Kleine & Walker (2017), which agrees with the value reported by Jacobsen (2005) and is the most recent published estimate. The difference between these values is not due to discrepancies in Martian meteorite measurements; in fact, the Kleine & Walker (2017) value derives from the bulk $(Hf/W)_{Mars}$ of Dauphas & Pourmand (2011). Rather, the difference arises from the $\left(^{180}Hf/^{184}W\right)_{CHUR}$ value used (Equation 3.2). Dauphas & Pourmand (2011) use a CHUR composition defined as a Mars-like mixture of meteoritic sources (Lodders & Fegley, 1997), rather than a CI-like value as in Kleine & Walker (2017) or Nimmo & Kleine (2007). Since the distinction is in a constant reference ratio, the actual implied timescale of accretion is identical for either value of $f^{Hf/W}$. A body that differentiated at some time after CAI will reach a fixed final ε_{182W} regardless of which $f^{Hf/W}$ is used because the implied initial $\left(^{182}W/^{180}Hf\right)_{mantle}$ is the same in each case.

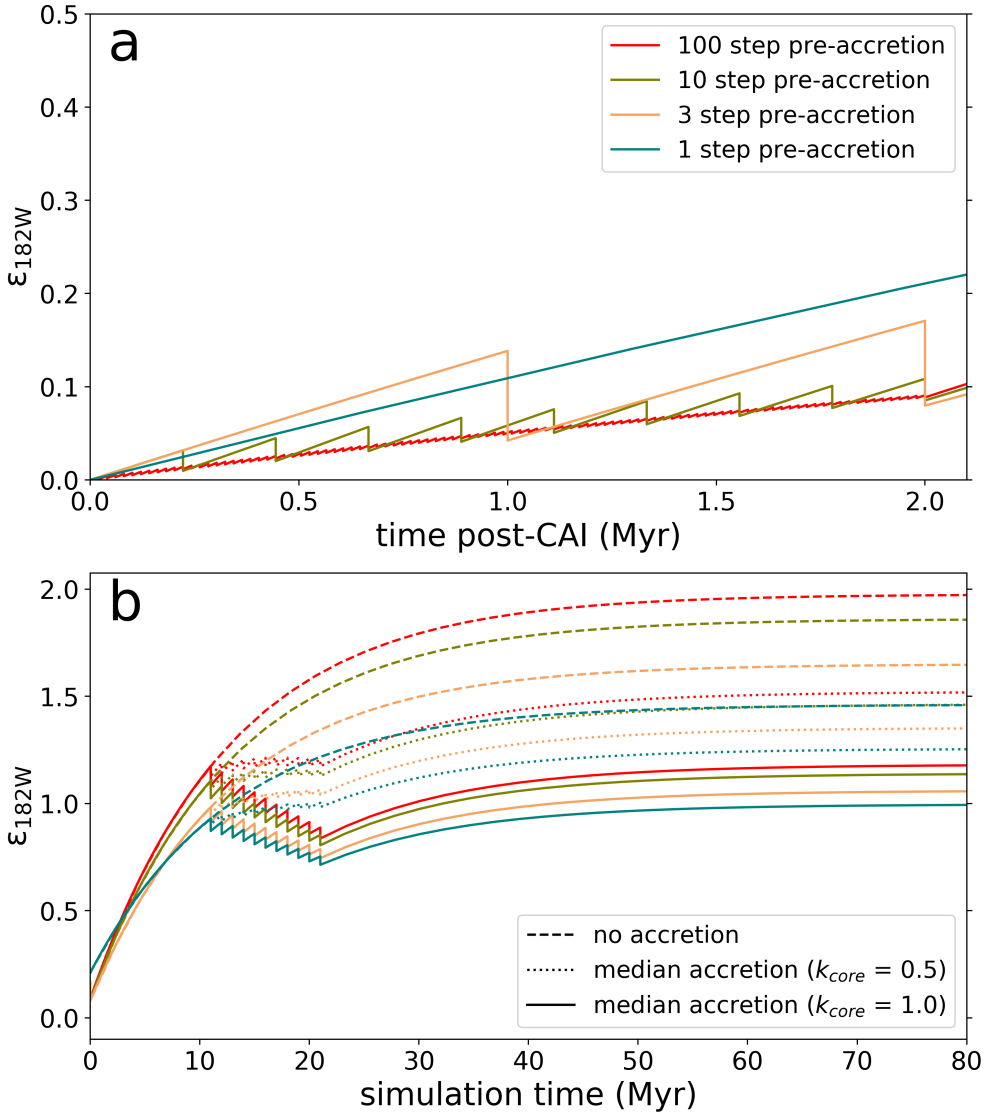

Figure B.1: Effect of "pre-accretion" (i.e., oligarchic growth before the *N*-body simulation begins) shown by the evolution of a single embryo with variable prescribed pre-accretion history. Pre-accretion (**a**) consists of homogenous growth steps (k_{core} = 1.0) evenly distributed over the 2 Myr period between CAI condensation and the start of the *N*-body simulation. The effect of increasing the number of steps becomes negligible beyond 100 steps. At later times (**b**), the embryo experiences either no accretion (dashed curves) or a synthetic accretion history based on the median of the Mars analogs (11 planetesimal impactors, 95% mass reached 18 Myr after simulation start; Table B.3) with k_{core} = 0.5 (dotted curves) or k_{core} = 1.0 (solid curves). The maximum possible effect of pre-accretion is ~0.5 ε units, and the effect is substantially smaller for most analogs.

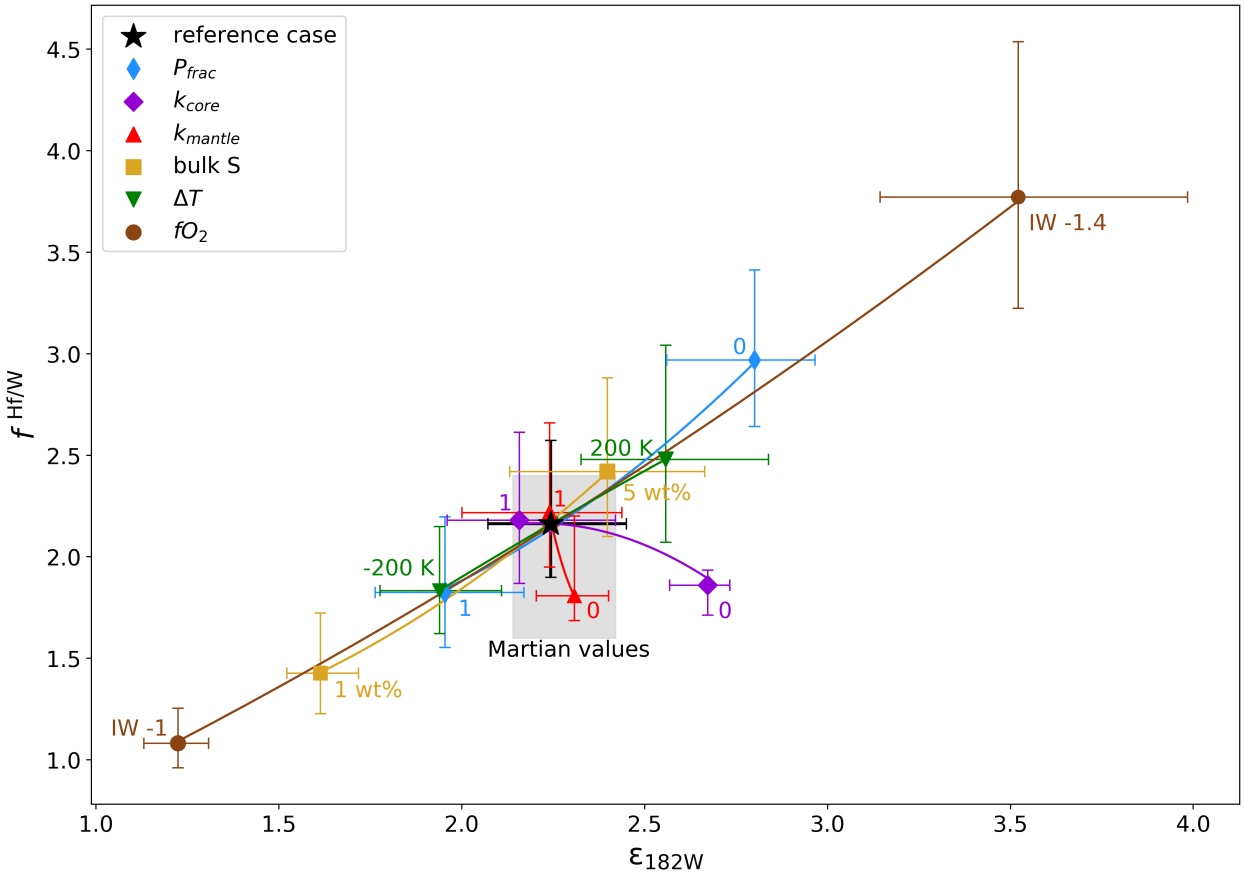

Figure B.2: Alternate version of Figure 3.4 using the W metal–silicate partitioning parameterization of Siebert et al. (2011) (Table B.2). Here, the "reference case" parameters are P_{frac} = 0.6, k_{core} = 0.85, k_{mantle} = 0.4, S = 3.5 wt%, ΔT = 0 K, and fO_2 = IW–1.22. Contrasted with the Jennings et al. (2021) parameterization, this version has generally more siderophile W, a decreased sensitivity to ΔT, an inverted effect of P_{frac}, and a larger k_{core} effect on ε_{182W}. The shaded grey region indicates the uncertainty range of measured Martian Shergotty-source values. Symbols denote the median of all analogs and error bars indicate interquartile ranges.

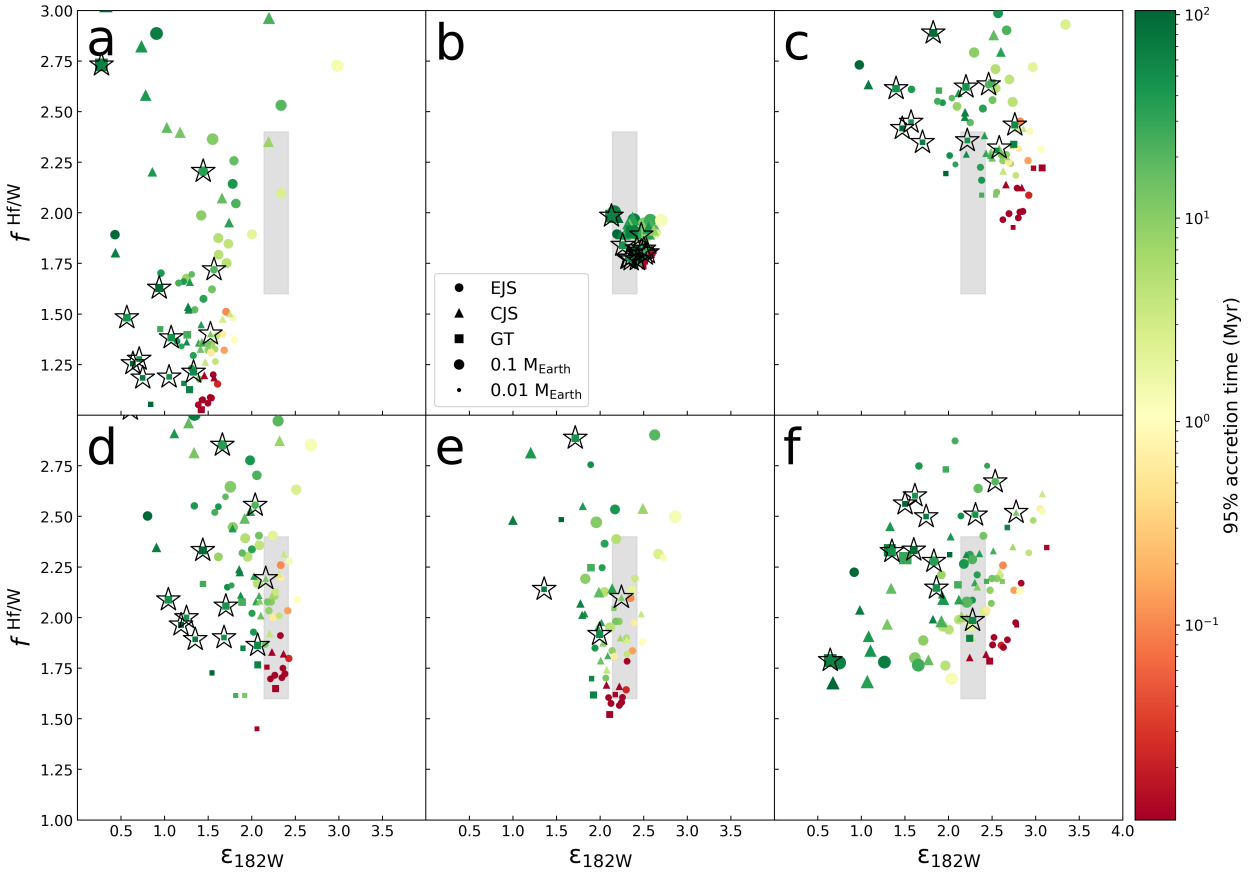

Figure B.3: Alternate version of Figure 3.5 with relaxed parameter constraints. Symbol color indicates 95% accretion time, and symbol size is proportional to mass. Stars indicate analogs with "Mars-like" orbits (Figure 3.1). Shaded grey region indicates the uncertainty range of measured Martian Shergotty-source values (Table B.4). **a.** fO_2 = IW–1.2, 5.0 wt% S, k_{mantle} = 1.0, k_{core} = 1.0, P_{frac} = 1.0, ΔT = 200 K. **b.** fO_2 = IW–1.7, 1.0 wt% S, k_{mantle} = 0.1, k_{core} = 0.1, P_{frac} = 0.1, ΔT = –200 K. **c.** fO_2 = IW–1.7, 1.6 wt% S, k_{mantle} = 0.4, k_{core} = 0.85, P_{frac} = 0.4, ΔT = –200 K. **d.** fO_2 = IW–1.5, 3.5 wt% S, k_{mantle} = 0.4, k_{core} = 0.85, P_{frac} = 0.4, 5 Myr between CAI condensation and simulation start. **e.** Initial fO_2 of IW–4.0 inside 1.5 AU and IW–1.4 outside of 1.5 AU, 3.5 wt% S, k_{mantle} = 0.4, k_{core} = 0.85, P_{frac} = 0.6, ΔT = 150 K. **f.** Reference case conditions calculated with Siebert et al. (2011) coefficients (i.e., Figure B.2): fO_2 = IW–1.22, 3.5 wt% S, k_{mantle} = 0.4, k_{core} = 0.85, P_{frac} = 0.6.

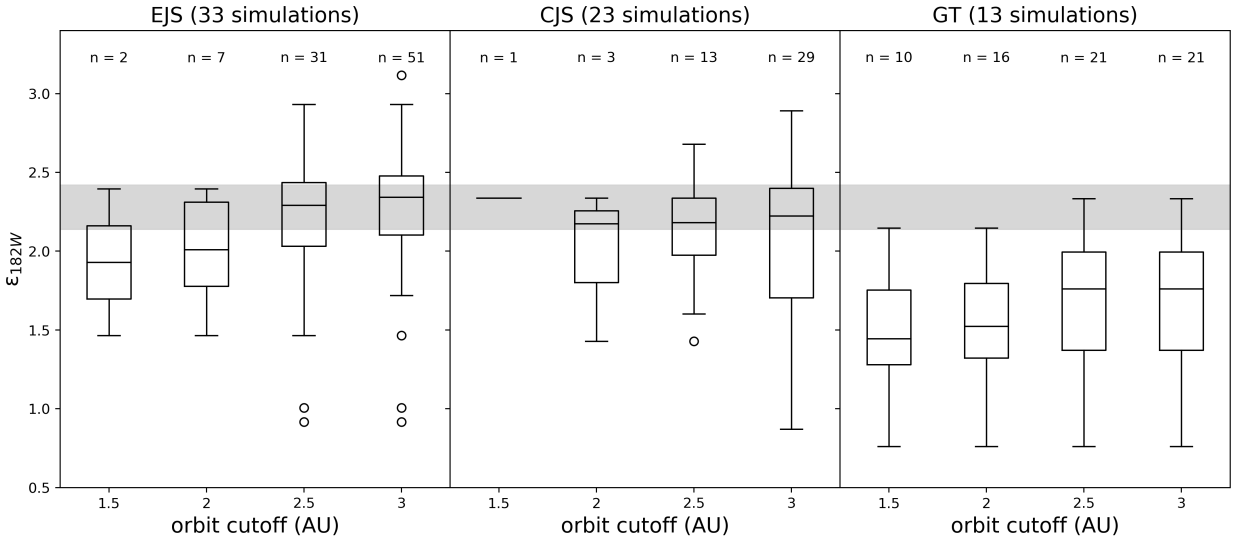

Figure B.4: Orbital distribution of final analog ^{182}W anomalies under "reference case" model conditions (Figure 3.5a; fO_2 = IW–1.47, 3.5 wt% S, k_{mantle} = 0.4, k_{core} = 0.85, P_{frac} = 0.6). The shaded band indicates the measured Martian value with uncertainty (Table B.4). As in Figure 3.2, there does not appear to be a strong relationship between a body's final orbit and its final ε_{182W}. This implies that accretion history is independent of final analog orbit. For example, if analogs with more distant orbits took substantially longer to accrete, there would be a negative correlation between orbit cutoff and ε_{182W}.

B.3 Supplementary Tables

Table B.1: Modelled Martian geochemistry

element	abundance (wt%)	geochemistry
Fe	43.78	partitioned (D_{Fe})
Si	25.10	perfectly lithophile
Mg	22.38	perfectly lithophile
Ni	2.56	partitioned (D_{Fe})
Ca	2.61	perfectly lithophile
Al	2.40	perfectly lithophile
Na	1.16	perfectly lithophile
Hf	3.06×10^{-5}	perfectly lithophile
W	2.75×10^{-5}	partitioned (D_W)
S	variable (1.0–5.0)	perfectly siderophile
C	variable (0.0–0.2)	perfectly siderophile

Bulk Mars composition used in this study. Compositions are from Palme & O'Neill (2014) and are based on a CI chondrite with oxygen and the highly volatile elements removed. Bulk S was varied in the range 1–5 wt% and compositions were renormalized to 100 wt% for each analog. Bulk C was fixed at 0 wt% except in one instance (Section 3.3). Note that Si is unlikely to be "perfectly lithophile" in planets larger or more reducing than Mars (e.g., Lin et al., 2002; Georg et al., 2007).

Table B.2: Comparison of W partitioning parameterizations

parameter	Jennings et al. (2021)	Siebert et al. (2011)	Wade et al. (2012)
a	0.61(28)	1.96(14)	1.80(24)
b	–4091(670)	–937(741)	–6728
c	0	–55(35)	–77
d	0	–0.57(4)	0
n	6+	4+	6+

Metal–silicate partitioning parameters for W (Equation 3.5) from various studies with reported uncertainties. Major disagreements include the interpreted valence state (n), whether the pressure term (c) is statistically meaningful, and whether to parameterize melt composition with an $\frac{nbo}{t}$ term (d). We use the Jennings et al. (2021) values in our analysis. Compare Figure 3.4 with Figure B.2 for an example of how the choice of partitioning parameters can influence the analogs' calculated Hf–W signatures.

Table B.3: Properties of all Mars analogs

analog ID	mass (M_{Earth})	ecc.	SMA (AU)	prov. (AU)	t_{50} (Myr)	t_{95} (Myr)	# p.	# e.	$f^{Hf/W}$	ε_{182W}
EJS3:65	0.0593	0.229	2.33	2.75	0	8.66	9	0	2.02	2.34
EJS7:55	0.1060	0.148	2.24	1.95	0.19	42.86	25	1	2.82	2.41
EJS8:63	0.1150	0.149	2.85	2.39	0.25	2.54	17	1	2.74	3.12
EJS9:52	0.0489	0.348	1.73	1.83	0	48.50	11	0	2.06	1.81
EJS9:64	0.0521	0.159	2.94	2.68	0	0	2	0	1.74	2.34
EJS10:67	0.0670	0.209	2.68	2.89	0	0.10	13	0	2.24	2.57
EJS11:61	0.1080	0.135	1.91	2.17	5.15	5.15	10	1	2.49	2.33
EJS16:51	0.0471	0.555	2.27	1.83	0	6.21	10	0	2.02	2.44
EJS16:63	0.0549	0.098	2.53	2.54	0	42.68	6	0	1.92	2.10
EJS18:49	0.1770	0.020	2.03	1.77	1.36	69.40	13	3	3.29	1.72
EJS18:53	0.0608	0.005	1.00	1.66	0	40.82	22	0	2.43	1.47
EJS21:53	0.1470	0.099	2.39	2.26	0.19	10.78	9	2	2.85	2.23
EJS22:52	0.0499	0.174	2.85	1.88	0	0.63	12	0	2.10	2.54
EJS23:62	0.0497	0.261	2.22	2.51	0	0.00	2	0	1.72	2.43
EJS23:65	0.0613	0.101	2.57	2.69	0	3.54	10	0	2.10	2.46
EJS24:65	0.0684	0.290	2.32	2.57	0	14.10	17	0	2.36	2.30
EJS25:56	0.0555	0.066	2.24	2.05	0	1.30	14	0	2.20	2.68
EJS26:54	0.1080	0.106	1.55	1.75	2.81	35.04	29	1	2.90	2.01
EJS26:60	0.0485	0.061	2.52	2.35	0	0	3	0	1.75	2.46
EJS26:61	0.0486	0.096	2.11	2.38	0	0	2	0	1.71	2.27
EJS26:64	0.0591	0.129	2.55	2.61	0	10.07	9	0	2.06	2.39
EJS26:65	0.0593	0.144	2.14	2.75	0	0.14	8	0	2.02	2.60
EJS27:67	0.0690	0.051	2.07	2.79	0	34.30	16	0	2.31	2.19
EJS28:63	0.1010	0.072	2.24	2.17	3.02	4.90	7	1	2.39	2.31
EJS28:64	0.1790	0.256	2.39	2.39	0.17	26.46	22	2	3.57	2.53
EJS29:51	0.0994	0.036	2.02	1.66	0.69	21.84	22	1	2.73	2.50
EJS29:66	0.1710	0.033	2.64	2.86	0.12	1.29	10	2	3.14	3.55
EJS30:61	0.0546	0.046	2.29	2.37	0	35.28	10	0	1.99	2.11
EJS31:37	0.0387	0.133	2.05	1.28	0	31.55	11	0	2.02	1.88
EJS31:64	0.0591	0.169	2.56	2.55	0	12.98	9	0	2.06	2.34
EJS33:42	0.0839	0.141	2.54	1.59	8.00	8.00	13	1	2.31	1.92
EJS34:31	0.0949	0.174	2.61	1.08	0.03	16.72	40	1	2.99	2.43
EJS35:50	0.1350	0.230	2.25	1.66	0.05	19.88	24	2	3.12	2.93
EJS35:58	0.0585	0.442	2.43	2.09	0	17.76	15	0	2.24	2.05
EJS36:35	0.0487	0.411	2.57	1.25	0	40.27	22	0	2.37	1.81
EJS37:62	0.1060	0.355	2.80	2.44	0.03	1.98	10	1	2.50	2.72
EJS38:67	0.1020	0.018	2.67	2.35	0	4.28	9	1	2.44	2.47
EJS39:53	0.0983	0.137	2.25	1.51	11.29	189.28	19	1	2.54	0.92
EJS39:58	0.0494	0.118	2.22	2.19	0	0	18	0	1.88	2.46
EJS40:61	0.0516	0.196	2.28	2.41	0	12.06	5	0	1.85	2.25
EJS40:68	0.0583	0.133	2.70	3.04	0	0.02	3	0	1.83	2.56
EJS42:68	0.0623	0.334	1.15	3.00	0	0.59	7	0	2.01	2.40
EJS43:67	0.0629	0.050	2.89	2.94	0	1.11	9	0	2.08	2.75
EJS44:27	0.0469	0.160	2.64	0.93	0	17.89	24	0	2.41	1.92
EJS44:57	0.0645	0.123	1.54	2.01	0	20.93	22	0	2.46	2.29
EJS44:69	0.1150	0.203	2.44	2.84	0	9.62	10	1	2.57	2.11
EJS46:65	0.0533	0.274	2.72	2.75	0	0	2	0	1.75	2.48
EJS48:45	0.0537	0.274	1.97	1.46	0	24.52	21	0	2.37	1.74

Table B.3 (Continued)

analog ID	mass (M_{Earth})	ecc.	SMA (AU)	prov. (AU)	t_{50} (Myr)	t_{95} (Myr)	# p.	# e.	$f^{Hf/W}$	ε_{182W}
EJS48:68	0.1100	0.151	2.99	2.74	0	4.75	2	1	2.30	2.47
EJS50:45	0.1990	0.696	2.47	1.39	19.62	63.81	32	1	4.09	1.01
EJS50:55	0.0485	0.863	2.36	2.01	0	4.05	8	0	1.95	2.47
CJS4:24	0.1310	0.326	2.43	1.51	5.07	16.76	35	2	3.08	1.60
CJS5:72	0.0642	0.448	2.89	3.48	0	0	3	0	1.88	2.33
CJS7:58	0.0534	0.203	2.84	2.22	0	6.84	10	0	2.05	2.40
CJS7:65	0.0603	0.555	1.54	2.68	0	29.90	9	0	2.06	2.17
CJS8:57	0.1040	0.212	2.23	2.11	0.68	34.18	15	1	2.60	2.40
CJS8:66	0.0616	0.101	2.53	2.82	0	9.89	9	0	2.07	2.23
CJS8:70	0.0652	0.110	2.16	3.20	0	14.21	7	0	2.03	2.22
CJS9:51	0.1620	0.251	2.82	1.92	0.01	22.32	35	2	3.58	2.74
CJS10:71	0.0647	0.023	2.61	3.33	0	3.67	5	0	1.96	2.32
CJS11:53	0.0508	0.122	1.47	1.97	0	11.94	12	0	2.11	2.34
CJS11:58	0.1010	0.305	2.66	1.98	24.82	69.62	11	1	2.42	1.00
CJS11:71	0.0627	0.135	2.87	3.34	0	0.00	3	0	1.87	2.49
CJS12:45	0.1020	0.192	2.65	1.40	12.50	40.68	34	1	2.91	1.33
CJS12:66	0.0707	0.495	2.10	2.71	0	40.10	18	0	2.40	1.95
CJS13:71	0.1260	0.078	2.86	3.10	3.17	16.74	9	1	2.66	2.31
CJS16:67	0.0660	0.664	2.48	2.87	0.00	2.73	13	0	2.20	2.52
CJS18:50	0.1580	0.075	2.03	1.81	0.10	41.77	45	2	3.73	2.68
CJS18:63	0.0609	0.244	2.34	2.55	0	36.04	12	0	2.16	2.18
CJS19:68	0.1690	0.034	1.94	2.22	8.84	42.00	20	2	3.30	1.43
CJS21:60	0.0555	0.224	2.29	2.29	0	49.75	10	0	2.06	1.98
CJS23:72	0.0733	0.331	2.27	3.30	0	55.45	12	0	2.25	1.98
CJS28:53	0.0538	0.147	2.88	1.94	0	3.46	15	0	2.21	2.62
CJS30:76	0.1970	0.108	2.67	3.06	12.01	35.20	24	2	3.83	1.62
CJS31:59	0.0545	0.316	2.31	2.25	0	24.10	10	0	2.06	2.23
CJS32:65	0.1280	0.217	2.98	2.65	0.31	7.76	23	1	3.02	2.89
CJS37:40	0.1400	0.382	2.77	1.58	8.47	12.00	21	2	2.98	1.70
CJS40:69	0.1940	0.214	2.88	2.42	19.60	175.43	16	2	3.45	0.87
CJS48:76	0.0791	0.459	2.79	3.82	0	62.47	11	0	2.27	1.97
CJS49:73	0.1470	0.137	2.83	2.88	18.96	40.88	26	1	3.24	1.32
GT1:38	0.0543	0.115	2.14	2.81	0	62.64	6	0	1.79	2.12
GT2:26	0.0567	0.030	1.46	1.89	0	55.91	6	0	1.87	2.15
GT2:38	0.0518	0.160	2.17	2.86	0	0	5	0	1.68	2.33
GT5:40	0.0617	0.117	1.43	2.76	0	44.47	7	0	2.05	1.76
GT6:10	0.1634	0.027	1.01	1.45	0.35	28.79	63	0	4.14	1.81
GT7:30	0.0697	0.043	1.41	2.17	0	94.99	13	0	2.30	1.52
GT8:30	0.0620	0.287	1.68	2.20	0	24.32	18	0	2.07	1.99
GT9:43	0.0332	0.073	1.89	1.82	0	57.59	15	0	1.76	1.97
GT9:74	0.0359	0.045	1.47	2.53	0	110.90	5	0	1.86	1.18
GT10:18	0.1586	0.048	1.26	1.45	0.82	63.91	61	1	4.06	1.37
GT10:41	0.0283	0.195	2.01	1.67	0	11.35	3	0	1.56	1.91
GT10:43	0.0310	0.466	2.18	1.80	0	0.01	4	0	1.68	2.25
GT11:33	0.0257	0.235	2.06	1.45	0	0.00	1	0	1.41	2.01
GT11:37	0.0624	0.042	1.52	1.72	0.06	44.89	9	1	2.05	1.14
GT12:24	0.0413	0.111	1.79	1.47	0	26.47	10	0	2.04	1.53
GT12:33	0.0283	0.251	1.88	1.57	0	24.02	3	0	1.56	1.79

Table B.3 (Continued)

analog ID	mass (M_{Earth})	ecc.	SMA (AU)	prov. (AU)	t_{50} (Myr)	t_{95} (Myr)	# p.	# e.	$f^{Hf/W}$	ε_{182W}
GT14:15	0.1741	0.069	1.49	1.53	43.99	63.80	24	2	3.31	0.76
GT14:69	0.0307	0.030	1.74	2.49	0	117.00	2	0	1.65	1.51
GT15:45	0.0338	0.033	1.41	1.85	0	72.49	7	0	1.79	1.34
GT16:50	0.0339	0.082	1.48	2.01	0	48.89	8	0	1.80	1.73
GT16:52	0.0364	0.073	1.45	1.98	0	45.03	16	0	1.89	1.26

Values of analog mass, eccentricity (ecc.), semi-major axis (SMA), and Hf–W values are given at the end of the *N*-body simulation. Provenance (prov.) is the mass-weighted average of the initial semi-major axes of the analog's building blocks. Times are given in simulation time (starting 2 Myr after CAI formation), with t_{50} and t_{95} being the times at which the analog reached 50% and 95% of its final mass, respectively (a value of 0 indicates that the threshold was reached before the start of the simulation). Counts of accreted bodies only include planetesimals (# p.) and embryos (# e.) that impacted the analog itself, and do not include the seed embryo or any bodies that had previously impacted its impactors. Hf–W evolution was calculated at "reference case" conditions (Figure 3.5a; fO_2 = IW–1.47, 3.5 wt% S, k_{mantle} = 0.4, k_{core} = 0.85, P_{frac} = 0.6).

Table B.4: Values used for the Hf–W isotopic calculations.

Parameter	Value	Source
$\left({}^{180}\mathrm{Hf}/{}_{184}\mathrm{W}\right)_{CHUR}$	1.35 ± 0.11	Kleine & Walker (2017)
$t_{1/2}$ of ^{182}Hf	8.9 ± 0.1 Myr	Kleine & Walker (2017)
t_{CAI}	4.567 Ga	MacPherson (2014)
$\left({}^{182}\mathrm{Hf}/{}_{180}\mathrm{Hf}\right)_{inital}$	$(1.018 \pm 0.043) \times 10^{-4}$	Kruijer et al. (2014)
$\left({}^{182}\mathrm{W}/{}_{184}\mathrm{W}\right)_{inital}$	0.865 ± 0.001	Kruijer et al. (2014)
$\left({}^{184}\mathrm{W}/{}_{\mathrm{W}}\right)_{modern}$	0.3064 ± 0.0002	IUPAC (2003)
$\left({}^{180}\mathrm{Hf}/{}_{\mathrm{Hf}}\right)_{modern}$	0.3508 ± 0.0016	IUPAC (2003)
Martian mantle $f^{\mathrm{Hf/W}}$	2.0 ± 0.4	Kleine & Walker (2017)
Martian mantle $\varepsilon_{182\mathrm{W}}$ (relative to terrestrial)	0.37 ± 0.04	Kruijer et al. (2017)
CHUR $\varepsilon_{182\mathrm{W}}$ (relative to terrestrial)	–1.9 ± 0.1	Kleine & Walker (2017)

Formulations of $\varepsilon_{182\mathrm{W}}$ and $f^{\mathrm{Hf/W}}$ are given in Equations 3.1 and 3.2, respectively. In this study, we compare our analogs to $\varepsilon_{182\mathrm{W}}$ of the Martian mantle relative to the chondritic reservoir CHUR (2.27 ± 0.14), which is equal to the difference between the Martian mantle $\varepsilon_{182\mathrm{W}}$ and CHUR $\varepsilon_{182\mathrm{W}}$ values listed here.

Appendix C
Supplemental Material for Chapter 4

C.1 Equations for Figure 4.6

The following equations were used to calculate the alloy properties plotted in Figure 4.6. All equations are functions of differential stress τ and are modified from Gleason & Mao (2013), Reaman et al. (2011), and references therein. Parameter values are listed in Table C.2.

Dislocation velocity: $$v = \left(\frac{V_D a' b L}{w^2}\right) \exp\left(\frac{-\Delta H_0}{kT}\right) \sinh\left(\Delta H_0 - \frac{\Delta H}{kT}\right) \quad \text{(C.1)}$$

Activation enthalpy: $$\Delta H = \Delta H_0 \left[1 - \left(\frac{\tau_p}{\tau}\right)^{3/4}\right]^{4/3} \quad \text{(C.2)}$$

Strain rate: $$\dot{\epsilon} = bv\left(\frac{\tau}{G_0 b}\right)^2 \quad \text{(C.3)}$$

Critical grain size: $$d = \sqrt{\frac{A_{Dif}}{A_{Dis}} \frac{V}{b} \frac{k}{R} \ln\left(\frac{\alpha G}{2S\tau}\right) \left(\frac{G}{\tau}\right)^n} \quad \text{(C.4)}$$

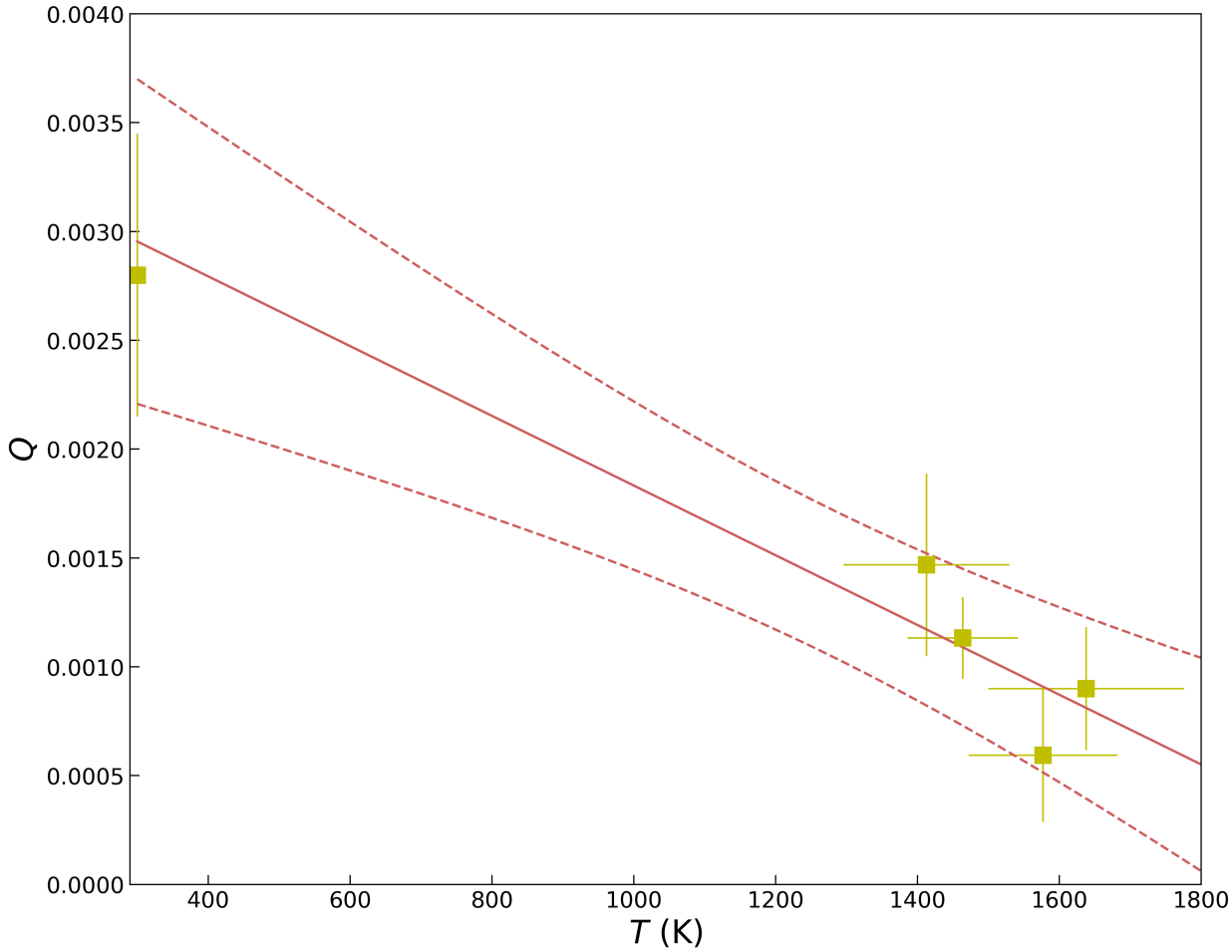

Figure C.1: Observed change in Q upon laser heating of Fe–5Si. The 300 K point (upper left) was calculated from the Fe–5Si fit (Figure 4.3). High temperature data are from consecutive diffraction images collected at approximately the same pressure (43–46 GPa; see Figure 4.2). The solid line is a fit to $^{\partial Q}/_{\partial T}$, calculated by orthogonal distance regression considering the error bars of each point. The dashed lines are 95% confidence intervals.

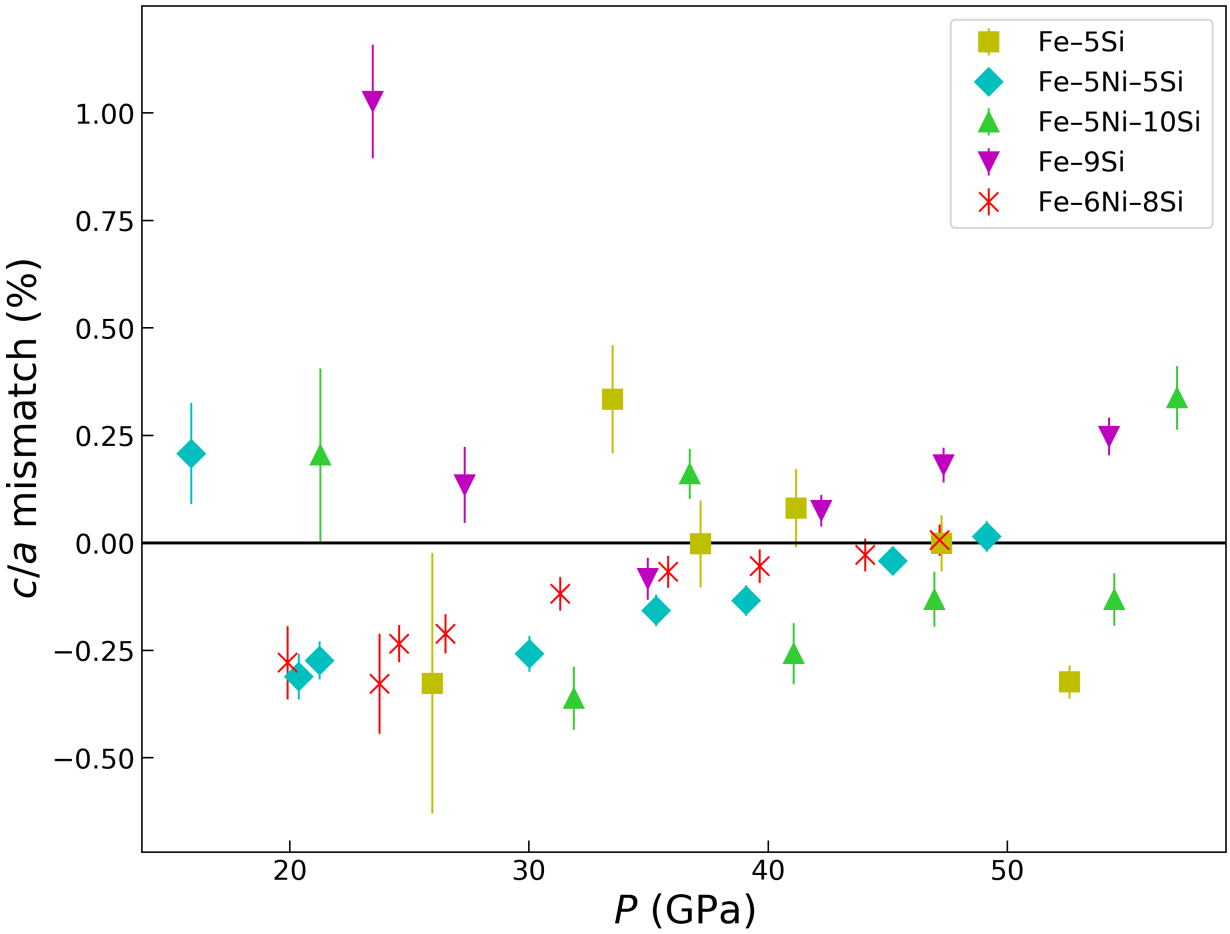

Figure C.2: Comparison between our experimentally determined ratio of hcp alloy unit cell parameters (i.e., the ratios of c-axis lengths to a-axis lengths) and the ratio calculated using the parametrization of Fischer & Campbell (2015). 'Mismatch' here is defined as $\left(\frac{\text{measured } c/a - \text{calculated } c/a}{\text{calculated } c/a}\right) \times 100\%$. Despite the nonhydrostatic conditions of our radial diffraction experiments, the measured and calculated unit cell ratios agree quite well at 300 K.

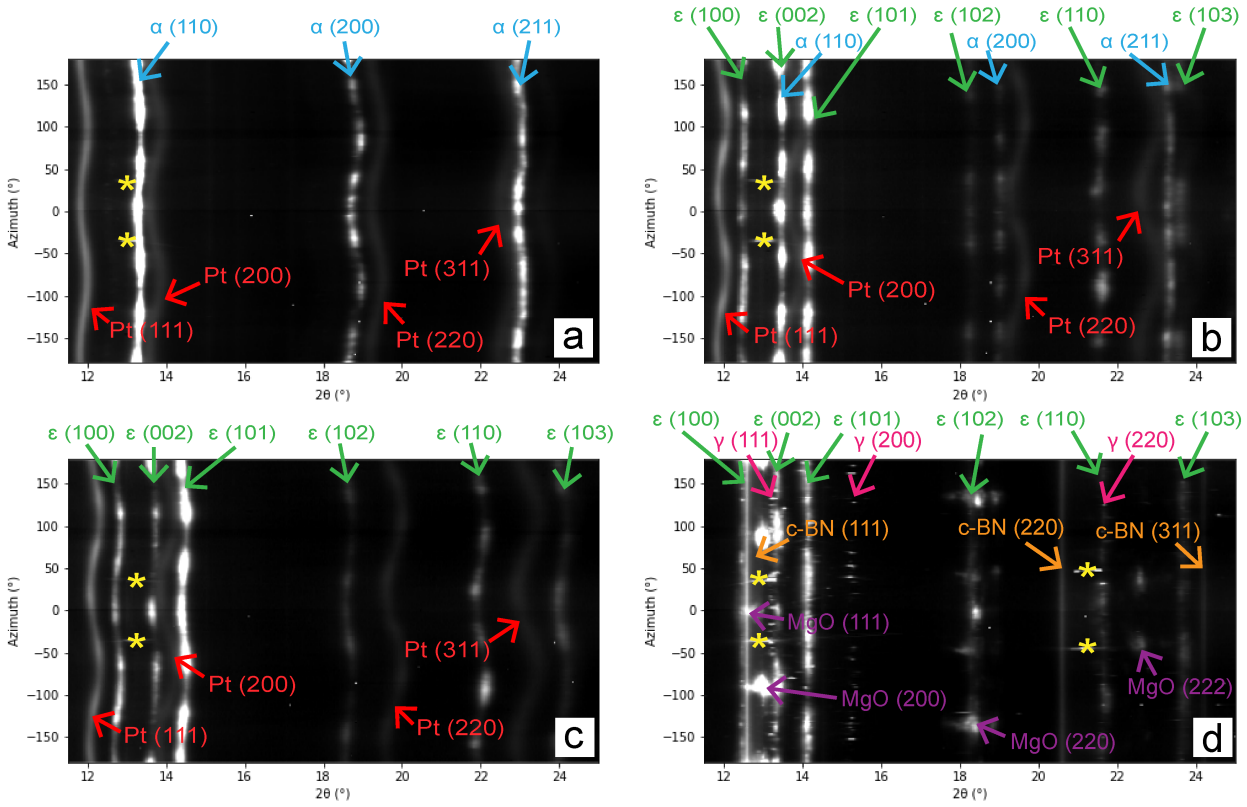

Figure C.3: Selection of caked diffraction images from our radial X-ray diffraction experiments shown in the range $11.5^\circ < 2\theta < 25^\circ$. Labels above each panel indicate sample diffraction (**α:** bcc, **γ:** fcc, **ε:** hcp) and labels within each panel indicate diffraction from pressure standards and gasket materials. **a:** Fe–5Ni–5Si at 6.5 GPa (bcc only). **b:** Fe–5Ni–5Si at 16 GPa (bcc + hcp). **c:** Fe–5Ni–5Si at 30 GPa (hcp only). **d:** Fe–5Ni–5Si at 43 GPa and 1580 K (hcp + fcc). Yellow asterisks indicate single-crystal diffraction spots from the diamond anvils, which were removed before refinement. Sinusoidal distortions of diffraction rings indicate elastic deformation and intensity variations within rings indicate plastic deformation (i.e., texturing).

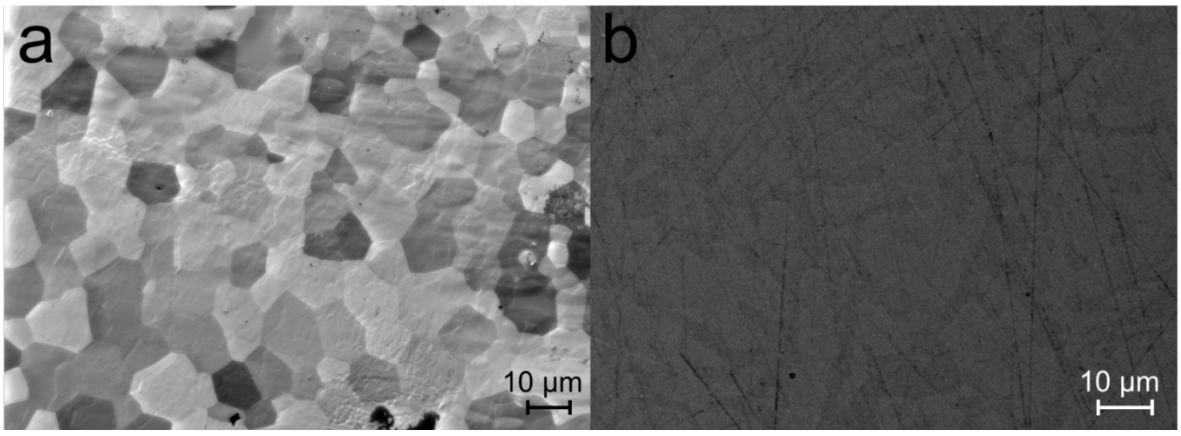

Figure C.4: Scanning electron microscope images of two starting materials at ambient conditions, the Fe–5Ni–5Si foil (**a**) and the Fe–6Ni–8Si alloy chunk (**b**). The left image was taken during focused ion beam exposure, which improved the visibility of individual grains due to the differential ion channeling across grain orientations.

C.3 Supplementary Tables

Table C.1: Data from XRD experiments

composition	phases	T (K)	P (GPa)	hcp c (Å)	hcp a (Å)	Q
Fe–5Si	bcc	300	12.6(35)	-	-	-
Fe–5Si	bcc + hcp	300	19.9(36)	3.9538(11)	2.454(4)	0.00151(16)
Fe–5Si	bcc + hcp	300	23.7(26)	3.9425(8)	2.449(9)	0.00153(10)
Fe–5Si	hcp	300	24.6(29)	3.9345(5)	2.442(2)	0.00222(6)
Fe–5Si	hcp	300	26.5(39)	3.9229(6)	2.435(2)	0.00278(7)
Fe–5Si	hcp	300	31.3(26)	3.9074(5)	2.425(2)	0.00299(5)
Fe–5Si	hcp	300	35.8(24)	3.8881(5)	2.413(2)	0.00321(5)
Fe–5Si	hcp	300	39.6(29)	3.8645(5)	2.399(2)	0.00334(6)
Fe–5Si	hcp	300	44.0(56)	3.8551(5)	2.393(2)	0.00315(6)
Fe–5Si	hcp	300	47.1(29)	3.8472(4)	2.388(2)	0.00315(5)
Fe–5Si	hcp*	300	45.4(26)	3.8486(4)	2.389(2)	0.00303(5)
Fe–5Si	hcp*	300	44.3(20)	3.8533(4)	2.392(2)	0.00261(5)
Fe–5Si	hcp*	300	38.0(46)	3.8592(4)	2.396(5)	0.00222(5)
Fe–5Si	hcp*	300	35.5(38)	3.8722(4)	2.404(2)	0.00247(4)
Fe–5Ni–5Si	bcc	300	6.5(14)	-	-	-
Fe–5Ni–5Si	bcc + hcp	300	15.9(14)	3.9812(16)	2.456(5)	0.00194(27)
Fe–5Ni–5Si	bcc + hcp	300	20.4(19)	3.9445(7)	2.448(2)	0.00240(7)
Fe–5Ni–5Si	hcp	300	21.2(24)	3.9295(6)	2.439(2)	0.00302(6)
Fe–5Ni–5Si	hcp	300	30.0(10)	3.9108(5)	2.428(2)	0.00327(7)
Fe–5Ni–5Si	hcp	300	35.3(14)	3.8880(5)	2.413(2)	0.00329(6)
Fe–5Ni–5Si	hcp	300	39.1(14)	3.8722(4)	2.404(2)	0.00354(5)
Fe–5Ni–5Si	hcp	300	45.2(14)	3.8514(4)	2.390(1)	0.00361(5)
Fe–5Ni–5Si	hcp	300	49.1(34)	3.8333(4)	2.379(2)	0.00360(5)
Fe–5Ni–5Si	hcp*	300	48.7(17)	3.8330(9)	2.380(3)	0.00284(10)
Fe–5Ni–5Si	hcp*	300	48.1(14)	3.8356(5)	2.382(2)	0.00206(6)
Fe–5Ni–5Si	hcp*	300	39.7(7)	3.8592(12)	2.397(3)	0.00198(6)
Fe–5Ni–10Si	bcc	300	11.7(40)	-	-	-
Fe–5Ni–10Si	bcc + hcp	300	25.9(34)	3.9249(44)	2.432(10)	0.00143(33)
Fe–5Ni–10Si	bcc + hcp	300	33.5(12)	3.9155(17)	2.412(5)	0.00158(22)
Fe–5Ni–10Si	hcp	300	37.2(12)	3.8821(13)	2.401(4)	0.00236(14)
Fe–5Ni–10Si	hcp	300	41.2(13)	3.8708(12)	2.393(4)	0.00278(14)
Fe–5Ni–10Si	hcp	300	47.2(18)	3.8514(8)	2.384(3)	0.00320(13)
Fe–5Ni–10Si	hcp	300	52.6(18)	3.8271(5)	2.377(2)	0.00346(10)
Fe–5Ni–10Si	hcp*	300	50.5(15)	3.8449(7)	2.376(2)	0.00276(10)
Fe–5Ni–10Si	hcp*	300	47.1(43)	3.8577(7)	2.385(3)	0.00166(9)
Fe–5Ni–10Si	hcp*	300	40.7(45)	3.8783(3)	2.399(9)	0.00172(10)
Fe–6Ni–8Si	bcc	300	6.8(14)	-	-	-
Fe–6Ni–8Si	bcc + hcp	300	21.3(12)	3.9693(29)	2.449(7)	0.00292(27)
Fe–6Ni–8Si	bcc + hcp	300	31.9(13)	3.9154(10)	2.432(3)	0.00331(12)

Table C.1 (Continued)

composition	phases	*T* (K)	*P* (GPa)	hcp *c* (Å)	hcp *a* (Å)	*Q*
Fe–6Ni–8Si	hcp	300	41.0(15)	3.8917(9)	2.416(3)	0.00447(20)
Fe–6Ni–8Si	hcp	300	36.7(11)	3.9169(8)	2.421(2)	0.00444(10)
Fe–6Ni–8Si	hcp	300	46.9(14)	3.8673(8)	2.400(3)	0.00505(12)
Fe–6Ni–8Si	hcp	300	54.5(16)	3.8452(8)	2.387(2)	0.00564(12)
Fe–6Ni–8Si	hcp	300	57.1(20)	3.8456(10)	2.377(3)	0.00576(11)
Fe–6Ni–8Si	hcp*	300	55.9(13)	3.8468(7)	2.382(2)	0.00533(9)
Fe–6Ni–8Si	hcp*	300	50.1(17)	3.8570(7)	2.392(2)	0.00371(9)
Fe–6Ni–8Si	hcp*	300	44.5(15)	3.8699(10)	2.400(3)	0.00348(14)
Fe–9Si	bcc	300	7.6(6)	-	-	-
Fe–9Si	bcc + hcp	300	23.5(7)	3.9800(19)	2.435(5)	0.00280(37)
Fe–9Si	bcc + hcp	300	27.3(7)	3.9336(19)	2.429(3)	0.00209(17)
Fe–9Si	hcp	300	35.0(7)	3.8934(6)	2.412(2)	0.00339(8)
Fe–9Si	hcp	300	42.2(7)	3.8714(5)	2.396(1)	0.00398(6)
Fe–9Si	hcp	300	47.3(8)	3.8555(5)	2.385(2)	0.00453(7)
Fe–9Si	hcp	300	54.2(9)	3.8334(6)	2.371(2)	0.00506(8)
Fe–9Si	hcp*	300	52.4(8)	3.8361(4)	2.374(1)	0.00385(5)
Fe–9Si	hcp*	300	48.4(20)	3.8446(21)	2.382(6)	0.00263(28)
Fe–9Si	hcp*	300	39.4(7)	3.8798(5)	2.400(1)	0.00078(9)
Fe–5Si	fcc + hcp	1577(105)	43.1(8)	3.8992(4)	2.410(4)	0.00059(31)
Fe–5Si	fcc + hcp	1638(138)	44.4(10)	3.8948(4)	2.410(8)	0.00090(28)
Fe–5Si	fcc + hcp	1412(117)	45.4(9)	3.8802(10)	2.406(4)	0.00147(42)
Fe–5Si	fcc + hcp	1463(78)	44.5(7)	3.8808(18)	2.408(6)	0.00113(19)
Fe	hcp	300	17.8(2)	3.9514(4)	2.4453(1)	0.00214(6)
Fe	hcp	300	23.7(6)	3.9342(2)	2.4358(1)	0.00220(2)
Fe	hcp	300	29.1(2)	3.9346(8)	2.4307(3)	0.00252(14)
Fe	hcp	300	31.8(8)	3.8994(3)	2.4162(1)	0.00216(8)
Fe	hcp	300	38.8(2)	3.8683(3)	2.3990(1)	0.00227(3)
Fe	hcp	300	41.9(2)	3.8319(3)	2.3827(1)	0.00277(7)
Fe	hcp	300	49.1(2)	3.8161(4)	2.3731(1)	0.00245(8)

Data from radial X-ray diffraction experiments collected at Advanced Light Source beamline 12.2.2 (Kunz et al., 2005). Asterisks indicate decompression data. Compositions are in weight percent. *Q* is the deformation of all observed sample peaks. *Q* and unit cell parameters (*a* and *c*) were determined simultaneously by Rietveld refinement (Section 4.2). Numbers in parentheses are uncertainties on the last digit(s). Pressures were calculated from the equation of state of Pt (Fei et al., 2007) at 300 K or MgO (Speziale et al., 2001) at high temperatures. Temperature measurement is described in Kunz et al. (2018).

Table C.2: Values used for inner core deformation calculations

Parameter		Value	Source
Debye frequency	V_D	13 THz	Gleason & Mao (2013)
Peierls barrier width	a'	0.2 nm	Gleason & Mao (2013)
Burgers vector	b	0.5 nm	Gleason & Mao (2013)
Kink pair width	w	20 nm	Gleason & Mao (2013)
Dislocation length	L	500 nm	Gleason & Mao (2013)
Standard activation enthalpy	ΔH_0	6 eV	Gleason & Mao (2013)
Peierls stress	τ_p	varies	This study
Aggregate shear modulus	G	varies	This study; Gleason & Mao (2013); Reagan et al. (2018)
Ambient aggregate shear modulus	G_0	varies	This study; Gleason & Mao (2013); Reagan et al. (2018)
Geometrical constant of diffusion	A_{Dif}	30	Reaman et al. (2011)
Geometrical constant of dislocation	A_{Dis}	1.8	Reaman et al. (2011)
Schmid factor constant	$\alpha/2S$	0.6	Reaman et al. (2011)
Power-law constant	n	2	Reaman et al. (2011)
Specific volume	V	varies	Dewaele et al. (2006); Fischer et al. (2014)

Parameters used in Equations C.1–C.4. We retained the values used in previous studies, except for Peierls stress, which we set equal to our recalculated strength (Figure 4.5), and specific volume, which we recalculated for the alloy compositions used (assuming that the effect of Ni is negligible).

Appendix D
Failed Projects

D.1 Melting Curves of the Martian Mantle

Planetary mantles are multi-phase systems that melt over a range of temperatures at any given pressure. The solidus is the temperature at which melting begins, and the liquidus is the temperature at which no solid remains; these temperatures are pressure-dependent, giving rise to curves that describe melting throughout a planet's interior. The locations of these curves in *P*–*T* space influence various processes of planetary evolution. There are significant disagreements between measurements of the terrestrial melting curves, but Martian mantle melting is understood even less rigorously.

We attempted to measure the melting curves of a Mars-like sample in a diamond anvil cell (DAC). The sample was prepared from a mixture of oxides to match the proposed Taylor (2013) Martian mantle composition and melted via laser levitation to produce a homogenous glass which was powdered and loaded into Re gaskets for compression. KCl was used as our pressure medium, pressure standard, and thermal insulator because of its relatively high melting point (Boehler 1996). During the experiments, the DAC was laser-heated from both sides, with temperatures determined from thermal emission. We attempted to use two complimentary melting criteria. The first criterion (Andrault et al., 2011) was the disappearance of the first solid phase diffraction peaks and the appearance of diffuse melt scattering, indicating the solidus temperature was exceeded. The same criterion in reverse (i.e., the appearance of the first solid peaks) could be applied upon cooling a fully molten sample to determine the liquidus temperature. We also tracked temperature versus laser power to look for the temperature plateau indicative of the presence of a partial melt; the end of this plateau was used by Andrault et al. (2011) as an indication of the liquidus.

The major problem we encountered arose from our choice of glassy starting material. Glasses are amorphous, and thus produce the same diffuse X-ray scattering as liquids. Therefore, each sample had to be fully crystallized in situ to produce diffraction peaks that could then be observed disappearing. In principle, this can be done by heating the sample for a while below the solidus temperature. Unfortunately, since Mars is small, its mantle pressures are below 20 GPa (Rivoldini et al., 2011). This is quite low for a laser-heated DAC experiment, and consequently the minimum temperature at which the laser would engage was already close to the solidus temperature and was highly unstable thereafter. We were unable to maintain a stable sub-solidus temperature for long enough to eliminate the starting material's diffuse scattering. The publication of Duncan et al. (2018), which extracted melting curves from multianvil experiments, made continuing this project unnecessary.

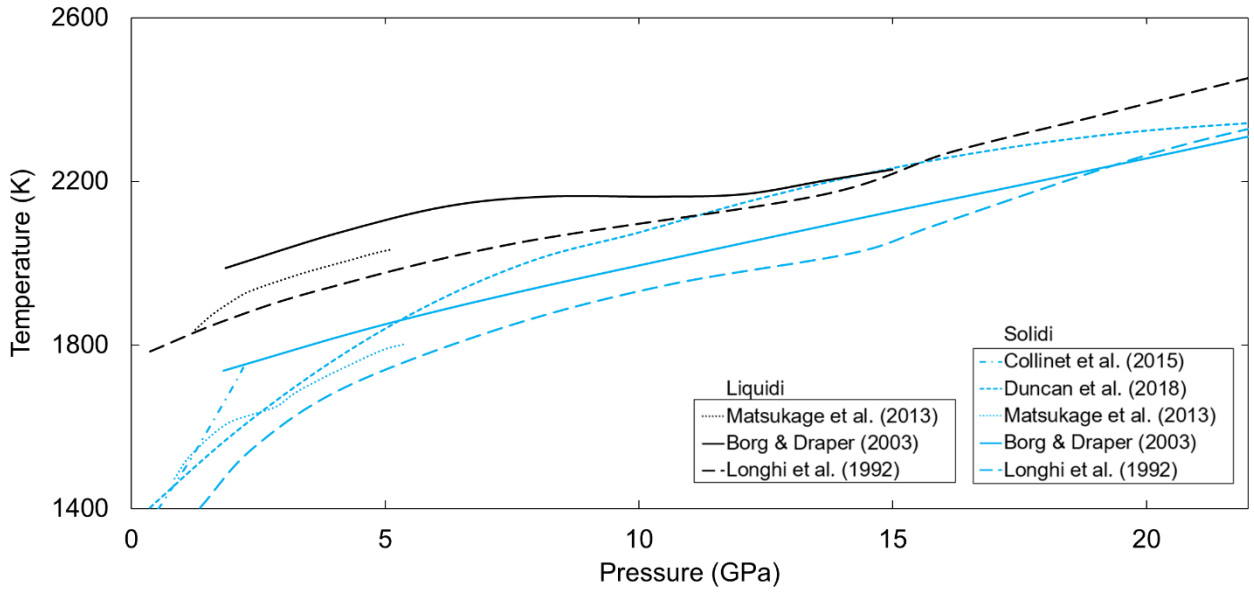

Figure D.1: Some published melting curves for the Martian mantle.

D.2 Alkali Halide Equation of State

The DAC is fundamentally a uniaxial compression device, but most DAC experiments benefit from uniform (i.e., hydrostatic or lithostatic) compression. This is achieved by filling the empty space around the sample with a "pressure medium" that will readily flow and uniformly redistribute stress in the sample chamber. These pressure media can be loaded as gases or liquids, but solids are easier to load, so alkali halide salts (which are soft, transparent, and thermally insulating) are frequently employed. Additionally, solid pressure media diffract X-rays, so a halide pressure medium can be used as simultaneously as a "pressure standard" (i.e., a substance whose unit cell parameters are used to infer the pressure of the sample as a whole) provided that its equation of state (EoS) is known. There are recent EoS measurements of the most common alkali halides: KCl (e.g., Chidester et al., 2021), KBr (e.g., Dewaele et al., 2012), NaCl (e.g., Sakai et al., 2011), and LiF (e.g., Dong et al., 2014) but these compositions may not be suitable for every experiment. Many of the most up-to-date alkali halide EoS formulations were published in the twentieth century (including Francis Birch's last research publication: Birch, 1986), so it may be worthwhile to update the parameterizations of some less-popular materials.

We investigated several alkali halides: KI, LiCl, LiBr, LiI, and NaBr. Of these, LiCl, LiBr, and LiI were too hygroscopic to load under the ambient humidity of our lab; prepared sample flakes of these materials adsorbed atmospheric moisture and dissolved within a few tens of seconds, far too quickly to load them in the DAC. The other two compositions appeared workable and were loaded along with a Pt flake, which served as a pressure standard. Samples were baked at 100°C for one hour to drive off any adsorbed water before closing the cell.

NaBr fluoresced strongly when exposed to X-rays and melted at unexpectedly low temperatures (~2000 K at 20 GPa). Additionally, we confirmed that NaBr does not undergo the standard *B1→B2* phase transition, instead transforming into a lower-symmetry structure at ~30 GPa (Sato-Sorensen, 1983; Flórez et al., 2002). On the other hand, KI made the *B1→B2* transition at <3 GPa and did not melt in our heated experiments, so we targeted it for further study. Unfortunately, a global pandemic delayed the necessary room-temperature experiments for over a year, and eventually they had to be done remotely with mailed-in samples. These samples were a mixed flake of Pt and KI gas-loaded with Ne, but in neither sample were the Ne peaks sufficiently unambiguous to confirm its presence (and thus the hydrostaticity of the sample). Since these experiments were remote, we could not reload these failed samples.

We proceeded to analyze the heated data anyway in hopes of supplementing them with a successful room-temperature experiment later. Diffraction data from 100 representative exposures were integrated with Dioptas (Prescher & Prakapenka, 2015) and exported to PeakFit (Singh et al., 1994) to determine the volumes of KI and Pt. Temperatures were determined from in situ thermal emission upon cooling and corrected for the experimental geometry to determine separate Pt and KI temperatures (Campbell et al., 2007; 2009). The Pt temperature of each experiment contributed to its pressure determination via a thermal EoS of Pt (Fei et al., 2007). These corrections revealed that our experiments' coverage of P (18–49 GPa) and T (1200–1850) were narrower than expected, limiting the utility of this dataset. Furthermore, the data did not show significant changes in the KI volume with temperature (probably because of the large volume ratio of KI to Pt), and the calculated pressure counterintuitively increased upon cooling. This latter behavior is obviously unphysical; it is possible for

sample pressures to decrease upon initial heating due to sample relaxation, but this is not a reversible process. Since calculated pressure varies with Pt volume, it is possible that a chemical reaction (i.e., between Pt and H from lingering water in the KI) is responsible for the anomalous pressures. However, to reproduce the observations, this reaction would also have to be reversible upon cooling, which is unlikely. X-ray exposure is known to alter the color of alkali halides (e.g., Seitz, 1946), so it is conceivable that the optical properties of KI radically changed during our experiments, producing the pressure discrepancy and implying that KI is unsuitable as a pressure medium. In any case, the lack of either publishable heated or room-temperature data induced us to discontinue this work.

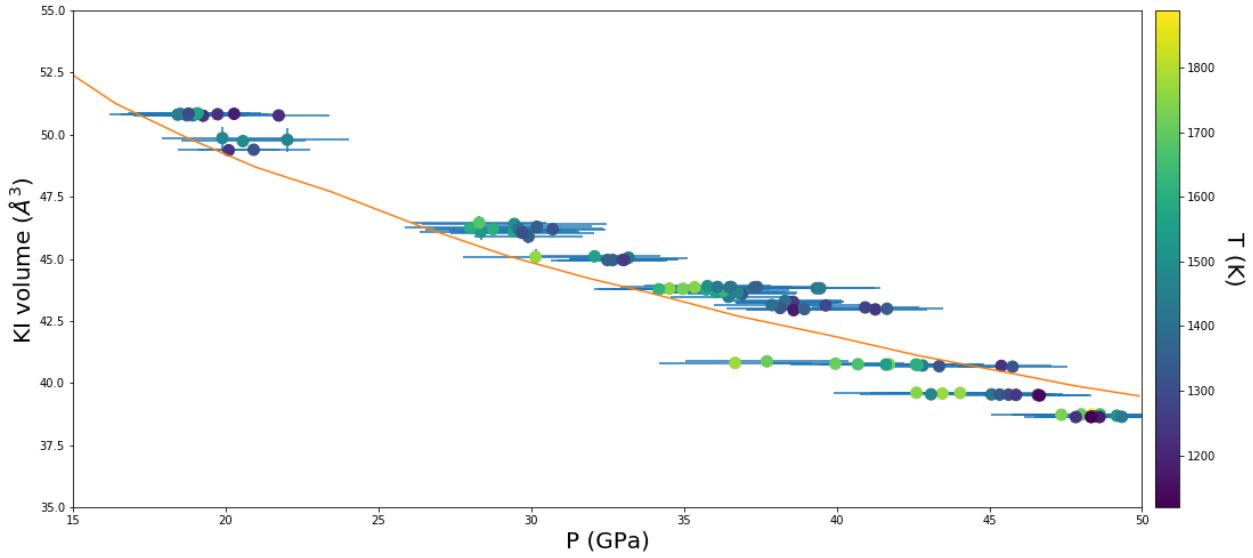

Figure D.2: Volume and pressure measurements collected on cooling. The orange line is a fit to the most recent study on the EoS of KI (Köhler et al., 1997), which collected room-temperature data up to 30 GPa. Error bars represent the standard error of each point. Note that higher temperature data are shifted to the left, the opposite effect than is expected considering thermal expansion of the sample materials. This phenomenon proved robust across several rounds of data reanalysis.

D.3 Fe–Si Deformation at Higher Pressures and Temperatures

The experiments described in Chapter 4 were intended to include additional radial diffraction measurements of Si-bearing alloys at higher pressures. These would have spanned 100–120 GPa and helped reduce the uncertainty of extrapolating Q to Earth's inner core pressure (Section 4.4.2). We attempted these experiments with the room-temperature methodology described in Section 4.2, save that we used beveled diamond anvils with a culet size of 100 μm and beryllium (Be) gaskets drilled with 25 μm sample chambers. In room temperature radial experiments, samples must be located by their X-ray absorption contrast compared to the gasket material, and we were unable to locate the alloy sample or pressure standard in any of these experiments. This could have been due to the small sample chamber volume; Be produces more diffraction peaks than the gasket materials used in other experiments, and these could have obscured the sample in the absence of strong diffraction. Be is, to our knowledge, necessary for megabar radial diffraction, as it is the only gasket material that is both X-ray transparent and will not break down at very high pressures. However, the size of the sample can be increased to some extent, so these experiments remain a target for further study.

We performed numerous experiments to characterize the effect of temperature on the strength and deformation textures of Si-bearing alloys, of which only one experiment produced data of sufficient quality to include in Chapter 4 (Figure 4.2, Figure C.1). Several experiments failed because the laser would not couple with the sample material, despite coupling well to the gasket surrounding the sample chamber. This is very unusual since the sample was an opaque metal insulated by MgO flakes, but it is possible that the insulation failed across multiple experiments, allowing heat

to be removed by the thermally conductive anvils. This issue could be ameliorated by using sintered single crystal sheets of MgO or Al_2O_3 as insulators instead of pressed powders, or by using a smaller sample flake less likely to make thermal contact with the anvils. However, even successfully heated experiments displayed issues such as appearance of unknown diffraction peaks (possibly due to MgO–sample reactions) and crystallization of excess fcc-structured sample (Section 4.3), preventing them from proceeding to Reitveld refinement. Additional quality heated experiments would greatly improve the extrapolation of Q to high temperatures (Section 4.4.2). For example, we used a simple temperature parameterization (Figure C.1) that implies a fixed linear correlation between temperature and Q, and this is unlikely to prove robust for all compositions across thousands of kelvins.

Appendix E
Suggestions for Further Research

E.1 Early Mars

E.1.1 Martian Core Formation

InSight's recent seismic observations of the Martian interior have set up something of a paradox regarding the composition of Mars' core. On the one hand, seismological studies (Stähler et al., 2021; Khan et al., 2022) confidently support the large core radii (>1800 km) predicted by the most modern pre-InSight geophysical models (e.g., Khan et al., 2018; Plesa et al., 2018). This consensus implies a low-density (~6 g/cm^3) core containing a substantial portion of light elements. On the other hand, evidence from cosmochemistry and mineral physics suggests that such a large light element inventory may be unlikely. As mentioned in Section 2.4.7, an 1800 km core likely requires >20 wt% S, which would imply a bulk Mars equivalent to or exceeding the most S-rich chondrites. S may not be solely responsible for the core's low density, but metal–silicate partitioning experiments have raised substantial objections to all the other reasonable light elements (Section 2.3.2).

Assuming the geophysical consensus on Mars' core radius is final, there may be cosmochemical solutions; perhaps it can be shown that Mars retained unexpected quantities of primordial S and C (e.g., Tian et al., 2021), or that radiogenic heating resulted in core formation at elevated temperatures (e.g., Sahijpal & Bhatia, 2015), which would enhance the siderophilic tendencies of O and H. Alternatively, our knowledge of the metal–silicate partitioning trends may be incomplete. Simultaneous partitioning of several light elements at Mars-relevant conditions may demonstrate compositional effects that support multiple alloying light elements; the antipathy of C for S-rich metallic melts has only been shown in one study (Tsuno et al., 2018), for example. Finally, as Figure 2.7 demonstrates, the physical properties of Fe–S melts are

still poorly constrained. It is conceivable that future experiments will show that Martian core density can be achieved with a lower S content than expected.

E.1.2 Timing and Dynamics of Martian Accretion

There is more work to be done involving the coupling of planetary accretion simulations with chemical constraints available from meteorites and terrestrial bodies. There are a wide variety of recent accretionary simulations incorporating variant dynamical regimes (e.g., Matsumura et al., 2017), early solar system dynamics (Clement et al., 2021; Okamura & Kobayashi, 2021), and nonidealities in the chaotic growth epoch (Cambioni et al., 2021). A reasonable accretionary history can be distinguished based on whether it can produce both Earth and Mars analogs with respectively appropriate masses and oxygen fugacities (fO_2). This method might also help evaluate reasonable fO_2 distributions in the disk, though there is unlikely to be a unique combination of dynamical history and fO_2 distribution which explains the terrestrial planets. One general consideration for modeling bulk planetary fO_2 is the effect of siderophile oxygen. Any O atoms which partition into the metal during core formation do not create oxides, meaning that the bulk fO_2 derived from mantle FeO would underestimate the total O present in the planet (Rubie et al., 2011).

The Hf–W constraints on the timing of Martian formation (Chapter 3) can be improved by incorporating the complementary Sm–Nd system. While the parent and daughter nuclides of Hf–W differ in metal–silicate affinity, the difference in Sm–Nd is in affinity for silicate melt versus silicate crystals. This makes the system sensitive to the timing of mantle solidification, a particularly interesting property on Mars since there are at least two isotopically distinct mantle reservoirs, the older of which has a solidification date only ~30 Myr after Solar System formation (Harper et al., 1995). The

simplest approach would be to interpret any accretionary impact as an instance of mantle remelting and homogenization, constraining Mars' growth to occur entirely before this solidification date. However, given that planetesimal impactors are unlikely to completely melt the mantle, modelling the evolution of the Sm–Nd signature in consecutively-generated melt ponds may offer a new perspective on the isotopic heterogeneity of Mars. The Sm–Nd signature has been previously interpreted to reflect a very long-lived magma ocean (Debaille et al., 2007), while other studies have proposed an extremely short-lived magma ocean (Bouvier et al., 2018); modelling approaches may help discriminate between these cases.

E.2 Properties of hcp Fe Alloys

Future geodynamical or tomographic research may narrow the acceptable range of inner core stresses and grain sizes (Figure 4.6). Until then, hcp Fe alloys have a wealth of under-characterized properties which may be of interest. Most obviously, since Chapter 4 represents the first texture and strength measurements of an Fe alloy with a light element, the effects of non-Si light elements (H, C, O, S) are not yet known. Even within the Si-bearing system, further experiments with varying Si contents might find compositional trends which we could not observe in our data (Figure 4.3). We did not characterize grain size, Si site occupancy, or deformation-driven migration of alloying elements either. These measurements are difficult in a non-quenchable phase like hcp Fe, but there are some studies on interstitial elements in hcp Fe (e.g., Somers et al., 1997; Vaks & Khromov, 2008; Gomi et al., 2018) and rapidly decompressing high-pressure samples (i.e., Smith et al., 2015) may make ex situ characterization useful. For deformation textures, application of viscoplastic self-consistent (VPSC) modelling could help refine interpretations of texturing mechanisms (e.g., Merkel et al., 2021).

Furthermore, as noted in Section D.3, our extrapolation of the Fe–Ni–Si Q values to inner core conditions could be improved. The deformation textures of hcp Fe were previously observed to reach a maximum around 50 GPa (Wenk et al., 2000). This could correspond to a nonlinearity in deformation strength which may only be perceptible with dense Q vs P data coverage extending to higher pressures than the ~60 GPa we obtained (Figure 4.3). Similarly, the Q vs T effect is likely nonlinear considering the well-known nonlinear temperature effects on deformation rates (e.g., Weertman, 1970). It may be useful to define the Q evolution with respect to homologous temperature using measured Fe–Si melting data (e.g., Fischer et al., 2013). The IXS versus NRIX discrepancy in literature measurements of shear modulus (Figure 4.4) also deserves a closer look. There may be unconsidered differences between experimental techniques (e.g., frequency corrections) which explain the difference in apparent Si effect. Si has a very small effect on the bulk modulus of Fe (Lin et al., 2003), and a similarly negligible effect on shear modulus would enhance the relative importance of any strengthening effects in determining inner core deformation style (i.e., Equation 4.3).

References

Ahrens, Thomas J., W. W. Anderson, and Thomas J. Ahrens. 1994. “An Equation of State for Liquid Iron and Implications for the Earth’s Core.” *Journal of Geophysical Research* 99 (B3): 4273–84. https://doi.org/10.1029/93JB03158.

Albarède, Francis. 2009. “Volatile Accretion History of the Terrestrial Planets and Dynamic Implications.” *Nature* 461 (7268): 1227–33. https://doi.org/10.1038/nature08477.

Alboussière, Thierry, Renaud Deguen, and Mickaël Melzani. 2010. “Melting-Induced Stratification above the Earth’s Inner Core Due to Convective Translation.” *Nature* 466 (7307): 744–47. https://doi.org/10.1038/nature09257.

Anderson, Don L. 1972. “Internal Constitution of Mars.” *Journal of Geophysical Research* 77 (5): 789–95. https://doi.org/10.1038/234089a0.

Anderson, O. L. 1965. “Determination and Some Uses of Isotropic Elastic Constants of Polycrystalline Aggregates Using Single-Crystal Data.” In *Physical Acoustics*, 3:43–95. Academic Press. https://doi.org/10.1016/B978-0-12-395669-9.50009-6.

Andrault, Denis, Nathalie Bolfan-Casanova, Giacomo Lo Nigro, Mohamed A. Bouhifd, Gaston Garbarino, and Mohamed Mezouar. 2011. “Solidus and Liquidus Profiles of Chondritic Mantle: Implication for Melting of the Earth across Its History.” *Earth and Planetary Science Letters* 304 (1–2): 251–59. https://doi.org/10.1016/j.epsl.2011.02.006.

Antonangeli, Daniele, Sébastien Merkel, and Daniel L. Farber. 2006. “Elastic Anisotropy in Hcp Metals at High Pressure and the Sound Wave Anisotropy of the Earth’s Inner Core.” *Geophysical Research Letters* 33 (24): L24303. https://doi.org/10.1029/2006GL028237.

Antonangeli, Daniele, Guillaume Morard, Luigi Paolasini, Gaston Garbarino, Caitlin A. Murphy, Eric Edmund, Frédéric Decremps, et al. 2018. “Sound Velocities and Density Measurements of Solid Hcp-Fe and Hcp-Fe–Si (9 Wt.%) Alloy at High Pressure: Constraints on the Si Abundance in the Earth’s Inner Core.” *Earth and Planetary Science Letters* 482 (January): 446–53. https://doi.org/10.1016/j.epsl.2017.11.043.

Antonangeli, Daniele, Florent Occelli, Herwig Requardt, James Badro, Guillaume Fiquet, and Michael Krisch. 2004. “Elastic Anisotropy in Textured Hcp-Iron to 112 GPa from Sound Wave Propagation Measurements.” *Earth and Planetary Science Letters* 225 (1–2): 243–51. https://doi.org/10.1016/j.epsl.2004.06.004.

Aubert, Julien, Hagay Amit, Gauthier Hulot, and Peter Olson. 2008. “Thermochemical Flows Couple the Earth’s Inner Core Growth to Mantle Heterogeneity.” *Nature* 454 (7205): 758–61. https://doi.org/10.1038/nature07109.

Balog, P. S., R. A. Secco, D. C. Rubie, and D. J. Frost. 2003. “Equation of State of Liquid Fe-10 Wt % S: Implications for the Metallic Cores of Planetary Bodies.” *Journal of Geophysical Research: Solid Earth* 108 (B2). https://doi.org/10.1029/2001jb001646.

Banerdt, W. Bruce, Suzanne E. Smrekar, Don Banfield, Domenico Giardini, Matthew Golombek, Catherine L. Johnson, Philippe Lognonné, et al. 2020. “Initial Results from the InSight Mission on Mars.” *Nature Geoscience* 13 (3): 183–89. https://doi.org/10.1038/s41561-020-0544-y.

Bergman, Michael I. 1998. “Estimates of the Earth’s Inner Core Grain Size.” *Geophysical Research Letters* 25 (10): 1593–96. https://doi.org/10.1029/98GL01239.

Bergman, Michael I. 1997. “Measurements of Electric Anisotropy Due to Solidification Texturing and the Implications for the Earth’s Inner Core.” *Nature* 389 (6646): 60–63. https://doi.org/10.1038/37962.

Bergman, Michael I., Yahya Al-Khatatbeh, Daniel J. Lewis, and Margarita C. Shannon. 2014. “Deformation of Directionally Solidified Alloys: Evidence for Microstructural Hardening of Earth’s Inner Core?” *Comptes Rendus - Geoscience* 346 (5–6): 140–47. https://doi.org/10.1016/j.crte.2014.04.004.

Bergman, Michael I., Louis Giersch, Michael Hinczewski, and Valerie Izzo. 2000. “Elastic and Attenuation Anisotropy in Directionally Solidified (Hcp) Zinc, and the Seismic Anisotropy in the Earth’s Inner Core.” *Physics of the Earth and Planetary Interiors* 117 (1–4): 139–51. https://doi.org/10.1016/S0031-9201(99)00093-X.

Bergman, Michael I., Daniel J. Lewis, Ingyin Hla Myint, Liam Slivka, Shun-ichiro Karato, and Andrew Abreu. 2010. “Grain Growth and Loss of Texture during Annealing of Alloys, and the Translation of Earth’s Inner Core.” *Geophysical Research Letters* 37 (22): L22313. https://doi.org/10.1029/2010GL045103.

Bertka, Constance M., and Yingwei Fei. 1997. “Mineralogy of the Martian Interior up to Core-Mantle Boundary Pressures.” *Journal of Geophysical Research: Solid Earth* 102 (B3): 5251–64. https://doi.org/10.1029/96jb03270.

Bertka, Constance M., and Yingwei Fei. 1998. “Density Profile of an SNC Model Martian Interior and the Moment-of-Inertia Factor of Mars.” *Earth and Planetary Science Letters* 157 (1–2): 79–88. https://doi.org/10.1016/S0012-821X(98)00030-2.

Bertka, Constance M., and Yingwei Fei. 1998. “Implications of Mars Pathfinder Data for the Accretion History of the Terrestrial Planets.” *Science* 281 (5384): 1838–40. https://doi.org/10.1126/science.281.5384.1838.

Birch, Francis. 1986. “Equation of State and Thermodynamic Parameters of NaCl to 300 Kbar in the High-Temperature Domain.” *Journal of Geophysical Research* 91 (B5): 4949. https://doi.org/10.1029/jb091ib05p04949.

Birch, Francis. 1947. “Finite Elastic Strain of Cubic Crystals.” *Physical Review* 71 (11): 809–24. https://doi.org/10.1103/PhysRev.71.809.

Birch, Francis. 1952. “Elasticity and Constitution of the Earth’s Interior.” *Journal of Geophysical Research* 57 (2): 227–86. https://doi.org/https://doi.org/10.1029/JZ057i002p00227.

Birch, Francis. 1964. “Density and Composition of Mantle and Core.” *Journal of Geophysical Research* 69 (20): 4377–88. https://doi.org/10.1029/jz069i020p04377.

Bissig, Felix, Amir Khan, Martin van Driel, Simon C. Stähler, Domenico Giardini, Mark Panning, Mélanie Drilleau, et al. 2018. “On the Detectability and Use of Normal Modes for Determining Interior Structure of Mars.” *Space Science Reviews* 214 (8). https://doi.org/10.1007/s11214-018-0547-9.

Boehler, Reinhard, Marvin Ross, and David B. Boercker. 1996. “High-Pressure Melting Curves of Alkali Halides.” *Physical Review B - Condensed Matter and Materials Physics* 53 (2): 556–63. https://doi.org/10.1103/PhysRevB.53.556.

Borg, Lars E., and David S. Draper. 2003. “A Petrogenetic Model for the Origin and Compositional Variation of the Martian Basaltic Meteorites.” *Meteoritics and Planetary Science* 38 (12): 1713–31. https://doi.org/10.1111/j.1945-5100.2003.tb00011.x.

Borisov, S. V., and N. V. Podberezskaya. 2012. “X-Ray Diffraction Analysis: A Brief History and Achievements of the First Century.” *Journal of Structural Chemistry* 53 (1): 1–3.

Boujibar, Asmaa, Denis Andrault, Mohamed Ali Bouhifd, Nathalie Bolfan-Casanova, Jean Luc Devidal, and Nicolas Trcera. 2014. “Metal-Silicate Partitioning of Sulphur, New Experimental and Thermodynamic Constraints on Planetary Accretion.” *Earth and Planetary Science Letters* 391: 42–54. https://doi.org/10.1016/j.epsl.2014.01.021.

Bouvier, Audrey, Janne Blichert-Toft, and Francis Albarède. 2009. “Martian Meteorite Chronology and the Evolution of the Interior of Mars.” *Earth and Planetary Science Letters* 280 (1–4): 285–95. https://doi.org/10.1016/j.epsl.2009.01.042.

Bouvier, Laura C., Maria M. Costa, James N. Connelly, Ninna K. Jensen, Daniel Wielandt, Michael Storey, Alexander A. Nemchin, et al. 2018. “Evidence for Extremely Rapid Magma Ocean Crystallization and Crust Formation on Mars.” *Nature* 558 (7711): 586–89. https://doi.org/10.1038/s41586-018-0222-z.

Bragg, William H., and William L. Bragg. 1913. “The Reflection of X-Rays by Crystals.” *Proceedings of the Royal Society of London A* 88: 428–38.

Brennan, Matthew C., Rebecca A. Fischer, Samantha Couper, Lowell Miyagi, Daniele Antonangeli, and Guillaume Morard. 2021. “High-Pressure Deformation of Iron–Nickel–Silicon Alloys and Implications for Earth’s Inner Core.” *Journal of Geophysical Research: Solid Earth* 126 (3). https://doi.org/10.1029/2020JB021077.

Brennan, Matthew C., Rebecca A. Fischer, and Jessica C. E. Irving. 2020. “Core Formation and Geophysical Properties of Mars.” *Earth and Planetary Science Letters* 530: 115923. https://doi.org/10.1016/j.epsl.2019.115923.
Brennan, Matthew C., Rebecca A. Fischer, Francis Nimmo, and David P. O’Brien. 2022. “Timing of Martian Core Formation from Models of Hf–W Evolution Coupled with N-Body Simulations.” *Geochimica et Cosmochimica Acta* 316: 295–308. https://doi.org/10.1016/j.gca.2021.09.022.
Breuer, Doris, Dave A. Yuen, Tilman Spohn, and Shuxia Zhang. 1998. “Three Dimensional Models of Martian Mantle Convection with Phase Transitions.” *Geophysical Research Letters* 25 (3): 229–32. https://doi.org/10.1029/97GL03767.
Bridgman, Percy W. 1912. “Water, in the Liquid and Five Solid Forms, under Pressure.” *Proceedings of the American Academy of Arts and Sciences* 47 (13): 441–558.
Bridgman, Percy W. 1939. “The High Pressure Behavior of Miscellaneous Minerals.” *American Journal of Sciences* 237 (1): 7–18.
Buffett, B. A., and H. R. Wenk. 2001. “Texturing of the Earth’s Inner Core by Maxwell Stresses.” *Nature* 413 (6851): 60–63. https://doi.org/10.1038/35092543.
Cambioni, Saverio, Seth A. Jacobson, Alexandre Emsenhuber, Erik Asphaug, David C. Rubie, Travis S.J. Gabriel, Stephen R. Schwartz, and Roberto Furfaro. 2021. “The Effect of Inefficient Accretion on Planetary Differentiation.” *The Planetary Science Journal* 2 (3): 93. https://doi.org/10.3847/PSJ/ABF0AD.
Cameron, A.G.W. 1962. “The Formation of the Sun and Planets.” *Icarus* 1 (6): 13–69.
Campbell, Andrew J., Lisa Danielson, Kevin Righter, Christopher T. Seagle, Yanbin Wang, and Vitali B. Prakapenka. 2009. “High Pressure Effects on the Iron-Iron Oxide and Nickel-Nickel Oxide Oxygen Fugacity Buffers.” *Earth and Planetary Science Letters* 286 (3–4): 556–64. https://doi.org/10.1016/j.epsl.2009.07.022.
Campbell, Andrew J., Christopher T. Seagle, Dion L. Heinz, Guoyin Shen, and Vitali B. Prakapenka. 2007. “Partial Melting in the Iron-Sulfur System at High Pressure: A Synchrotron X-Ray Diffraction Study.” *Physics of the Earth and Planetary Interiors* 162 (1–2): 119–28. https://doi.org/10.1016/j.pepi.2007.04.001.
Canup, Robin M. 2008. “Accretion of the Earth.” *Philosophical Transactions of the Royal Society A: Mathematical, Physical and Engineering Sciences*. Royal Society. https://doi.org/10.1098/rsta.2008.0101.
Chambers, J. E. 2013. “Late-Stage Planetary Accretion Including Hit-and-Run Collisions and Fragmentation.” *Icarus* 224 (1): 43–56. https://doi.org/10.1016/j.icarus.2013.02.015.
Chambers, J. E. 2001. “Making More Terrestrial Planets.” *Icarus* 152 (2): 205–24. https://doi.org/10.1006/icar.2001.6639.
Chambers, John E. 2006. “A Semi-Analytic Model for Oligarchic Growth.” *Icarus* 180 (2): 496–513. https://doi.org/10.1016/j.icarus.2005.10.017.
Chambers, John E. 2004. “Planetary Accretion in the Inner Solar System.” *Earth and Planetary Science Letters* 223 (3–4): 241–52. https://doi.org/10.1016/j.epsl.2004.04.031.
Chen, Bin, Lili Gao, Ken Ichi Funakoshi, and Jie Li. 2007. “Thermal Expansion of Iron-Rich Alloys and Implications for the Earth’s Core.” *Proceedings of the National Academy of Sciences of the United States of America* 104 (22): 9162–67. https://doi.org/10.1073/pnas.0610474104.
Chi, Han, Rajdeep Dasgupta, Megan S. Duncan, and Nobumichi Shimizu. 2014. “Partitioning of Carbon between Fe-Rich Alloy Melt and Silicate Melt in a Magma Ocean - Implications for the Abundance and Origin of Volatiles in Earth, Mars, and the Moon.” *Geochimica et Cosmochimica Acta* 139: 447–71. https://doi.org/10.1016/j.gca.2014.04.046.
Chidester, B. A., E. C. Thompson, R. A. Fischer, D. L. Heinz, V. B. Prakapenka, Y. Meng, and A. J. Campbell. 2021. “Experimental Thermal Equation of State Of.” *Physical Review B* 104 (9): 094107. https://doi.org/10.1103/PhysRevB.104.094107.
Ciesla, Fred J., and Jeffrey N. Cuzzi. 2006. “The Evolution of the Water Distribution in a Viscous Protoplanetary Disk.” *Icarus* 181 (1): 178–204. https://doi.org/10.1016/j.icarus.2005.11.009.

Clement, Matthew S., Nathan A. Kaib, and John E. Chambers. 2020. “Embryo Formation with GPU Acceleration: Reevaluating the Initial Conditions for Terrestrial Accretion.” *The Planetary Science Journal* 1 (May): 18. https://doi.org/10.3847/psj/ab91aa.
Clement, Matthew S., Nathan A. Kaib, Sean N. Raymond, John E. Chambers, and Kevin J. Walsh. 2019. “The Early Instability Scenario: Terrestrial Planet Formation during the Giant Planet Instability, and the Effect of Collisional Fragmentation.” *Icarus* 321 (March): 778–90. https://doi.org/10.1016/J.ICARUS.2018.12.033.
Clement, Matthew S., Nathan A. Kaib, Sean N. Raymond, and John E. Chambers. 2021. “The Early Instability Scenario: Mars’ Mass Explained by Jupiter’s Orbit.” *Icarus* 367 (October): 114585. https://doi.org/10.1016/J.ICARUS.2021.114585.
Clesi, Vincent, Mohamed Ali Bouhifd, Nathalie Bolfan-Casanova, Geeth Manthilake, Federica Schiavi, Caroline Raepsaet, Hélène Bureau, Hicham Khodja, and Denis Andrault. 2018. “Low Hydrogen Contents in the Cores of Terrestrial Planets.” *Science Advances* 4 (3). https://doi.org/10.1126/sciadv.1701876.
Clinton, J. F., D. Giardini, P. Lognonné, B. Banerdt, M. Van Driel, M. Drilleau, N. Murdoch, et al. 2017. “Preparing for in Sight: An Invitation to Participate in a Blind Test for Martian Seismicity.” *Seismological Research Letters* 88 (5): 1290–1302. https://doi.org/10.1785/0220170094.
Collinet, Max, Etienne Médard, Bernard Charlier, Jacqueline Vander Auwera, and Timothy L. Grove. 2015. “Melting of the Primitive Martian Mantle at 0.5-2.2 GPa and the Origin of Basalts and Alkaline Rocks on Mars.” *Earth and Planetary Science Letters* 427: 83–94. https://doi.org/10.1016/j.epsl.2015.06.056.
Connolly, J. A.D. 2009. “The Geodynamic Equation of State: What and How.” *Geochemistry, Geophysics, Geosystems* 10 (10): Q10014. https://doi.org/10.1029/2009GC002540.
Corgne, Alexandre, Shantanu Keshav, Bernard J. Wood, William F. McDonough, and Yingwei Fei. 2008. “Metal-Silicate Partitioning and Constraints on Core Composition and Oxygen Fugacity during Earth Accretion.” *Geochimica et Cosmochimica Acta* 72 (2): 574–89. https://doi.org/10.1016/j.gca.2007.10.006.
Cottrell, Elizabeth, Michael J Walter, and David Walker. 2009. “Metal-Silicate Partitioning of Tungsten at High Pressure and Temperature: Implications for Equilibrium Core Formation in Earth.” *Earth and Planetary Science Letters* 281: 275–87. https://doi.org/10.1016/j.epsl.2009.02.024.
Crotwell, H. P., T. J. Owens, and J. Ritsema. 1999. “The TauP Toolkit: Flexible Seismic Travel-Time and Ray-Path Utilities.” *Seismological Research Letters* 70 (2): 154–60. https://doi.org/10.1785/gssrl.70.2.154.
Dale, Christopher W., Kevin W. Burton, Richard C. Greenwood, Abdelmouhcine Gannoun, Jonathan Wade, Bernard J. Wood, and D. Graham Pearson. 2012. “Late Accretion on the Earliest Planetesimals Revealed by the Highly Siderophile Elements.” *Science* 336 (6077): 72–75. https://doi.org/10.1126/SCIENCE.1214967.
Dauphas, N., and A. Pourmand. 2011. “Hf-W-Th Evidence for Rapid Growth of Mars and Its Status as a Planetary Embryo.” *Nature* 473 (7348): 489–92. https://doi.org/10.1038/nature10077.
Dauphas, Nicolas, Christoph Burkhardt, Paul H Warren, and Zhen Teng. 2014. “Geochemical Arguments for an Earth-like Moon-Forming Impactor.” *Phil. Trans. R. Soc. A* 372 (2024): 20130244. https://doi.org/10.1098/rsta.2013.0244.
Laeter, J. R. De, J. K. Böhlke, P. De Bièvre, H. Hidaka, H. S. Peiser, K. J.R. Rosman, and P. D.P. Taylor. 2003. “Atomic Weights of the Elements: Review 2000 (IUPAC Technical Report).” *Pure and Applied Chemistry* 75 (6): 683–800. https://doi.org/10.1351/pac200375060683.
Debaille, V., A. D. Brandon, Q. Z. Yin, and B. Jacobsen. 2007. “Coupled 142Nd–143Nd Evidence for a Protracted Magma Ocean in Mars.” *Nature 2007 450:7169* 450 (7169): 525–28. https://doi.org/10.1038/nature06317.
Deguen, Renaud, Maylis Landeau, and Peter Olson. 2014. “Turbulent Metal-Silicate Mixing, Fragmentation, and Equilibration in Magma Oceans.” *Earth and Planetary Science Letters* 391 (April): 274–87. https://doi.org/10.1016/j.epsl.2014.02.007.

Deng, Sizhuang, and Alan Levander. 2020. “Autocorrelation Reflectivity of Mars.” *Geophysical Research Letters* 47 (16): e2020GL089630. https://doi.org/10.1029/2020GL089630.
Deuss, Arwen. 2014. “Heterogeneity and Anisotropy of Earth’s Inner Core.” *The Annual Review of Earth and Planetary Sciences* 42: 103–26. https://doi.org/10.1146/annurev-earth-060313-054658.
Dewaele, A., A. B. Belonoshko, G. Garbarino, F. Occelli, P. Bouvier, M. Hanfland, and M. Mezouar. 2012. “High-Pressure-High-Temperature Equation of State of KCl and KBr.” *Physical Review B - Condensed Matter and Materials Physics* 85 (21). https://doi.org/10.1103/PhysRevB.85.214105.
Dewaele, Agnès, Paul Loubeyre, Florent Occelli, Mohamed Mezouar, Peter I. Dorogokupets, and Marc Torrent. 2006. “Quasihydrostatic Equation of State of Iron above 2 Mbar.” *Physical Review Letters* 97 (21): 215504. https://doi.org/10.1103/PhysRevLett.97.215504.
Dewey, James, and Perry Byerly. 1969. “The Early History of Seismometry (to 1900).” *Bulletin of the Seismological Society of America* 59 (1): 183–227.
Dong, Haini, Susannah M. Dorfman, Christopher M. Holl, Yue Meng, Vitali B. Prakapenka, Duanwei He, and Thomas S. Duffy. 2014. “Compression of Lithium Fluoride to 92 GPa.” *High Pressure Research* 34 (1): 39–48. https://doi.org/10.1080/08957959.2013.878932.
Drążkowska, J., Y. Alibert, and B. Moore. 2016. “Close-in Planetesimal Formation by Pile-up of Drifting Pebbles.” *Astronomy & Astrophysics* 594 (October): A105. https://doi.org/10.1051/0004-6361/201628983.
Dreibus, G., and H. Wãnke. 1985. “Mars, a Volatile Rich Planet.” *Meteoritics* 20 (2): 367–80.
Dugaro, A., G. C. De Elía, and L. A. Darriba. 2019. “Physical Properties of Terrestrial Planets and Water Delivery in the Habitable Zone Using N -Body Simulations with Fragmentation.” *Astronomy and Astrophysics* 632 (December): A14. https://doi.org/10.1051/0004-6361/201936061.
Duncan, Megan S., Nicholas C. Schmerr, Constance M. Bertka, and Yingwei Fei. 2018. “Extending the Solidus for a Model Iron-Rich Martian Mantle Composition to 25 GPa.” *Geophysical Research Letters* 45 (19): 10,211-10,220. https://doi.org/10.1029/2018GL078182.
Dwyer, Christina A., Francis Nimmo, and John E. Chambers. 2015. “Bulk Chemical and Hf-W Isotopic Consequences of Incomplete Accretion during Planet Formation.” *Icarus* 245 (January): 145–52. https://doi.org/10.1016/j.icarus.2014.09.010.
Dziewonski, Adam M., and Don L. Anderson. 1981. “Preliminary Reference Earth Model.” *Physics of the Earth and Planetary Interiors* 25 (4): 297–356. https://doi.org/10.1016/0031-9201(81)90046-7.
Dziewoński, Adam M., and Barbara Romanowicz. 2015. “Deep Earth Seismology.” In *Treatise on Geophysics*.
Fei, Yingwei, Angele Ricolleau, Mark Frank, Kenji Mibe, Guoyin Shen, and Vitali Prakapenka. 2007. “Toward an Internally Consistent Pressure Scale.” *Proceedings of the National Academy of Sciences of the United States of America* 104 (22): 9182–86. https://doi.org/10.1073/pnas.0609013104.
Fischer, Rebecca A., and Andrew J. Campbell. 2015. “The Axial Ratio of Hcp Fe and Fe-Ni-Si Alloys to the Conditions of Earth’s Inner Core.” *American Mineralogist* 100 (11–12): 2718–24. https://doi.org/10.2138/am-2015-5191.
Fischer, Rebecca A., Andrew J. Campbell, Razvan Caracas, Daniel M. Reaman, Dion L. Heinz, Przemyslaw Dera, and Vitali B. Prakapenka. 2014. “Equations of State in the Fe-FeSi System at High Pressures and Temperatures.” *Journal of Geophysical Research: Solid Earth* 119 (4): 2810–27. https://doi.org/10.1002/2013JB010898.
Fischer, Rebecca A., Andrew J. Campbell, and Fred J. Ciesla. 2017. “Sensitivities of Earth’s Core and Mantle Compositions to Accretion and Differentiation Processes.” *Earth and Planetary Science Letters* 458: 252–62. https://doi.org/10.1016/j.epsl.2016.10.025.
Fischer, Rebecca A., Andrew J. Campbell, Daniel M. Reaman, Noah A. Miller, Dion L. Heinz, Przymyslaw Dera, and Vitali B. Prakapenka. 2013. “Phase Relations in the Fe-FeSi System at High Pressures and Temperatures.” *Earth and Planetary Science Letters* 373: 54–64. https://doi.org/10.1016/j.epsl.2013.04.035.

Fischer, Rebecca A., Yoichi Nakajima, Andrew J. Campbell, Daniel J. Frost, Dennis Harries, Falko Langenhorst, Nobuyoshi Miyajima, Kilian Pollok, and David C. Rubie. 2015. “High Pressure Metal-Silicate Partitioning of Ni, Co, V, Cr, Si, and O.” *Geochimica et Cosmochimica Acta* 167: 177–94. https://doi.org/10.1016/j.gca.2015.06.026.

Fischer, Rebecca A., and Francis Nimmo. 2018. “Effects of Core Formation on the Hf–W Isotopic Composition of the Earth and Dating of the Moon-Forming Impact.” *Earth and Planetary Science Letters* 499: 257–65. https://doi.org/10.1016/j.epsl.2018.07.030.

Fischer, Rebecca A., Francis Nimmo, and David P. O’Brien. 2018. “Radial Mixing and Ru–Mo Isotope Systematics under Different Accretion Scenarios.” *Earth and Planetary Science Letters* 482 (January): 105–14. https://doi.org/10.1016/j.epsl.2017.10.055.

Fischer, Rebecca A, and Fred J Ciesla. 2014. “Dynamics of the Terrestrial Planets from a Large Number of N-Body Simulations.” *Earth and Planetary Science Letters* 392: 28–38. https://doi.org/10.1016/j.epsl.2014.02.011.

Flórez, M., J. M. Recio, E. Francisco, M. A. Blanco, and A. Martín Pendás. 2002. “First-Principles Study of the Rocksalt-Cesium Chloride Relative Phase Stability in Alkali Halides.” *Physical Review B - Condensed Matter and Materials Physics* 66 (14): 1–8. https://doi.org/10.1103/PhysRevB.66.144112.

Foley, C. Nicole, M. Wadhwa, L. E. Borg, P. E. Janney, R. Hines, and T. L. Grove. 2005. “The Early Differentiation History of Mars from 182W-142Nd Isotope Systematics in the SNC Meteorites.” *Geochimica et Cosmochimica Acta* 69 (18): 4557–71. https://doi.org/10.1016/j.gca.2005.05.009.

Frost, Daniel J., Yuki Asahara, David C. Rubie, Nobuyoshi Miyajima, Leonid S. Dubrovinsky, Christian Holzapfel, Eiji Ohtani, Masaaki Miyahara, and Takeshi Sakai. 2010. “Partitioning of Oxygen between the Earth’s Mantle and Core.” *Journal of Geophysical Research: Solid Earth* 115 (2). https://doi.org/10.1029/2009JB006302.

Georg, R. Bastian, Alex N. Halliday, Edwin A. Schauble, and Ben C. Reynolds. 2007. “Silicon in the Earth’s Core.” *Nature* 447 (7148): 1102–6. https://doi.org/10.1038/nature05927.

Gessmann, C. K., B. J. Wood, D. C. Rubie, and M. R. Kilburn. 2001. “Solubility of Silicon in Liquid Metal at High Pressure: Implications for the Composition of the Earth’s Core.” *Earth and Planetary Science Letters* 184 (2): 367–76. https://doi.org/10.1016/S0012-821X(00)00325-3.

Geßmann, Christine K., and David C. Rubie. 2000. “The Origin of the Depletions of V, Cr and Mn in the Mantles of the Earth and Moon.” *Earth and Planetary Science Letters* 184 (1): 95–107. https://doi.org/10.1016/S0012-821X(00)00323-X.

Gilbert, F., and Adam M. Dziewoński. 1975. “An Application of Normal Mode Theory to the Retrieval of Structural Parameters and Source Mechanisms from Seismic Spectra.” *Philosophical Transactions of the Royal Society of London. Series A, Mathematical and Physical Sciences* 278 (1280): 187–269. https://doi.org/10.1098/rsta.1975.0025.

Gleason, A. E., and W. L. Mao. 2013. “Strength of Iron at Core Pressures and Evidence for a Weak Earth’s Inner Core.” *Nature Geoscience* 6 (7): 571–74. https://doi.org/10.1038/ngeo1808.

Goldschmidt, V. M. 1937. “The Principles of Distribution of Chemical Elements in Minerals and Rocks.” *Journal of the Chemical Society*, 655–73. https://doi.org/10.1039/jr9370000655.

Gomi, Hitoshi, Yingwei Fei, and Takashi Yoshino. 2018. “The Effects of Ferromagnetism and Interstitial Hydrogen on the Equation of States of Hcp and Dhcp FeHx: Implications for the Earth’s Inner Core Age.” *American Mineralogist* 103 (8): 1271–81. https://doi.org/10.2138/am-2018-6295.

Goossens, Sander, Terence J. Sabaka, Antonio Genova, Erwan Mazarico, Joseph B. Nicholas, and Gregory A. Neumann. 2017. “Evidence for a Low Bulk Crustal Density for Mars from Gravity and Topography.” *Geophysical Research Letters* 44 (15): 7686–94. https://doi.org/10.1002/2017GL074172.

Grott, M., D. Baratoux, E. Hauber, V. Sautter, J. Mustard, O. Gasnault, S. W. Ruff, et al. 2012. “Long-Term Evolution of the Martian Crust-Mantle System.” *Space Science Reviews* 174: 49–111. https://doi.org/10.1007/978-1-4614-7774-7_5.

Gutenberg, Beno. 1914. “Beobachtungen an Registrierungen von Fernbeben in Göttingen Und Folgerungen Über Die Konstitution Des Erdkörpers.” *Nachrichten von Der Gesellschaft Der Wissenschaften Zu Göttingen, Mathematisch-Physikalische Klasse*, 125–76.

Hansen, Brad M.S. 2009. “Formation of the Terrestrial Planets from a Narrow Annulus.” *Astrophysical Journal* 703 (1): 1131–40. https://doi.org/10.1088/0004-637X/703/1/1131.
Harper, Charles L., and Stein B. Jacobsen. 1996. “Evidence for 182Hf in the Early Solar System and Constraints on the Timescale of Terrestrial Accretion and Core Formation.” *Geochimica et Cosmochimica Acta* 60 (7): 1131–53. https://doi.org/10.1016/0016-7037(96)00027-0.
Harper, Charles L., Laurence E. Nyquist, Brij Bansal, Henry Wiesmann, and Chi Yu Shih. 1995. “Rapid Accretion and Early Differentiation of Mars Indicated by 142Nd/144Nd in SNC Meteorites.” *Science* 267 (5195): 213–17. https://doi.org/10.1126/SCIENCE.7809625.
Harrison, J. C. 1963. “An Analysis of the Lunar Tides.” *Journal of Geophysical Research* 68 (14): 4269–80. https://doi.org/10.1029/jz068i014p04269.
Helffrich, George. 2017. “Mars Core Structure—Concise Review and Anticipated Insights from Insight.” *Progress in Earth and Planetary Science* 4 (1). https://doi.org/10.1186/s40645-017-0139-4.
Hemley, Russell J., Ho Kwang Mao, Guoyin Shen, James Badro, Philippe Gillet, Michael Hanfland, and Daniel Häusermann. 1997. “X-Ray Imaging of Stress and Strain of Diamond, Iron, and Tungsten at Megabar Pressures.” *Science* 276 (5316): 1242–45. https://doi.org/10.1126/science.276.5316.1242.
Hennessy, Henry. 1872. “The Rigidity of the Earth.” *Nature* 5 (119): 288–89. https://doi.org/10.1038/005288a0.
Hutton, Charles. 1778. “An Account of the Calculations Made from the Survey and Measures Taken at Schehallien, in Order to Ascertain the Mean Density of the Earth.” *Philosophical Transactions of the Royal Society of London* 68: 689–788.
Irving, J. C. E., and A. Deuss. 2011. “Hemispherical Structure in Inner Core Velocity Anisotropy.” *Journal of Geophysical Research* 116 (B4): B04307. https://doi.org/10.1029/2010JB007942.
Ishii, Miaki, and Adam M. Dziewoński. 2002. “The Innermost Inner Core of the Earth: Evidence for a Change in Anisotropic Behavior at the Radius of about 300 Km.” *Proceedings of the National Academy of Sciences* 99 (22): 14026–30. https://doi.org/10.1073/pnas.172508499.
Jacobsen, Stein B. 2005. “The Hf-W Isotopic System and the Origin of the Earth and Moon.” *Annual Review of Earth and Planetary Sciences* 33: 531–70. https://doi.org/10.1146/annurev.earth.33.092203.122614.
Jacobsen, Steven D., Fuming Jiang, Zhu Mao, Thomas S. Duffy, Joseph R. Smyth, Christopher M. Holl, and Daniel J. Frost. 2008. “Effects of Hydration on the Elastic Properties of Olivine.” *Geophysical Research Letters* 35 (14). https://doi.org/10.1029/2008GL034398.
Jacobson, S. A., and A. Morbidelli. 2014. “Lunar and Terrestrial Planet Formation in the Grand Tack Scenario.” *Philosophical Transactions of the Royal Society A: Mathematical, Physical and Engineering Sciences* 372 (2024): 20130174. https://doi.org/10.1098/rsta.2013.0174.
Japan Society for the Promotion of Science. 1998. “Recommended Values of Activity Coefficients and Interaction Parameters of Elements in Iron Alloys.” In *Steelmaking Data Sourcebook*, 273–297.
Javoy, M. 1997. “The Major Volatile Elements of the Earth: Their Origin, Behavior, Fate.” *Geophysical Research Letters* 24 (2): 177–80. https://doi.org/10.1029/96GL03931.
Jeanloz, Raymond, and Hans-Rudolf -R Wenk. 1988. “Convection and Anisotropy of the Inner Core.” *Geophysical Research Letters* 15 (1): 72–75. https://doi.org/10.1029/GL015i001p00072.
Jennings, E. S., S. A. Jacobson, D. C. Rubie, Y. Nakajima, A. K. Vogel, L. A. Rose-Weston, and D. J. Frost. 2021. “Metal–Silicate Partitioning of W and Mo and the Role of Carbon in Controlling Their Abundances in the Bulk Silicate Earth.” *Geochimica et Cosmochimica Acta* 293 (January): 40–69. https://doi.org/10.1016/J.GCA.2020.09.035.
Kaiura, G. H., and J. M. Toguri. 1979. “Densities of the Molten FeS, FeS-Cu2S AND Fe-S-O Systems-Utilizing a Bottom-Balance Archimedean Technique.” *Canadian Metallurgical Quarterly* 18 (2): 155–64. https://doi.org/10.1179/cmq.1979.18.2.155.

Kanitpanyacharoen, W., S. Merkel, L. Miyagi, P. Kaercher, C. N. Tomé, Y. Wang, and H. R. Wenk. 2012. “Significance of Mechanical Twinning in Hexagonal Metals at High Pressure.” *Acta Materialia* 60 (1): 430–42. https://doi.org/10.1016/j.actamat.2011.07.055.

Karato, Shun Ichiro. 2008. *Deformation of Earth Materials: An Introduction to the Rheology of Solid Earth. Deformation of Earth Materials: An Introduction to the Rheology of Solid Earth*. 1st ed. Vol. 9780521844. Cambridge University Press. https://doi.org/10.1017/CBO9780511804892.

Karato, Shun Ichiro. 1993. “Inner Core Anisotropy Due to the Magnetic Field-Induced Preferred Orientation of Iron.” *Science* 262 (5140): 1708–11. https://doi.org/10.1126/science.262.5140.1708.

Kassner, Michael E. 2008. *Fundamentals of Creep in Metals and Alloys. Fundamentals of Creep in Metals and Alloys*. 3rd ed. Elsevier Science. https://doi.org/10.1016/B978-0-08-047561-5.X0001-2.

Kavner, Abby, Thomas S. Duffy, and Guoyin Shen. 2001. “Phase Stability and Density of FeS at High Pressures and Temperatures: Implications for the Interior Structure of Mars.” *Earth and Planetary Science Letters* 185 (1–2): 25–33. https://doi.org/10.1016/S0012-821X(00)00356-3.

Kenyon, Scott J., and Benjamin C. Bromley. 2006. “Terrestrial Planet Formation. I. The Transition from Oligarchic Growth to Chaotic Growth.” *The Astronomical Journal* 131 (3): 1837–50. https://doi.org/10.1086/499807.

Khan, A., and James A.D. D. Connolly. 2008. “Constraining the Composition and Thermal State of Mars from Inversion of Geophysical Data.” *Journal of Geophysical Research: Planets* 113 (7): E07003. https://doi.org/10.1029/2007JE002996.

Khan, A., C. Liebske, A. Rozel, A. Rivoldini, F. Nimmo, J. A.D. Connolly, A. C. Plesa, and D. Giardini. 2018. “A Geophysical Perspective on the Bulk Composition of Mars.” *Journal of Geophysical Research: Planets* 123 (2): 575–611. https://doi.org/10.1002/2017JE005371.

Kiefer, Walter S., and Qingsong Li. 2016. “Water Undersaturated Mantle Plume Volcanism on Present-Day Mars.” *Meteoritics and Planetary Science* 51 (11): 1993–2010. https://doi.org/10.1111/maps.12720.

Kleine, Thorsten, and Richard J. Walker. 2017. “Tungsten Isotopes in Planets.” *Annual Review of Earth and Planetary Sciences* 45 (1): 389–417. https://doi.org/10.1146/annurev-earth-063016-020037.

Kobayashi, Hiroshi, and Nicolas Dauphas. 2013. “Small Planetesimals in a Massive Disk Formed Mars.” *Icarus* 225 (1): 122–30. https://doi.org/10.1016/j.icarus.2013.03.006.

Köhler, U., P. G. Johannsen, and W. B. Holzapfel. 1997. “Equation-of-State Data for CsCl-Type Alkali Halides.” *Journal of Physics Condensed Matter* 9 (26): 5581–92. https://doi.org/10.1088/0953-8984/9/26/007.

Kokubo, Eiichiro, and Hidenori Genda. 2010. “Formation of Terrestrial Planets from Protoplanets under a Realistic Accretion Condition.” *Astrophysical Journal Letters* 714 (1 PART 2): L21. https://doi.org/10.1088/2041-8205/714/1/L21.

Komabayashi, Tetsuya, and Yingwei Fei. 2010. “Internally Consistent Thermodynamic Database for Iron to the Earth’s Core Conditions.” *Journal of Geophysical Research: Solid Earth* 115 (3). https://doi.org/10.1029/2009JB006442.

Komabayashi, Tetsuya, Giacomo Pesce, Guillaume Morard, Daniele Antonangeli, Ryosuke Sinmyo, and Mohamed Mezouar. 2019. “Phase Transition Boundary between Fcc and Hcp Structures in Fe-Si Alloy and Its Implications for Terrestrial Planetary Cores.” *American Mineralogist* 104 (1): 94–99. https://doi.org/10.2138/am-2019-6636.

Konopliv, Alex S., Sami W. Asmar, William M. Folkner, Özgür Karatekin, Daniel C. Nunes, Suzanne E. Smrekar, Charles F. Yoder, and Maria T. Zuber. 2011. “Mars High Resolution Gravity Fields from MRO, Mars Seasonal Gravity, and Other Dynamical Parameters.” *Icarus* 211 (1): 401–28. https://doi.org/10.1016/j.icarus.2010.10.004.

Konopliv, Alex S., Ryan S. Park, and William M. Folkner. 2016. “An Improved JPL Mars Gravity Field and Orientation from Mars Orbiter and Lander Tracking Data.” *Icarus* 274: 253–60. https://doi.org/10.1016/j.icarus.2016.02.052.

Koot, Laurence, and Mathieu Dumberry. 2011. “Viscosity of the Earth’s Inner Core: Constraints from Nutation Observations.” *Earth and Planetary Science Letters* 308 (3–4): 343–49. https://doi.org/10.1016/j.epsl.2011.06.004.
Kotan, Hasan, Kris A. Darling, Mostafa Saber, Ronald O. Scattergood, and Carl C. Koch. 2013. “An in Situ Experimental Study of Grain Growth in a Nanocrystalline Fe91 Ni8 Zr1 Alloy.” *Journal of Materials Science* 48 (5): 2251–57. https://doi.org/10.1007/s10853-012-7002-1.
Kruijer, Thomas S., Thorsten Kleine, Lars E. Borg, Gregory A. Brennecka, Anthony J. Irving, Addi Bischoff, and Carl B. Agee. 2017. “The Early Differentiation of Mars Inferred from Hf–W Chronometry.” *Earth and Planetary Science Letters* 474 (September): 345–54. https://doi.org/10.1016/j.epsl.2017.06.047.
Kruijer, Thomas S., Thorsten Kleine, Mario Fischer-Gödde, Christoph Burkhardt, and Rainer Wieler. 2014. “Nucleosynthetic W Isotope Anomalies and the Hf-W Chronometry of Ca-Al-Rich Inclusions.” *Earth and Planetary Science Letters* 403 (October): 317–27. https://doi.org/10.1016/j.epsl.2014.07.003.
Kunz, Martin, Alastair A. MacDowell, Wendel A. Caldwell, Daniella Cambie, Richard S. Celestre, Edward E. Domning, Robert M. Duarte, et al. 2005. “A Beamline for High-Pressure Studies at the Advanced Light Source with a Superconducting Bending Magnet as the Source.” *Journal of Synchrotron Radiation* 12 (5): 650–58. https://doi.org/10.1107/S0909049505020959.
Kunz, Martin, Jinyuan Yan, Earl Cornell, Edward E. Domning, C. Ethan Yen, Andrew Doran, Christine M. Beavers, Aaron Treger, Quentin Williams, and Alastair A. MacDowell. 2018. “Implementation and Application of the Peak Scaling Method for Temperature Measurement in the Laser Heated Diamond Anvil Cell.” *Review of Scientific Instruments* 89 (8): 083903. https://doi.org/10.1063/1.5028276.
Lee, Der Chuen, and Alex N. Halliday. 1995. “Hafnium–Tungsten Chronometry and the Timing of Terrestrial Core Formation.” *Nature* 378 (6559): 771–74. https://doi.org/10.1038/378771a0.
Lehmann, Inge. 1936. “P’.” *Publ. Bur. Centr. Seism. Internat. Serie A* 14: 87–115.
Levison, Harold F., Katherine A. Kretke, Kevin J. Walsh, and William F. Bottke. 2015. “Growing the Terrestrial Planets from the Gradual Accumulation of Submeter-Sized Objects.” *Proceedings of the National Academy of Sciences of the United States of America* 112 (46): 14180–85. https://doi.org/10.1073/pnas.1513364112.
Li, J., and C. B. Agee. 2001. “The Effect of Pressure, Temperature, Oxygen Fugacity and Composition on Partitioning of Nickel and Cobalt between Liquid Fe-Ni-S Alloy and Liquid Silicate: Implications for the Earth’s Core Formation.” *Geochimica et Cosmochimica Acta* 65 (11): 1821–32. https://doi.org/10.1016/S0016-7037(00)00613-X.
Lichtenberg, Tim, Joanna Drążkowska, Maria Schönbächler, Gregor J. Golabek, and Thomas O. Hands. 2021. “Bifurcation of Planetary Building Blocks during Solar System Formation.” *Science* 371 (6527): 365–70. https://doi.org/10.1126/science.abb3091.
Lin, Jung-Fu, Andrew J Campbell, Dion L Heinz, Guoyin Shen, J.-F Lin, A J Campbell, D L Heinz, and G Shen. 2003. “Static Compression of Iron-Silicon Alloys: Implications for Silicon in the Earth’s Core.” *Journal of Geophysical Research: Solid Earth* 108 (B1): 2045. https://doi.org/10.1029/2002JB001978.
Lissauer, Jack J. 2007. “Planets Formed in Habitable Zones of M Dwarf Stars Probably Are Deficient in Volatiles.” *The Astrophysical Journal* 660 (2): L149–52. https://doi.org/10.1086/518121.
Lodders, K., and B. Fegley. 1997. “An Oxygen Isotope Model for the Composition of Mars.” *Icarus* 126 (2): 373–94. https://doi.org/10.1006/icar.1996.5653.
Lodders, Katharina. 2010. “Solar System Abundances of the Elements.” *Astrophysics and Space Science Proceedings* 0 (202579): 379–417. https://doi.org/10.1007/978-3-642-10352-0_8.
Lodders, Katharina, and B. Fegley. 1998. “Meteorite Classification and Companion Tables.” In *The Planetary Scientist’s Companion*, 295–331. Oxford University Press.
Longhi, John, E. Knittle, J. R. Holloway, and H. Wänke. 1992. “The Bulk Composition, Mineralogy and Internal Structure of Mars.” In *Mars*, 184–208. https://doi.org/10.2307/j.ctt207g59v.10.

Ma, Zhongting. 2001. “Thermodynamic Description for Concentrated Metallic Solutions Using Interaction Parameters.” *Metallurgical and Materials Transactions B: Process Metallurgy and Materials Processing Science* 32 (1): 87–103. https://doi.org/10.1007/s11663-001-0011-0.
MacPherson, G. J. 2013. “Calcium-Aluminum-Rich Inclusions in Chondritic Meteorites.” *Treatise on Geochemistry: Second Edition* 1: 139–79. https://doi.org/10.1016/B978-0-08-095975-7.00105-4.
Mah, Jingyi, and Ramon Brasser. 2021. “Isotopically Distinct Terrestrial Planets via Local Accretion.” *Icarus* 354 (January): 114052. https://doi.org/10.1016/J.ICARUS.2020.114052.
Marchi, Simone, Richard J. Walker, and Robin M. Canup. 2020. “A Compositionally Heterogeneous Martian Mantle Due to Late Accretion.” *Science Advances* 6 (7): eaay2338. https://doi.org/10.1126/sciadv.aay2338.
Mare, Eleanor R., Andrew G. Tomkins, and Belinda M. Godel. 2014. “Restriction of Parent Body Heating by Metal-Troilite Melting: Thermal Models for the Ordinary Chondrites.” *Meteoritics and Planetary Science* 49 (4): 636–51. https://doi.org/10.1111/maps.12280.
Maskelyne, Nevil. 1775. “An Account of Observations Made on the Mountain Schehallien for Finding Its Attraction.” *Philosophical Transactions of the Royal Society of London* 65 (December): 500–542. https://doi.org/10.1098/RSTL.1775.0050.
Masters, G, J H Woodhouse, and G Freeman. 2011. “Mineos – User Manual Version 1.0.2.” *Computational Infrastructure for Geodynamics*.
Matsukage, Kyoko N., Yoko Nagayo, Matthew L. Whitaker, Eiichi Takahashi, and Toshisuke Kawasaki. 2013. “Melting of the Martian Mantle from 1.0 to 4.5 GPa.” *Journal of Mineralogical and Petrological Sciences* 108 (4): 201–14. https://doi.org/10.2465/jmps.120820.
Matsumura, Soko, Ramon Brasser, and Shigeru Ida. 2017. “N-Body Simulations of Planet Formation via Pebble Accretion: I. First Results.” *Astronomy and Astrophysics* 607 (November): 67. https://doi.org/10.1051/0004-6361/201731155.
McDonough, W. F. 2003. “Compositional Model for the Earth’s Core.” In *Treatise on Geochemistry*, 2–9:547–68. https://doi.org/10.1016/B0-08-043751-6/02015-6.
McDonough, W. F., and S. s. Sun. 1995. “The Composition of the Earth.” *Chemical Geology* 120 (3–4): 223–53. https://doi.org/10.1016/0009-2541(94)00140-4.
Merkel, Sébastien, Sovanndara Hok, Cynthia Bolme, Dylan Rittman, Kyle James Ramos, Benjamin Morrow, Hae Ja Lee, et al. 2021. “Femtosecond Visualization of Hcp-Iron Strength and Plasticity under Shock Compression.” *Physical Review Letters* 127 (20): 205501. https://doi.org/10.1103/PHYSREVLETT.127.205501.
Merkel, Sébastien, and Takehiro Yagi. 2005. “X-Ray Transparent Gasket for Diamond Anvil Cell High Pressure Experiments Properties of Melts in Planetary Interiors View Project Water and Carbon Content of the Deep Earth View Project.” *Article in Review of Scientific Instruments* 76 (4): 046109. https://doi.org/10.1063/1.1884195.
Merkel, Sébastien, Marion Gruson, Yanbin Wang, Norimasa Nishiyama, and Carlos N Tomé. 2012. “Texture and Elastic Strains in Hcp-Iron Plastically Deformed up to 17.5 GPa and 600 K: Experiment and Model.” *Modelling and Simulation in Materials Science and Engineering* 20 (2): 024005. https://doi.org/10.1088/0965-0393/20/2/024005.
Merkel, Sébastien, H. P. Liermann, L. Miyagi, and H. R. Wenk. 2013. “In Situ Radial X-Ray Diffraction Study of Texture and Stress during Phase Transformations in Bcc-, Fcc-and Hcp-Iron up to 36 GPa and 1000 K.” *Acta Materialia* 61 (14): 5144–51. https://doi.org/10.1016/j.actamat.2013.04.068.
Merkel, Sébastien, Hans Rudolf Wenk, Philippe Gillet, Ho kwang Mao, and Russell J. Hemley. 2004. “Deformation of Polycrystalline Iron up to 30GPa and 1000K.” *Physics of the Earth and Planetary Interiors* 145 (1–4): 239–51. https://doi.org/10.1016/j.pepi.2004.04.001.
Michel, Nathalie, and Olivier Forni. 2011. “Mars Mantle Convection: Influence of Phase Transitions with Core Cooling.” *Planetary and Space Science* 59 (8): 741–48. https://doi.org/10.1016/j.pss.2011.02.013.

Morard, Guillaume, Johann Bouchet, Attilio Rivoldini, Daniele Antonangeli, Mathilde Roberge, Eglantine Boulard, Adrien Denoeud, and Mohamed Mezouar. 2018. “Liquid Properties in the Fe-FeS System under Moderate Pressure: Tool Box to Model Small Planetary Cores.” *American Mineralogist* 103 (11): 1770–79. https://doi.org/10.2138/am-2018-6405.
Morbidelli, A., B. Bitsch, A. Crida, M. Gounelle, T. Guillot, S. Jacobson, A. Johansen, M. Lambrechts, and E. Lega. 2016. “Fossilized Condensation Lines in the Solar System Protoplanetary Disk.” *Icarus* 267: 368–76. https://doi.org/10.1016/j.icarus.2015.11.027.
Morgan, John W., and Edward Anders. 1979. “Chemical Composition of Mars.” *Geochimica et Cosmochimica Acta* 43 (10): 1601–10. https://doi.org/10.1016/0016-7037(79)90180-7.
Morishima, Ryuji, Gregor J Golabek, and Henri Samuel. 2013. *N-Body Simulations of Oligarchic Growth of Mars: Implications for Hf-W Chronology*. Vol. 366. https://www.sciencedirect.com/science/article/pii/S0012821X13000538.
Moskovitz, Nicholas, and Eric Gaidos. 2011. “Differentiation of Planetesimals and the Thermal Consequences of Melt Migration.” *Meteoritics and Planetary Science* 46 (6): 903–18. https://doi.org/10.1111/j.1945-5100.2011.01201.x.
Newton, Isaac. 1687. “De Mundi Systemate.” In *Philosophiæ Naturalis Principia Mathematica*, 1st ed.
Nimmo, F., and U. H. Faul. 2013. “Dissipation at Tidal and Seismic Frequencies in a Melt-Free, Anhydrous Mars.” *Journal of Geophysical Research: Planets* 118 (12): 2558–69. https://doi.org/10.1002/2013JE004499.
Nimmo, F., and T. Kleine. 2007. “How Rapidly Did Mars Accrete? Uncertainties in the Hf-W Timing of Core Formation.” *Icarus* 191 (2): 497–504. https://doi.org/10.1016/j.icarus.2007.05.002.
Nimmo, F., and D. J. Stevenson. 2000. “Influence of Early Plate Tectonics on the Thermal Evolution and Magnetic Field of Mars.” *Journal of Geophysical Research E: Planets* 105 (E5): 11969–79. https://doi.org/10.1029/1999JE001216.
Nishida, Keisuke, Eiji Ohtani, Satoru Urakawa, Akio Suzuki, Tatsuya Sakamaki, Hidenori Terasaki, and Yoshinori Katayama. 2011. “Density Measurement of Liquid FeS at High Pressures Using Synchrotron X-Ray Absorption.” *American Mineralogist* 96 (5–6): 864–68. https://doi.org/10.2138/am.2011.3616.
O’Brien, David P., Kevin J. Walsh, Alessandro Morbidelli, Sean N. Raymond, and Avi M. Mandell. 2014. “Water Delivery and Giant Impacts in the ‘Grand Tack’ Scenario.” *Icarus* 239 (September): 74–84. https://doi.org/10.1016/j.icarus.2014.05.009.
Okamura, Tatsuya, and Hiroshi Kobayashi. 2021. “The Growth of Protoplanets via the Accretion of Small Bodies in Disks Perturbed by the Planetary Gravity.” *The Astrophysical Journal* 916 (2): 109. https://doi.org/10.3847/1538-4357/AC06C6.
Palme, H., and H. St. C. O’Neill. 2007. “Cosmochemical Estimates of Mantle Composition.” *Treatise on Geochemistry* 2–9: 1–38. https://doi.org/10.1016/B0-08-043751-6/02177-0.
Panning, Mark P., Philippe Lognonné, W. Bruce Banerdt, Raphaël Garcia, Matthew Golombek, Sharon Kedar, Brigitte Knapmeyer-Endrun, et al. 2017. “Planned Products of the Mars Structure Service for the InSight Mission to Mars.” *Space Science Reviews* 211 (1–4): 611–50. https://doi.org/10.1007/s11214-016-0317-5.
Plesa, A. C., S. Padovan, N. Tosi, D. Breuer, M. Grott, M. A. Wieczorek, T. Spohn, S. E. Smrekar, and W. B. Banerdt. 2018. “The Thermal State and Interior Structure of Mars.” *Geophysical Research Letters* 45 (22): 12,198-12,209. https://doi.org/10.1029/2018GL080728.
Rai, Nachiketa, and Wim Van Westrenen. 2013. “Core-Mantle Differentiation in Mars.” *Journal of Geophysical Research E: Planets* 118 (6): 1195–1203. https://doi.org/10.1002/jgre.20093.
Raymond, Sean N., and Alessandro Morbidelli. 2014. “The Grand Tack Model: A Critical Review.” In *Proceedings of the International Astronomical Union*, 9:194–203. Cambridge University Press. https://doi.org/10.1017/S1743921314008254.
Raymond, Sean N., David P. O’Brien, Alessandro Morbidelli, and Nathan A. Kaib. 2009. “Building the Terrestrial Planets: Constrained Accretion in the Inner Solar System.” *Icarus* 203 (2): 644–62. https://doi.org/10.1016/j.icarus.2009.05.016.

Reaman, Daniel M., Glenn S. Daehn, and Wendy R. Panero. 2011. “Predictive Mechanism for Anisotropy Development in the Earth’s Inner Core.” *Earth and Planetary Science Letters* 312 (3–4): 437–42. https://doi.org/10.1016/j.epsl.2011.10.038.

Ricolleau, Angele, Yingwei Fei, Alexandre Corgne, Julien Siebert, and James Badro. 2011. “Oxygen and Silicon Contents of Earth’s Core from High Pressure Metal-Silicate Partitioning Experiments.” *Earth and Planetary Science Letters* 310 (3–4): 409–21. https://doi.org/10.1016/j.epsl.2011.08.004.

Righter, K., and C. K. Shearer. 2003. “Magmatic Fractionation of Hf and W: Constraints on the Timing of Core Formation and Differentiation in the Moon and Mars.” *Geochimica et Cosmochimica Acta* 67 (13): 2497–2507. https://doi.org/10.1016/S0016-7037(02)01349-2.

Righter, Kevin, and Nancy L. Chabot. 2011. “Moderately and Slightly Siderophile Element Constraints on the Depth and Extent of Melting in Early Mars.” *Meteoritics and Planetary Science* 46 (2): 157–76. https://doi.org/10.1111/j.1945-5100.2010.01140.x.

Righter, Kevin, and Michael J. Drake. 1996. “Core Formation in Earth’s Moon, Mars, and Vesta.” *Icarus* 124 (2): 513–29. https://doi.org/10.1006/icar.1996.0227.

Rivoldini, A., T. Van Hoolst, O. Verhoeven, A. Mocquet, and V. Dehant. 2011. “Geodesy Constraints on the Interior Structure and Composition of Mars.” *Icarus* 213 (2): 451–72. https://doi.org/10.1016/j.icarus.2011.03.024.

Rose-Weston, Lesley, James M. Brenan, Yingwei Fei, Richard A. Secco, and Daniel J. Frost. 2009. “Effect of Pressure, Temperature, and Oxygen Fugacity on the Metal-Silicate Partitioning of Te, Se, and S: Implications for Earth Differentiation.” *Geochimica et Cosmochimica Acta* 73 (15): 4598–4615. https://doi.org/10.1016/j.gca.2009.04.028.

Rubie, D. C. DC, SA A. Jacobson, A. Morbidelli, David P. O’Brien, E. D. Young, J. de Vries, F. Nimmo, H. Palme, and Daniel J. Frost. 2015. “Accretion and Differentiation of the Terrestrial Planets with Implications for the Compositions of Early-Formed Solar System Bodies and Accretion of Water.” *Icarus* 248: 89–108. https://doi.org/10.1016/j.icarus.2014.10.015.

Rubie, David C., Daniel J. Frost, Ute Mann, Yuki Asahara, Francis Nimmo, Kyusei Tsuno, Philip Kegler, Astrid Holzheid, and Herbert Palme. 2011. “Heterogeneous Accretion, Composition and Core-Mantle Differentiation of the Earth.” *Earth and Planetary Science Letters* 301 (1–2): 31–42. https://doi.org/10.1016/j.epsl.2010.11.030.

Rubie, David C., Christine K. Gessmann, and Daniel J. Frost. 2004. “Partitioning of Oxygen during Core Formation on the Earth and Mars.” *Nature* 429 (6987): 58–61. https://doi.org/10.1038/nature02473.

Rudge, John F., Thorsten Kleine, and Bernard Bourdon. 2010. “Broad Bounds on Earths Accretion and Core Formation Constrained by Geochemical Models.” *Nature Geoscience* 3 (6): 439–43. https://doi.org/10.1038/ngeo872.

Sahijpal, S., and G. K. Bhatia. 2015. “The Role of Impact and Radiogenic Heating in the Early Thermal Evolution of Mars.” *Journal of Earth System Science* 124 (1): 241–60. https://doi.org/10.1007/s12040-014-0518-9.

Sakai, Takeshi, Eiji Ohtani, Naohisa Hirao, and Yasuo Ohishi. 2011. “Equation of State of the NaCl-B2 Phase up to 304 GPa.” *Journal of Applied Physics* 109 (8). https://doi.org/10.1063/1.3573393.

Sanloup, C., A. Jambon, and P. Gillet. 1999. “A Simple Chondritic Model of Mars.” *Physics of the Earth and Planetary Interiors* 112 (1–2): 43–54. https://doi.org/10.1016/S0031-9201(98)00175-7.

Sato-Sorensen, Y. 1983. “Phase Transitions and Equations of State for the Sodium Halides: NaF, NaCl, NaBr, and NaI.” *Journal of Geophysical Research* 88 (B4): 3543–48. https://doi.org/10.1029/JB088iB04p03543.

Seagle, Christopher T., Andrew J. Campbell, Dion L. Heinz, Guoyin Shen, and Vitali B. Prakapenka. 2006. “Thermal Equation of State of Fe3S and Implications for Sulfur in Earth’s Core.” *Journal of Geophysical Research: Solid Earth* 111 (6). https://doi.org/10.1029/2005JB004091.

Seitz, Frederick. 1946. “Color Centers in Alkali Halide Crystals.” *Reviews of Modern Physics* 18 (3): 384–408. https://doi.org/10.1103/RevModPhys.18.384.

Siebert, Julien, Alexandre Corgne, and Frederick J. Ryerson. 2011. “Systematics of Metal-Silicate Partitioning for Many Siderophile Elements Applied to Earth’s Core Formation.” *Geochimica et Cosmochimica Acta* 75 (6): 1451–89. https://doi.org/10.1016/j.gca.2010.12.013.

Singh, Anil K., and C. Balasingh. 1994. “The Lattice Strains in a Specimen (Hexagonal System) Compressed Nonhydrostatically in an Opposed Anvil High Pressure Setup.” *Journal of Applied Physics* 75 (10): 4956–62. https://doi.org/10.1063/1.355786.

Singh, Jagbir, Nirmal Singh, P. N. Trehan, Rupinder Singh, and D. Mehta. 1994. “PEAKFIT-a PC Based Code for Analysis of Gamma Ray Spectra.” In *DAE Symposium on Nuclear Physics. Vol. 37B: Contributed Papers*.

Smith, Jesse S., Stanislav V. Sinogeikin, Chuanlong Lin, Eric Rod, Ligang Bai, and Guoyin Shen. 2015. “Developments in Time-Resolved High Pressure X-Ray Diffraction Using Rapid Compression and Decompression.” *Review of Scientific Instruments* 86 (7): 072208. https://doi.org/10.1063/1.4926887.

Sohl, Frank, and Tilman Spohn. 1997. “The Interior Structure of Mars: Implications from SNC Meteorites.” *Journal of Geophysical Research E: Planets* 102 (E1): 1613–35. https://doi.org/10.1029/96JE03419.

Somers, M. A.J., B. J. Kooi, L. Maldzinski, E. J. Mittemeijer, A. A. Van Der Horst, A. M. Van Der Kraan, and N. M. Van Der Pers. 1997. “Thermodynamics and Long-Range Order of Interstitials in an h.c.p. Lattice: Nitrogen in ε-Fe2N1 − Z.” *Acta Materialia* 45 (5): 2013–25. https://doi.org/10.1016/S1359-6454(96)00307-2.

Speziale, Sergio, Chang-Sheng Zha, Thomas S. Duffy, Russell J. Hemley, and Ho-kwang Mao. 2001. “Quasi-Hydrostatic Compression of Magnesium Oxide to 52 GPa: Implications for the Pressure-Volume-Temperature Equation of State.” *Journal of Geophysical Research: Solid Earth* 106 (B1): 515–28. https://doi.org/10.1029/2000jb900318.

Stähler, Simon C., Amir Khan, W. Bruce Banerdt, Philippe Lognonné, Domenico Giardini, Savas Ceylan, Mélanie Drilleau, et al. 2021. “Seismic Detection of the Martian Core.” *Science* 373 (6553): 443–48. https://doi.org/10.1126/science.abi7730.

Steenstra, Edgar S., and Wim van Westrenen. 2018. “A Synthesis of Geochemical Constraints on the Inventory of Light Elements in the Core of Mars.” *Icarus* 315 (November): 69–78. https://doi.org/10.1016/j.icarus.2018.06.023.

Stixrude, Lars, and Carolina Lithgow-Bertelloni. 2011. “Thermodynamics of Mantle Minerals - II. Phase Equilibria.” *Geophysical Journal International* 184 (3): 1180–1213. https://doi.org/10.1111/j.1365-246X.2010.04890.x.

Suehiro, Sho, Kenji Ohta, Kei Hirose, Guillaume Morard, and Yasuo Ohishi. 2017. “The Influence of Sulfur on the Electrical Resistivity of Hcp Iron: Implications for the Core Conductivity of Mars and Earth.” *Geophysical Research Letters* 44 (16): 8254–59. https://doi.org/10.1002/2017GL074021.

Tateno, Shigehiko, Kei Hirose, Yasuo Ohishi, and Yoshiyuki Tatsumi. 2010. “The Structure of Iron in Earth’s Inner Core.” *Science* 330 (6002): 359–61. https://doi.org/10.1126/science.1194662.

Tateno, Shigehiko, Yasuhiro Kuwayama, Kei Hirose, and Yasuo Ohishi. 2015. “The Structure of Fe-Si Alloy in Earth’s Inner Core.” *Earth and Planetary Science Letters* 418: 11–19. https://doi.org/10.1016/j.epsl.2015.02.008.

Taylor, G. Jeffrey. 2013. “The Bulk Composition of Mars.” *Chemie Der Erde* 73 (4): 401–20. https://doi.org/10.1016/j.chemer.2013.09.006.

Taylor, J., N. A. Teanby, and J. Wookey. 2013. “Estimates of Seismic Activity in the Cerberus Fossae Region of Mars.” *Journal of Geophysical Research E: Planets* 118 (12): 2570–81. https://doi.org/10.1002/2013JE004469.

Thompson, Elizabeth C., Bethany A. Chidester, Rebecca A. Fischer, Gregory I. Myers, Dion L. Heinz, Vitali B. Prakapenka, and Andrew J. Campbell. 2016. “Equation of State of Pyrite to 80 GPa and 2400 K.” *American Mineralogist* 101 (5): 1046–51. https://doi.org/10.2138/am-2016-5527.

Tian, Zhen, Tomáš Magna, James M.D. Day, Klaus Mezger, Erik E. Scherer, Katharina Lodders, Remco C. Hin, Piers Koefoed, Hannah Bloom, and Kun Wang. 2021. “Potassium Isotope Composition of Mars Reveals a Mechanism of Planetary Volatile Retention.” *Proceedings of the National Academy of Sciences* 118 (39): e2101155118. https://doi.org/10.1073/PNAS.2101155118.
Toda-Caraballo, Isaac, and Pedro E.J. Rivera-Díaz-Del-Castillo. 2015. “Modelling Solid Solution Hardening in High Entropy Alloys.” *Acta Materialia* 85 (February): 14–23. https://doi.org/10.1016/j.actamat.2014.11.014.
Tschauner, Oliver, Ma Chi, John R. Beckett, Clemens Prescher, Vitali B. Prakapenka, and George R. Rossman. 2014. “Discovery of Bridgmanite, the Most Abundant Mineral in Earth, in a Shocked Meteorite.” *Science* 346 (6213): 1100–1102. https://doi.org/10.1126/science.1259369.
Tsuno, Kyusei, Daniel J. Frost, and David C. Rubie. 2011. “The Effects of Nickel and Sulphur on the Core-Mantle Partitioning of Oxygen in Earth and Mars.” *Physics of the Earth and Planetary Interiors* 185 (1–2): 1–12. https://doi.org/10.1016/j.pepi.2010.11.009.
Tsuno, Kyusei, Damanveer S. Grewal, and Rajdeep Dasgupta. 2018. “Core-Mantle Fractionation of Carbon in Earth and Mars: The Effects of Sulfur.” *Geochimica et Cosmochimica Acta* 238 (October): 477–95. https://doi.org/10.1016/j.gca.2018.07.010.
Tuff, J., J. Wade, and B. J. Wood. 2013. “Volcanism on Mars Controlled by Early Oxidation of the Upper Mantle.” *Nature* 498 (7454): 342–45. https://doi.org/10.1038/nature12225.
Urakawa, Satoru, K. Someya, H. Terasaki, T. Katsura, S. Yokoshi, K.-I. Funakoshi, W. Utsumi, Y. Katayama, Y.-I. Sueda, and T. Irifune. 2004. “Phase Relationships and Equations of State for FeS at High Pressures and Temperatures and Implications for the Internal Structure of Mars.” *Physics of The Earth and Planetary Interiors* 143–144: 469–79. https://doi.org/10.1016/s0031-9201(04)00080-9.
Driel, Martin Van, Savas Ceylan, John Francis Clinton, Domenico Giardini, Hector Alemany, Amir Allam, David Ambrois, et al. 2019. “Preparing for InSight: Evaluation of the Blind Test for Martian Seismicity.” *Seismological Research Letters* 90 (4): 1518–34. https://doi.org/10.1785/0220180379.
Orman, James A. Van. 2004. “On the Viscosity and Creep Mechanism of Earth’s Inner Core.” *Geophysical Research Letters* 31 (20): L20606. https://doi.org/10.1029/2004GL021209.
Vaks, V. G., and K. Yu Khromov. 2008. “On the Theory of Interactions and Thermodynamic Properties of Carbon Atoms in Hcp and Fcc Iron.” *Journal of Experimental and Theoretical Physics 2008 106:1* 106 (1): 94–109. https://doi.org/10.1134/S106377610801007X.
Verhoeven, Olivier, A. Rivoldini, Pierre Vacher, Antoine Mocquet, Gael Choblet, Michel Menvielle, Veronique Dehant, et al. 2005. “Interior Structure of Terrestrial Planets: Modeling Mars’ Mantle and Its Electromagnetic, Geodetic, and Seismic Properties.” *Journal of Geophysical Research E: Planets* 110 (4): 1–19. https://doi.org/10.1029/2004JE002271.
Vočadlo, Lidunka, David P. Dobson, and Ian G. Wood. 2009. “Ab Initio Calculations of the Elasticity of Hcp-Fe as a Function of Temperature at Inner-Core Pressure.” *Earth and Planetary Science Letters* 288 (3–4): 534–38. https://doi.org/10.1016/j.epsl.2009.10.015.
Voelkel, Oliver, Rogerio Deienno, Katherine Kretke, and Hubert Klahr. 2021. “Linking Planetary Embryo Formation to Planetesimal Formation: II. The Effect of Pebble Accretion in the Terrestrial Planet Zone.” *Astronomy and Astrophysics* 645 (January): 132. https://doi.org/10.1051/0004-6361/202039245.
Wade, Jon, Bernard J. Wood, and C. Ashley Norris. 2013. “The Oxidation State of Tungsten in Silicate Melt at High Pressures and Temperatures.” *Chemical Geology* 335: 189–93. https://doi.org/10.1016/j.chemgeo.2012.10.011.
Wade, Jon, Bernard J. Wood, and James Tuff. 2012. “Metal–Silicate Partitioning of Mo and W at High Pressures and Temperatures: Evidence for Late Accretion of Sulphur to the Earth.” *Geochimica et Cosmochimica Acta* 85 (May): 58–74. https://doi.org/10.1016/J.GCA.2012.01.010.
Walsh, Kevin J., and Harold F. Levison. 2019. “Planetesimals to Terrestrial Planets: Collisional Evolution amidst a Dissipating Gas Disk.” *Icarus* 329 (September): 88–100. https://doi.org/10.1016/j.icarus.2019.03.031.

Walsh, Kevin J., Alessandro Morbidelli, Sean N. Raymond, David P. O'Brien, and Avi M. Mandell. 2011. "A Low Mass for Mars from Jupiter's Early Gas-Driven Migration." *Nature* 475 (7355): 206–9. https://doi.org/10.1038/nature10201.

Wang, Jingyun, Stanislav V. Sinogeikin, Toru Inoue, and Jay D. Bass. 2003. "Elastic Properties of Hydrous Ringwoodite." *American Mineralogist* 88 (10): 1608–11. https://doi.org/10.2138/am-2003-1025.

Wang, Zaicong, and Harry Becker. 2017. "Chalcophile Elements in Martian Meteorites Indicate Low Sulfur Content in the Martian Interior and a Volatile Element-Depleted Late Veneer." *Earth and Planetary Science Letters* 463 (April): 56–68. https://doi.org/10.1016/j.epsl.2017.01.023.

Wänke, Heinrich. 1991. "Chemistry, Accretion, and Evolution of Mars." *Space Science Reviews* 56 (1–2): 1–8. https://doi.org/10.1007/BF00178384.

Wänke, Heinrich, and G. Dreibus. 1988. "Chemical Composition and Accretion History of Terrestrial Planets." *Philosophical Transactions of the Royal Society of London. Series A, Mathematical and Physical Sciences* 325 (1587): 545–57. https://doi.org/10.1098/rsta.1988.0067.

Warren, Paul H. 2011. "Stable-Isotopic Anomalies and the Accretionary Assemblage of the Earth and Mars: A Subordinate Role for Carbonaceous Chondrites." *Earth and Planetary Science Letters* 311: 93–100. https://doi.org/10.1016/j.epsl.2011.08.047.

Weber, Renee C., Pei Ying Lin, Edward J. Garnero, Quentin Williams, and Philippe Lognonné. 2011. "Seismic Detection of the Lunar Core." *Science* 331 (6015): 309–12. https://doi.org/10.1126/science.1199375.

Weertman, J. 1970. "The Creep Strength of the Earth's Mantle." *Reviews of Geophysics* 8 (1): 145. https://doi.org/10.1029/RG008i001p00145.

Weichert, Emil. 1897. "Ueber Die Massenverteilung Im Inneren Der Erde." *Nachrichten von Der Gesellschaft Der Wissenschaften Zu Göttingen, Mathematisch-Physikalische Klasse* 3: 221–43.

Wenk, H. R., S. Matthies, J. Donovan, and D. Chateigner. 1998. "BEARTEX: A Windows-Based Program System for Quantitative Texture Analysis." *Journal of Applied Crystallography* 31 (2): 262–69. https://doi.org/10.1107/S002188989700811X.

Wenk, H. R., S. Matthies, R. J. Hemley, H. K. Mao, and J. Shu. 2000. "The Plastic Deformation of Iron at Pressures of the Earth's Inner Core." *Nature* 405 (6790): 1044–47. https://doi.org/10.1038/35016558.

Wetherill, GW. 1991. "Why Isn't Mars as Big as Earth?" *Lunar and Planetary Science Conference* 22: 1495–96. http://scholar.google.com/scholar?hl=en&btnG=Search&q=intitle:No+Title#0%5Cnhttp://adsabs.harvard.edu/full/1991LPI....22.1495W.

White, W. M. 2013. *Geochemistry*. John Wiley & Sons.

Wieczorek, Mark A., and Maria T. Zuber. 2004. "Thickness of the Martian Crust: Improved Constraints from Geoid-to-Topography Ratios." *Journal of Geophysical Research E: Planets* 109 (1). https://doi.org/10.1029/2003je002153.

Williams, Curtis D., Matthew E. Sanborn, Céline Defouilloy, Qing Zhu Yin, Noriko T. Kita, Denton S. Ebel, Akane Yamakawa, and Katsuyuki Yamashita. 2020. "Chondrules Reveal Large-Scale Outward Transport of Inner Solar System Materials in the Protoplanetary Disk." *Proceedings of the National Academy of Sciences of the United States of America* 117 (38): 23426–35. https://doi.org/10.1073/pnas.2005235117.

Williams, John Pierre, and Francis Nimmo. 2004. "Thermal Evolution of the Martian Core: Implications for an Early Dynamo." *Geology* 32 (2): 97–100. https://doi.org/10.1130/G19975.1.

Wood, Bernard J., Jie Li, and Anat Shahar. 2013. "Carbon in the Core: Its Influence on the Properties of Core and Mantle." *Reviews in Mineralogy and Geochemistry* 75 (1): 231–50. https://doi.org/10.2138/RMG.2013.75.8.

Yamazaki, Daisuke, Noriyoshi Tsujino, Akira Yoneda, Eiji Ito, Takashi Yoshino, Yoshinori Tange, and Yuji Higo. 2017. “Grain Growth of ε-Iron: Implications to Grain Size and Its Evolution in the Earth’s Inner Core.” *Earth and Planetary Science Letters* 459 (February): 238–43. https://doi.org/10.1016/j.epsl.2016.11.049.

Yang, Shuying, Munir Humayun, Kevin Righter, Gwendolyn Jefferson, Dana Fields, and Anthony J. Irving. 2015. “Siderophile and Chalcophile Element Abundances in Shergottites: Implications for Martian Core Formation.” *Meteoritics and Planetary Science* 50 (4): 691–714. https://doi.org/10.1111/maps.12384.

Yoo, M. H., J. R. Morris, K. M. Ho, and S. R. Agnew. 2002. “Nonbasal Deformation Modes of HCP Metals and Alloys: Role of Dislocation Source and Mobility.” *Metallurgical and Materials Transactions A: Physical Metallurgy and Materials Science* 33 (3): 813–22. https://doi.org/10.1007/s11661-002-0150-1.

Yoshida, Shigeo, Ikuro Sumita, and Mineo Kumazawa. 1996. “Growth Model of the Inner Core Coupled with the Outer Core Dynamics and the Resulting Elastic Anisotropy.” *Journal of Geophysical Research: Solid Earth* 101 (B12): 28085–103. https://doi.org/10.1029/96jb02700.

Yoshizaki, Takashi, and William F. McDonough. 2020. “The Composition of Mars.” *Geochimica et Cosmochimica Acta* 273 (March): 137–62. https://doi.org/10.1016/j.gca.2020.01.011.

Zhang, Zhongtian, David Bercovici, and Jacob S. Jordan. 2021. “A Two-Phase Model for the Evolution of Planetary Embryos With Implications for the Formation of Mars.” *Journal of Geophysical Research: Planets* 126 (4). https://doi.org/10.1029/2020je006754.

Zharkov, V. N., and T. V. Gudkova. 2005. “Construction of Martian Interior Model.” *Solar System Research* 39 (5): 343–73. https://doi.org/10.1007/s11208-005-0049-7.

Zheng, Yingcai, Francis Nimmo, and Thorne Lay. 2015. “Seismological Implications of a Lithospheric Low Seismic Velocity Zone in Mars.” *Physics of the Earth and Planetary Interiors* 240: 132–41. https://doi.org/10.1016/j.pepi.2014.10.004.

Zube, Nicholas G., Francis Nimmo, Rebecca A. Fischer, and Seth A. Jacobson. 2019. “Constraints on Terrestrial Planet Formation Timescales and Equilibration Processes in the Grand Tack Scenario from Hf-W Isotopic Evolution.” *Earth and Planetary Science Letters* 522 (September): 210–18. https://doi.org/10.1016/j.epsl.2019.07.001.